To the Graduate Council:

I am submitting herewith a thesis written by Jeffrey Allen Gatscher entitled "Mechanical Impedance Methods for Vibration Simulation." I have examined the final copy of this thesis for form and content and recommend that it be accepted in partial fulfillment of the requirements for the degree of Master of Science, with a major in Mechanical Engineering.

Grzegorz Kawiecki

Grzegorz Kawiecki, Ph.D., Major Professor

We have read this thesis
and recommend its acceptance:

A J Edmondson

Andrew J. Edmondson, Ph.D.

J A M Boulet

J. A. M. Boulet, Ph.D.

Accepted for the Council:

Carl Minkel

Associate Vice Chancellor
and Dean of The Graduate School

STATEMENT OF PERMISSION TO USE

In presenting this thesis in partial fulfillment of the requirements for a Master's degree at The University of Tennessee, Knoxville, I agree that the Library shall make it available to borrowers under rules of the Library. Brief quotations from this thesis are allowable without special permission, provided that accurate acknowledgment of the source is made.

Permission for extensive quotation from or reproduction of this thesis may be granted by my major professor, or in his absence, by the Head of Interlibrary Services when, in the opinion of ether, the proposed use of the material is for scholarly purposes. Any copying or use of the material in this thesis for financial gain shall not be allowed without my written permission.

Signature Jeffry A. Satcher

Date JULY 20, 1994

MECHANICAL IMPEDANCE METHODS FOR VIBRATION SIMULATION

A Thesis

Presented for the

Master of Science Degree

The University of Tennessee, Knoxville

Jeffrey Allen Gatscher

August, 1994

DEDICATION

This thesis is dedicated to my loving wife,

Eva Marie

who has awakened my spirit

and inspired me to pursue my dreams.

ACKNOWLEDGMENTS

I would like to thank my colleagues at Raytheon Company for their comments, suggestions, and assistance over the past year. In particular, I would like to thank Jim Suhre for introducing me to this very engaging topic, Robert Wynn for reviewing and amending this thesis, and Brian Nikkari for performing vibration testing. I would like to thank my major professor, Dr. Grzegorz Kawiecki for allowing me the freedom to thoroughly explore the details of this subject. Finally, I would like to express my thanks to my wife, Eva, for her understanding and patience during those long nights and weekends that were spent away from where I wanted to be.

ABSTRACT

Realistic laboratory simulation of a system's field vibration environment has been of major concern to design and test engineers for many years. The usual practice of basing vibration design and test specifications on an envelope of the equipment base acceleration levels experienced in the field environment has often resulted in excessive levels of overtesting. This results from the large differences between the mechanical impedance of the vehicle structure and that of a fully equalized vibration shaker. Mechanical impedance effects occur naturally in a field environment. Including such effects in a laboratory vibration environment achieves more realistic conditions of similitude. A possible solution to the problem is the generation of design and test specifications that are based on the knowledge of both the acceleration and the forces transmitted to the equipment in the field environment.

This research points out the detrimental effects which result when impedance effects are not considered in relating test requirements with field measurements. The ways in which these effects can be considered are evaluated, and comparison of three impedance methods is accomplished based on a cumulative damage criterion. A test structure is used to simulate an equipment and support foundation system. Detailed finite element analysis is performed to aid in computation of cumulative damage totals. The results indicate that mechanical impedance methods can be effectively used to reproduce the field vibration environment in a laboratory test. The establishment of a well developed finite element computer model coupled with laboratory impedance measurements can eliminate the overtesting problems inherent with constant motion, infinite impedance testing.

TABLE OF CONTENTS

CHAPTER		PAGE
1.	INTRODUCTION	1
	The Problem	1
	Mechanical Impedance History	2
	Thesis Organization	3
2.	SPECTRAL ENVELOPING AND RESONANCE VS. ANTIRESONANCE	6
	The Infinite Impedance Vibration Test	6
	Dynamic Loading and Antiresonance	8
	Determination of Antiresonance Frequencies	9
	Application - Determination of Antiresonance Frequencies	12
	Infinite Impedance Overtest	15
3.	DYNAMIC INTERACTION BETWEEN EQUIPMENT AND SUPPORT	20
	Response Parameters	20
	Dimensionless System Parameters	25
	Parametric Results	26
4.	MECHANICAL IMPEDANCE AND CONNECTION OF STRUCTURES	37
	Mechanical Impedance of Spring-Mass-Damper System	38
	Impedance of Multi-Degree-of-Freedom System	41
	Impedance of Connected Subsystems	43
	Application - Impedance Method for MDOF System	46
	Impedance of Simplified System	53
5.	VIBRATION TESTING USING MECHANICAL IMPEDANCE METHODS	57
	Force-Acceleration Product Method	58
	Dual Extremal Control Method	62
	Transmissibility Correction Method	65
	Vibration Test Method Comparison	69
6.	VIBRATION EQUIVALENCE - SIMULATION OF FIELD ENVIRONMENT	76
	Linear Cumulative Damage	76
	Experimental Study	77
	Vibration Equivalence	93
	Advantages and Disadvantages	102

CHAPTER PAGE

7. MISSILE DESIGN PROBLEM 104
What Went Wrong? 104
Missile Computer Model 106
Finite Element Analysis 107
Results Comparison 113

8. IMPLEMENTATION, PROCEDURE, AND CONCLUSION 120
Dual Extremal Control Vibration Controller 120
Dual Control Force Spectrum 121
The Procedure 125
Conclusion 129

REFERENCES 130

APPENDIXES 134
APPENDIX A. Chapter 5 Subsystem *II* 5-DOF Simulation Results 135
APPENDIX B. Chapter 6 Fabrication Drawings of Beam/Block Structure 142
APPENDIX C. Chapter 7 Missile Structural Dynamic Properties 147

VITA 153

LIST OF TABLES

TABLE		PAGE
2.1	5-DOF antiresonance frequencies - theory versus computed	16
6.1	Experimental vs. calculated natural frequencies, combined system	86
6.2	Experimental vs. calculated natural frequencies, subsystem	89
6.3	Cumulative damage totals	100
7.1	Experimental vs. calculated natural frequencies, SM-2 AUR	108
7.2	Dynamic characteristics of hard-mounted and isolated IR seeker proposals	109
7.3	Results comparison of hard-mounted and vibration isolated seeker proposals	117
8.1	Typical data used to calculate force control specification	124
C.1	SM-2 Block IIIA MR dynamic properties listing	148

LIST OF FIGURES

FIGURE		PAGE
2.1	Typical frequency response function displaying characteristic peaks and characteristic valleys.	7
2.2	Five-degree-of-freedom, free-free, dynamic chain system.	10
2.3	FRF of m_1 and m_2 resulting from harmonic loading at structure support masses.	14
2.4	FRF of m_3, m_4, and m_5 resulting from harmonic loading at structure support masses.	14
2.5	Acceleration test specification as an envelope of m_3 base field acceleration levels.	17
2.6	FRF of m_4 field results from 5-DOF system versus hypothetical infinite impedance equipment test.	18
2.7	FRF of m_5 field results from 5-DOF system versus hypothetical infinite impedance equipment test.	18
3.1	Two-degree-of-freedom system with base input motion for parametric study.	21
3.2	Single-degree-of-freedom system with base input motion for parametric study.	27
3.3	Mean square relative disp. of m_1 as a function of ω_2/ω_1 and M for $\zeta_1 = \zeta_2 =$ 2%	29
3.4	Mean square relative disp. of m_2 as a function of ω_2/ω_1 and M for $\zeta_1 = \zeta_2 =$ 2%	29
3.5	Mean square acceleration of m_1 as a function of ω_2/ω_1 and M for $\zeta_1 = \zeta_2 =$ 2%	30
3.6	Mean square acceleration of m_2 as a function of ω_2/ω_1 and M for $\zeta_1 = \zeta_2 =$ 2%	30

FIGURE PAGE

3.7 Mean square relative disp. of m_1 as a function of M and ω_2/ω_1 for $\zeta_1 = \zeta_2 =$ 2% 32

3.8 Mean square acceleration of m_1 as a function of M and ω_2/ω_1 for $\zeta_1 = \zeta_2 =$ 2% 32

3.9 Mean square relative disp. of m_1 as a function of M and equal damping ratios for $\omega_2/\omega_1 = 1$ 34

3.10 Mean square acceleration of m_1 as a function of M and equal damping ratios for $\omega_2/\omega_1 = 1$ 34

3.11 Mean square rel. disp. of m_1 as a function of M and ζ_2 for $\omega_2/\omega_1 = 1$ and ζ_1 = 1% 35

3.12 Mean square accel. of m_1 as a function of M and ζ_2 for $\omega_2/\omega_1 = 1$ and $\zeta_1 =$ 1% 35

3.13 Mean square rel. disp. of m_1 as a function of M and ζ_1 for $\omega_2/\omega_1 = 1$ and ζ_2 = 1% 36

3.14 Mean square accel. of m_1 as a function of M and ζ_1 for $\omega_2/\omega_1 = 1$ and $\zeta_2 =$ 1% 36

4.1 Single-degree-of-freedom system with applied force. 39

4.2 General linear elastic body subjected to arbitrary loading. 42

4.3 Connection of three subsystems to form a combined missile structure assembly. 44

4.4 Ten-degree-of-freedom, free-free, dynamic chain analog system and the three subsystems. 47

4.5 Driving point and transfer accelerance FRF of subsystem *I* at missile station 1. 48

4.6 Driving point and transfer accelerance FRF of subsystem *I* at missile station 2. 48

4.7 Driving point and transfer accelerance FRF of subsystem *II* at missile station 2. 49

FIGURE PAGE

4.8 Driving point and transfer accelerance FRF of subsystem *II* at missile station 3. 49

4.9 Driving point and transfer accelerance FRF of subsystem *III* at missile station 3. 50

4.10 Driving point and transfer accelerance FRF of subsystem *III* at missile station 4. 50

4.11 Interface force FRF at missile stations 2 and 3 resulting from impedance calculation method Eqs. (4.11) and (4.12). 51

4.12 Acceleration FRF of m_1, m_4, m_7, and m_9 resulting from impedance method Eqs. (4.13) through (4.16). 51

4.13 Acceleration FRF of m_1, and m_4, impedance calculation method versus direct solution. 52

4.14 Acceleration FRF of m_7 and m_9, impedance calculation method versus direct solution. 52

4.15 Combined system with an active vibration source (*subsystem I*) and passive vibration load (*subsystem II*). 54

5.1 Acceleration FRF of m_7 from 10-DOF field results with envelope of peaks for force-acceleration product test. 61

5.2 Driving point accelerance FRF of subsystem *III* with envelope of peaks for force-acceleration product test. 61

5.3 Input acceleration FRF to be applied to subsystem *III* for force-acceleration product test. 63

5.4 Acceleration of m_8 comparing 10-DOF field results to those obtained from subsystem *III* test using force-acceleration. 63

5.5 Acceleration of m_9 comparing 10-DOF field results to those obtained from subsystem *III* test using force-acceleration. 64

5.6 Acceleration of m_{10} comparing 10-DOF field results to those obtained from subsystem *III* test using force-acceleration. 64

FIGURE PAGE

5.7 Acceleration control spectrum shown as an envelope of peak m_7 interface levels for dual control test. 66

5.8 Force control spectrum shown as an envelope of peak m_7 interface levels for dual control test. 66

5.9 Input acceleration FRF to be applied to subsystem *III* for dual control test. 67

5.10 Acceleration FRF of m_8 comparing 10-DOF field results to those obtained from subsystem *III* test using dual control. 67

5.11 Acceleration FRF of m_9 comparing 10-DOF field results to those obtained from subsystem *III* test using dual control. 68

5.12 Acceleration FRF of m_{10} comparing 10-DOF field results to those obtained from subsystem *III* test using dual control. 68

5.13 Acceleration FRF of m_7 from 10-DOF field results with envelope of peaks for transmissibility correction test. 70

5.14 Transmissibility FRF of m_{10} for transmissibility correction test. 70

5.15 Input acceleration FRF to be applied to subsystem *III* for transmissibility correction test. 71

5.16 Acceleration of m_8 comparing 10-DOF field results to those from subsystem *III* test using transmiss. correction. 71

5.17 Acceleration of m_9 comparing 10-DOF field results to those from subsystem *III* test using transmiss. correction. 72

5.18 Acceleration of m_{10} comparing 10-DOF field results to those from subsystem *III* test using transmiss. correction. 72

5.19 Acceleration FRF of m_8 comparing the three impedance test methods vs. an infinite impedance test for subsystem *III*. 73

5.20 Acceleration FRF of m_9 comparing the three impedance test methods vs. an infinite impedance test for subsystem *III*. 73

5.21 Acceleration FRF of m_{10} comparing the three impedance test methods vs. an infinite impedance test for subsystem *III*. 74

6.1 Isometric view of beam and block combined test structure for use in combined system vibration testing. 78

6.2 Isometric view of subsystem beam and block structure for use in subsystem vibration testing. 78

6.3 Location of accelerometers as instrumented on combined structural system. 79

6.4 Experimental test data results for combined system - accelerometer location #1. 81

6.5 Experimental test data results for combined system - accelerometer locations #2 and #3. 81

6.6 Experimental test data results for combined system - accelerometer locations #4 and #5. 82

6.7 First mode shape from finite element modal analysis of the combined structural system. 83

6.8 Second mode shape from finite element modal analysis of the combined structural system. 83

6.9 Third mode shape from finite element modal analysis of the combined structural system. 84

6.10 Fourth mode shape from finite element modal analysis of the combined structural system. 84

6.11 Fifth mode shape from finite element modal analysis of the combined structural system. 85

6.12 Sixth mode shape from finite element modal analysis of the combined structural system. 85

6.13 Comparison of experimental versus calculated response at accelerometer location #1 for combined system. 87

FIGURE PAGE

6.14 Comparison of experimental versus calculated response at accelerometer location #2 for combined system. 87

6.15 Comparison of experimental versus calculated response at accelerometer location #4 for combined system. 88

6.16 Location of accelerometers as instrumented on subsystem structure. 90

6.17 Experimental test data results for subsystem structure, accelerometer location #1. 90

6.18 First mode shape from finite element modal analysis of the subsystem structure. 91

6.19 Second mode shape from finite element modal analysis of the subsystem structure. 91

6.20 Comparison of experimental versus calculated response at accelerometer location #1 for subsystem structure. 92

6.21 Acceleration FRF from interface of combined system with envelope of peak amplitudes of accererometer #2. 94

6.22 Driving point accelerance FRF of subsystem structure with envelope of peak amplitudes. 94

6.23 Final input acceleration FRF for subsystem test using force-acceleration product method. 95

6.24 Maximum subsystem structure bending stress FRF resulting from force-acceleration product test method. 95

6.25 Force control spectrum shown as an envelope of peak interface force levels from combined system. 97

6.26 Final input acceleration FRF for subsystem test using the dual extremal control test method. 97

6.27 Maximum subsystem structure bending stress FRF resulting from dual extremal control test method. 98

FIGURE PAGE

6.28 Transmissibility FRF for top block of subsystem structure for use in transmissibility correction test method. 98

6.29 Final input acceleration FRF for subsystem test using the transmissibility correction test method. 99

6.30 Maximum subsystem structure bending stress FRF resulting from transmissibility correction test method. 99

6.31 Subsystem structure bending stress FRF comparing the three impedance methods vs field levels and an infinite impedance test. 101

7.1 Standard Missile 2 Block IIIA all-up-round assembly external configuration. 105

7.2 AUR field measurements resulting from rocket motor random vibration input in the longitudinal axis, hard-mounted IR seeker. 110

7.3 Acceleration control spectrum shown as an envelope of peak guidance section base interface levels, hard-mounted IR seeker. 110

7.4 Force control spectrum shown as an envelope of peak guidance section base interface levels, hard-mounted IR seeker. 111

7.5 Input acceleration spectrum comparing dual control against infinite impedance method for longitudinal axis, hard-mounted IR seeker. 111

7.6 Guidance section test results for dual control and infinite impedance test methods, superimposed against field measurements, hard-mounted IR seeker. 112

7.7 AUR field measurements resulting from rocket motor random vibration input in the longitudinal axis, isolated IR seeker. 114

7.8 Acceleration control spectrum shown as an envelope of peak guidance section base interface levels, isolated IR seeker. 114

7.9 Force control spectrum shown as an envelope of peak guidance section base interface levels, isolated IR seeker. 115

7.10 Input acceleration spectrum comparing dual control against infinite impedance method for longitudinal axis, isolated IR seeker. 115

FIGURE PAGE

7.11 Guidance section test results for dual control and infinite impedance test methods, superimposed against field measurements, isolated IR seeker. . . 116

8.1 Diagram for dual extremal control of acceleration and force using conventional test equipment. 122

8.2 Sensitivity of mean-square acceleration of load mass to mean-square free acceleration of source mass when $\omega_2 = \omega_1$. 126

A.1 Acceleration of m_5 comparing 10-DOF field results to those obtained from subsystem *II* test using force-acceleration. 136

A.2 Acceleration of m_6 comparing 10-DOF field results to those obtained from subsystem *II* test using force-acceleration. 136

A.3 Acceleration of m_7 comparing 10-DOF field results to those obtained from subsystem *II* test using force-acceleration. 137

A.4 Acceleration of m_5 comparing 10-DOF field results to those obtained from subsystem *II* test using dual control. 137

A.5 Acceleration of m_6 comparing 10-DOF field results to those obtained from subsystem *II* test using dual control. 138

A.6 Acceleration of m_7 comparing 10-DOF field results to those obtained from subsystem *II* test using dual control. 138

A.7 Acceleration of m_5 comparing 10-DOF field results to those from subsystem *II* test using transmiss. correction. 139

A.8 Acceleration of m_6 comparing 10-DOF field results to those from subsystem *II* test using transmiss. correction. 139

A.9 Acceleration of m_7 comparing 10-DOF field results to those from subsystem *II* test using transmiss. correction. 140

A.10 Acceleration FRF of m_5 comparing the three impedance test methods vs. an infinite impedance test for subsystem *II*. 140

A.11 Acceleration FRF of m_6 comparing the three impedance test methods vs. an infinite impedance test for subsystem *II*. 141

FIGURE PAGE

A.12 Acceleration FRF of m_7 comparing the three impedance test methods vs. an infinite impedance test for subsystem *II*. 141

B.1 Fabrication drawing of beam and block test structure - sheet 1. 143

B.2 Fabrication drawing of beam and block test structure - sheet 2. 144

B.3 Fabrication drawing of beam and block test structure - sheet 3. 145

B.4 Fabrication drawing of beam and block test structure - sheet 4. 146

LIST OF SYMBOLS

a	acceleration
A_S	acceleration control specification
$\hat{A}$	accelerance, complex impedance variable
c	coefficient of viscous damping
$\hat{C}$	compliance, complex impedance variable
D	sum of fractional damage
$\hat{E}$	effective mass, complex impedance variable
f	natural cyclic frequency
f	force
F, F_S	force magnitude, force control specification
g	acceleration of gravity
$H(\omega)$	complex frequency response function
i	square root of -1
k	spring constant
K, $K(\omega)$	stiffness matrix, control level
$\hat{K}$	dynamic stiffness, complex impedance variable
m	mass
M	mass matrix, mass ratio
n, N	number of cycles
$S(\omega)$, S	power spectral density function, stress
t	time
x	absolute displacement
$\dot{x}$	absolute velocity
$\ddot{x}$	absolute acceleration
X	displacement magnitude
y	relative displacement
$\dot{y}$	relative velocity
$\ddot{y}$	relative acceleration
$\hat{Y}$	mobility, complex impedance variable
$\hat{Z}$	mechanical impedance, complex impedance variable
ζ	viscous damping ratio
θ	phase angle
σ	standard deviation, root-mean-square
$\Phi(x)$, $\phi(x)$	mean-square value of x
ω	natural circular frequency
∞	infinity

LIST OF ACRONYMS

AUR	all-up-round
DEC	dual extremal control impedance method
DOF	degree-of-freedom
FAP	force-acceleration product impedance method
FEA	finite element analysis
FEM	finite element model
FRF	frequency response function
Hz	Hertz, cycles per second
IR	infrared
MR	medium range
MS	missile station
PSD	power spectral density
RF	radio frequency
RMS	root-mean-square
SM-2	standard missile 2
TC	transmissibility correction impedance method

CHAPTER 1

INTRODUCTION

The generation of suitable vibration design and test specifications for missile equipment, using mechanical impedance methods, is the focus of this work. The resistance of guided missile equipment to airborne vibrations during flight is an important design factor. Well formulated and realistic vibration requirements are critical because of the great penalties involved if an equipment item is either over or under designed. A large proportion of the work being done on vibration is concerned with producing equipment designs which can withstand the dynamic loads that might occur in service. On the basis of field measurements, design conditions are selected and are backed up by specification of a vibration test that the completed equipment will have to pass.

The Problem

Since the beginnings of the shock and vibration field as we know it today, measurements have been carried out almost exclusively in terms of motion rather than in terms of force; test requirements have likewise been stated almost exclusively in terms of motion. This practice was certainly not the result of careful examination of all factors relevant to the choice. More likely, it began out of expediency, with little more justification than an apparent convenience. Motion measuring instruments can be installed on structure, where an item of equipment is mounted, for example, with little change in the structure. Measurements of the force applied by the structure to the equipment would require insertion of a measuring instrument between the structure and the equipment and functioning as part of the transmission path.

In interpreting the data and deriving test requirements, the effect of dynamic loading of the structure by the item of equipment has often been neglected. The loading effect has a subtle relation to the derivation of test requirements. Vibration spectra are usually somewhat jagged. Test requirements are invariably written in terms of smooth spectra. This is done partly for simplicity in clerical work, setup effort and test procedure, and partly to simulate a composite vibration condition. In other words, it is assumed that the particular frequencies at which spectral peaks of vibration occur are not coincidental; consequently the equipment must operate without malfunction or failure when excited by a vibration whose spectrum is a simple envelope of the composite peaks. It may happen, however, that a spectral valley persists (antiresonance) in spite of changes in the amount of propellant on board, etc., and is actually the effect of resonant dynamic loading of the structure by the equipment item. The test condition thus drastically overtests this item.

Mechanical Impedance History

The relation of driving force to the acceleration that a support structure imparts to a mounted equipment item is conveniently expressed through the use of mechanical impedance variables. Impedance variables contain ratios of input force to resulting input acceleration (or input acceleration to input force). Mechanical impedance as a concept originated by analogy to the theory of electrical multiport networks [1]. Mechanical impedance applications for vibration testing had its inception in the 1960's, predominantly driven by the requirements of the manned space program and for the desire to more accurately simulate field vibration in the laboratory test [2-4].

The conceptual foundations of mechanical impedance were laid down during this period of time. Many papers were generated detailing the benefits of mechanical

impedance testing and the basic incorrectness of a constant motion, infinite impedance simulation [1, 5-10]. However, it was generally concluded that real time control using impedance test methods was not easily achievable with the available test equipment of the time. Unfortunately, during the late 1970's and early 1980's much of the pioneering work done in the area of mechanical impedance testing was not enthusiastically pursued. This led to a tacit concordance of many aerospace contractors and their customers that performing infinite impedance testing (ignoring dynamic loading of an equipment item against its support) was a conservative solution to equipment design and testing needs. Conservatism in itself is not a bad idea; however blind conservatism, inherent in infinite impedance testing, can be very costly to missile manufacturers.

The late 1980's up to the present has seen a revitalized interest in using mechanical impedance vibration testing. Much of this new found interest originates partly out of necessity and partly because of much improved force measuring instruments and vibration control test equipment. Unnecessarily damaging very expensive one-of-a-kind space vehicles prompted the national laboratories to pursue more realistic testing techniques [11]. The advent of high speed computers has also rendered mechanical impedance testing an attractive alternative to infinite impedance testing.

Thesis Organization

The work presented here attempts to explore the conceptual problems inherent with infinite impedance vibration testing. Several alternative test methods, based on mechanical impedance concepts, are presented and demonstrated. The establishment of a rational procedure to execute impedance methods is suggested, and implementation of impedance methods into a vibration test facility is described.

The significance of antiresonance versus resonance is examined in Chapter 2 and a method is developed to calculate antiresonace frequencies for a multi-degree-of-freedom system. The amount of overtest that can result with an envelope of spectral peaks method is demonstrated. The dynamic interaction between masses of a two-degree-of-freedom system is thoroughly evaluated in Chapter 3. Dimensionless system parameters are varied over a wide range to characterize the influence one system has upon the other. The study of this simple system reveals the range of system parameters where dynamic loading can be considered significant and should be accounted for in an equipment test.

In Chapter 4 several mechanical impedance variables are defined and application of impedance techniques, to account for the connection of subsystems is presented. The calculation of interface force and acceleration is accomplished using impedance variables. The various impedance methods that can be used to account for dynamic interaction between equipment and support are evaluated in Chapter 5. Three methods are selected as the most promising: (1) force-acceleration product technique, where input acceleration is controlled as the product of force times acceleration, (2) dual extremal control method, which establishes both a force and acceleration control spectrum, and (3) transmissibility correction method, which corrects the input acceleration by the equipment transmissibility function. Each method is derived and then demonstrated using a multiple degree-of-freedom model.

Comparison of the three impedance techniques based on vibration equivalence is discussed in Chapter 6. Total accumulated damage is calculated for each method using a simple beam structure. Experimental vibration testing is performed and finite element analysis is used to determine cumulative damage. Application of mechanical impedance

methods to an aerospace design problem is performed in Chapter 7. A Standard Missile-2 design upgrade is evaluated using impedance concepts.

The philosophy behind establishing a rational procedure to implement mechanical impedance methods is discussed in Chapter 8. The various options available to calculate a force control spectrum for use in the dual control test method are presented, and a brief discussion on the necessary test equipment to implement the impedance testing techniques is described.

While the objective of taking dynamic loading into account is subject to some practical restraints, it may be possible to gain considerable improvement in vibration simulation realism. Employing experimental impedance measurements coupled with a well developed finite element computer model can virtually eliminate the possibility of unnecessarily damaging good hardware (a common occurrence with infinite impedance testing). The application of these techniques is straightforward and can be implemented in an existing product line test program or can be used in design and development of new missile systems. Elimination of the blind conservatism associated with infinite impedance testing will most likely save considerable time and money while providing greater insight into the dynamics of the structure at hand.

CHAPTER 2

SPECTRAL ENVELOPING AND RESONANCE VS. ANTIRESONANCE

It is common practice to present flight vibration data as some form of plot of motion amplitude (typically acceleration) versus frequency; sinusoidal vibration is shown in this way; and random vibration is analyzed in terms of spectral density. When such data is obtained on airborne structures, it is almost universal practice to record the motion of the points of attachment of equipment to the supporting structure. These plots usually show one or more characteristic peaks along with characteristic valleys (see Fig. 2.1). The characteristic peaks correspond to certain natural frequencies of the missile as a whole, including equipment. After several such plots that are considered to be pertinent to a given equipment item have been gathered together, the data is usually synthesized into a single simpler spectrum for design and test requirements. Since a margin of safety is desirable, the synthesized spectrum is usually a smooth simple curve whose level is determined principally by the peaks of a spectrum that is a composite of the original spectra.

The Infinite Impedance Vibration Test

At first glance it seems reasonable to require an equipment item to withstand the maximum intensities of vibration that are observed to occur during flight. However, this seemingly straightforward procedure must be viewed incredulously because it requires the neglect of the influence of the reactions of a mounted equipment item upon its supporting structure. Vibration specifications derived in the manner described require that a vibration shaker mounting platform deliver a prescribed motion regardless of the reaction

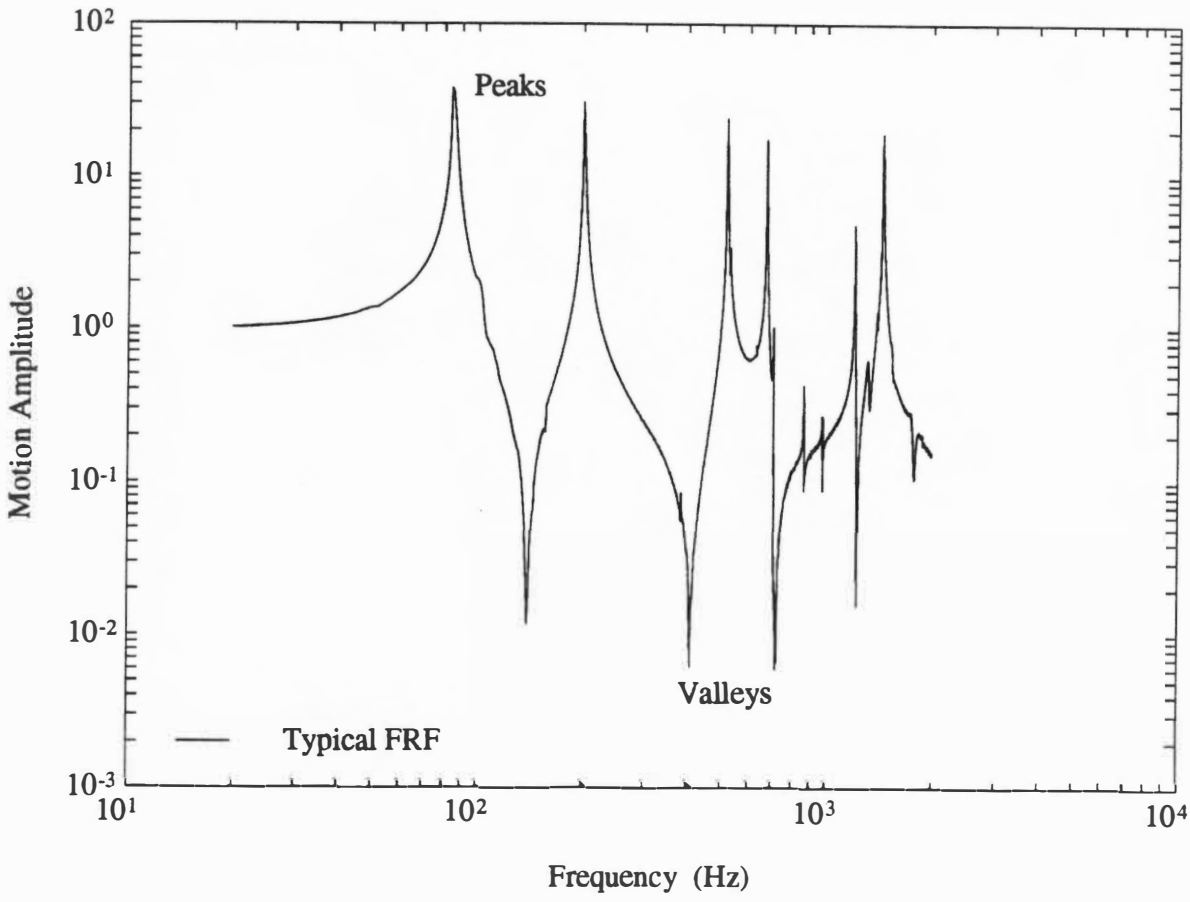

Figure 2.1 **Typical frequency response function displaying characteristic peaks and characteristic valleys.**

of the unit under test. Input acceleration to the test specimen is maintained at the prescribed level regardless of the force magnitude required to sustain this acceleration. This amounts to testing with an infinite impedance vibration source and thus implies that the actual equipment support structure (missile airframe) must have an infinite effective mass at all frequencies. This test method is referred to as infinite impedance vibration testing [1].

Dynamic Loading and Antiresonance

The supporting structure does not possess infinite effective mass at any frequency and the vibratory motion of the supporting structure can be significantly affected by the interface reactions of the coupled equipment item. This alteration of motion is known as dynamic loading. At a certain frequency an equipment item may exert an unusually large reaction, or load, against support excitation. The reaction may be sufficient to reduce components at this frequency existing in the excitation to relatively small values. If the support excitation is a sinusoidal vibration (or random vibration), then the frequency response function (FRF) of the support will exhibit a notch or characteristic valley at this frequency.

The frequency at which an equipment exerts maximum reaction against an excitation by its support is sometimes referred to as an antiresonance frequency [12]. The equipment, from the viewpoint of its support, has a maximum value of mechanical impedance at this frequency. When the support structure is the lowest level in the mechanical system, then the antiresonance frequency is independent of the characteristics of the support and depend only upon the characteristics of the mounted equipment. The determination of structural resonant frequencies (characteristic FRF peaks) is well

established and will not be reviewed here. The determination of structural antiresonance frequencies (characteristic FRF valleys) is less obvious and will be further evaluated.

Determination of Antiresonance Frequencies

The equations of motion for the five-degree-of-freedom (5-DOF), "free-free", dynamic chain system pictured in Fig. 2.2 are

$$\begin{aligned} m_1\ddot{x}_1 + k_1(x_1 - x_2) &= f_1 \\ m_2\ddot{x}_2 + k_1(x_2 - x_1) + k_2(x_2 - x_3) &= f_2 \\ m_3\ddot{x}_3 + k_2(x_3 - x_2) + k_3(x_3 - x_4) &= f_3 \\ m_4\ddot{x}_4 + k_3(x_4 - x_3) + k_4(x_4 - x_5) &= f_4 \\ m_5\ddot{x}_5 + k_4(x_5 - x_4) &= f_5 \end{aligned} \tag{2.1}$$

or in matrix notation can be expressed as

$$[M]\{\ddot{x}\} + [K]\{x\} = \{f\} \tag{2.2}$$

where

$$[M] = \begin{bmatrix} m_1 & 0 & 0 & 0 & 0 \\ 0 & m_2 & 0 & 0 & 0 \\ 0 & 0 & m_3 & 0 & 0 \\ 0 & 0 & 0 & m_4 & 0 \\ 0 & 0 & 0 & 0 & m_5 \end{bmatrix} \tag{2.3}$$

and

$$[K] = \begin{bmatrix} k_1 & -k_1 & 0 & 0 & 0 \\ -k_1 & k_1 + k_2 & -k_2 & 0 & 0 \\ 0 & -k_2 & k_2 + k_3 & -k_3 & 0 \\ 0 & 0 & -k_3 & k_3 + k_4 & -k_4 \\ 0 & 0 & 0 & -k_4 & k_4 \end{bmatrix} \tag{2.4}$$

If steady state harmonic input is assumed, that is, if $\{f_i\} = \{F_0\sin(\omega t)\}$, and the

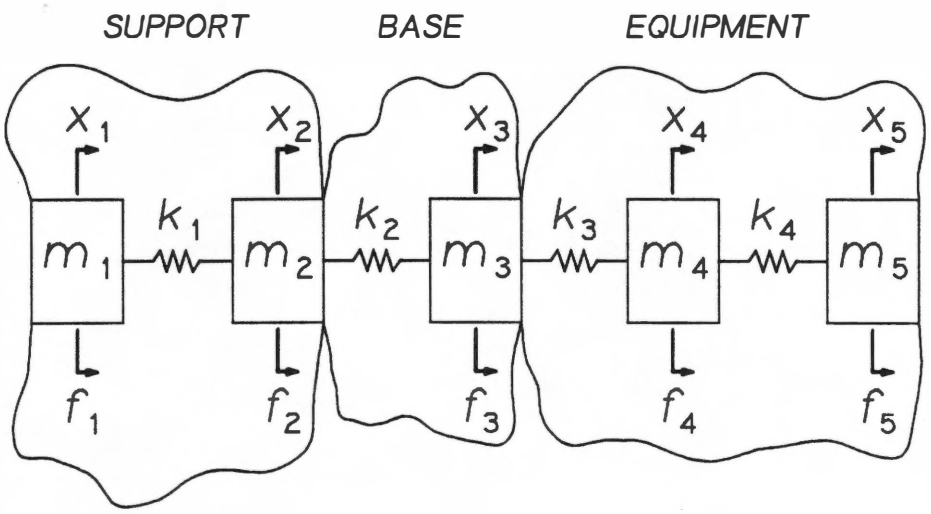

Figure 2.2 **Five-degree-of-freedom, free-free, dynamic chain system.**

displacement response is harmonic and of the form $\{x_i\} = \{X_i \sin(\omega t)\}$, the above set of governing differential equations will change to a set of simultaneous algebraic equations upon substitution of these expressions (and derivatives) into Eq. (2.2). The resulting substitution yields

$$([K] - \omega^2[M])\{X_i\} = \{F_0\} \tag{2.5}$$

Substitution of Eqs. (2.3) and (2.4) into Eq. (2.5) results in

$$[K_{EQV}]\{X_i\} = \{F_0\} \tag{2.6}$$

where $[K_{EQV}]$ is the equivalent stiffness matrix

$$[K_{EQV}] = \begin{bmatrix} k_1 - m_1\omega^2 & -k_1 & 0 & 0 & 0 \\ -k_1 & k_1 + k_2 - m_2\omega^2 & -k_2 & 0 & 0 \\ 0 & -k_2 & k_2 + k_3 - m_3\omega^2 & -k_3 & 0 \\ 0 & 0 & -k_3 & k_3 + k_4 - m_4\omega^2 & -k_4 \\ 0 & 0 & 0 & -k_4 & k_4 - m_5\omega^2 \end{bmatrix} \tag{2.7}$$

The solution for any X_i can be readily found by applying Cramer's rule to the simultaneous algebraic equations

$$X_i = \frac{|F|}{|X|} \tag{2.8}$$

where $|X|$ is the determinant of the coefficients of the X_i's (determinant of $[K_{EQV}]$) and $|F|$ is this determinant with the appropriate coefficient column replaced with the force column. To determine the antiresonance frequencies of the dynamic chain this ratio is set equal to zero:

$$X_i = \frac{|F|}{|X|} = 0 \tag{2.9}$$

To make this true the determinant of $|F|$ must equal zero. Therefore, a systematic method of determining antiresonance frequencies for a multi-degree-of-freedom system is established.

Application - Determination of Antiresonance Frequencies

The method described above is illustrated by the following demonstration. The case of the support structure (m_1 and m_2 of Fig. 2.2) as the input forcing function is used as an example ($f_3 = f_4 = f_5 = 0$). The following convenient system parameters are defined for the sake of simplicity.

$$\begin{aligned} m_1 &= 4m & k_1 &= 5k \\ m_2 &= 3m & k_2 &= 3k \\ m_3 &= 3m & k_3 &= 4k \\ m_4 &= 2m & k_4 &= 1k \\ m_5 &= 1m \end{aligned} \tag{2.10}$$

Substitution of Eq. (2.10) into Eq. (2.7), the $[K_{EQV}]$ matrix becomes

$$[K_{EQV}] = \begin{bmatrix} 5k - 4m\omega^2 & -5k & 0 & 0 & 0 \\ -5k & 8k - 3m\omega^2 & -3k & 0 & 0 \\ 0 & -3k & 7k - 3m\omega^2 & -4k & 0 \\ 0 & 0 & -4k & 5k - 2m\omega^2 & -k \\ 0 & 0 & 0 & -k & k - m\omega^2 \end{bmatrix} \tag{2.11}$$

To determine the antiresonance frequencies from steady state harmonic loads applied to the support (m_1 and m_2), we substitute the appropriate force column into this matrix then take its determinant. For example, the antiresonance frequencies of the base

(m_3 of Fig. 2.2) are found by replacing column 3 of Eq. (2.11) with the force column and setting this determinant equal to zero.

$$\begin{vmatrix} 5k-4m\omega^2 & -5k & F_0 & 0 & 0 \\ -5k & 8k-3m\omega^2 & F_0 & 0 & 0 \\ 0 & -3k & 0 & -4k & 0 \\ 0 & 0 & 0 & 5k-2m\omega^2 & -k \\ 0 & 0 & 0 & -k & k-m\omega^2 \end{vmatrix} = 0 \qquad (2.12)$$

Expanding this gives

$$F_0(60k^4 - 129k^3m\omega^2 + 72k^2m^2\omega^4 - 12km^3\omega^6) = 0 \qquad (2.13)$$

Dividing through by F_0 and solving for ω, we get three roots

$$\omega_1 = \sqrt{\frac{7k}{4m} - \frac{\sqrt{17}\,k}{4m}} \qquad \omega_2 = \sqrt{\frac{5k}{2m}} \qquad \omega_3 = \sqrt{\frac{7k}{4m} + \frac{\sqrt{17}\,k}{4m}} \qquad (2.14)$$

Since three roots resulted from expansion of this determinant, the m_3 base will experience three response antiresonances, at frequencies ω_1, ω_2 and ω_3.

To validate this method, this technique is numerically applied to the 5-DOF dynamic model. For this numerical problem the following values are used: m = 2 lb_m, k = 10,000 lb_f/in, and F_0 = 20 lb_f (steady-state harmonic loading). Substitution of these values into Eq. (2.10) yields

$$\begin{aligned} m_1 &= 8 & k_1 &= 50{,}000 \\ m_2 &= 6 & k_2 &= 30{,}000 \\ m_3 &= 6 & k_3 &= 40{,}000 \\ m_4 &= 4 & k_4 &= 10{,}000 \\ m_5 &= 2 \end{aligned} \qquad (2.15)$$

Figs. 2.3 and 2.4 display the FRF plots for each mass resulting from harmonic forces

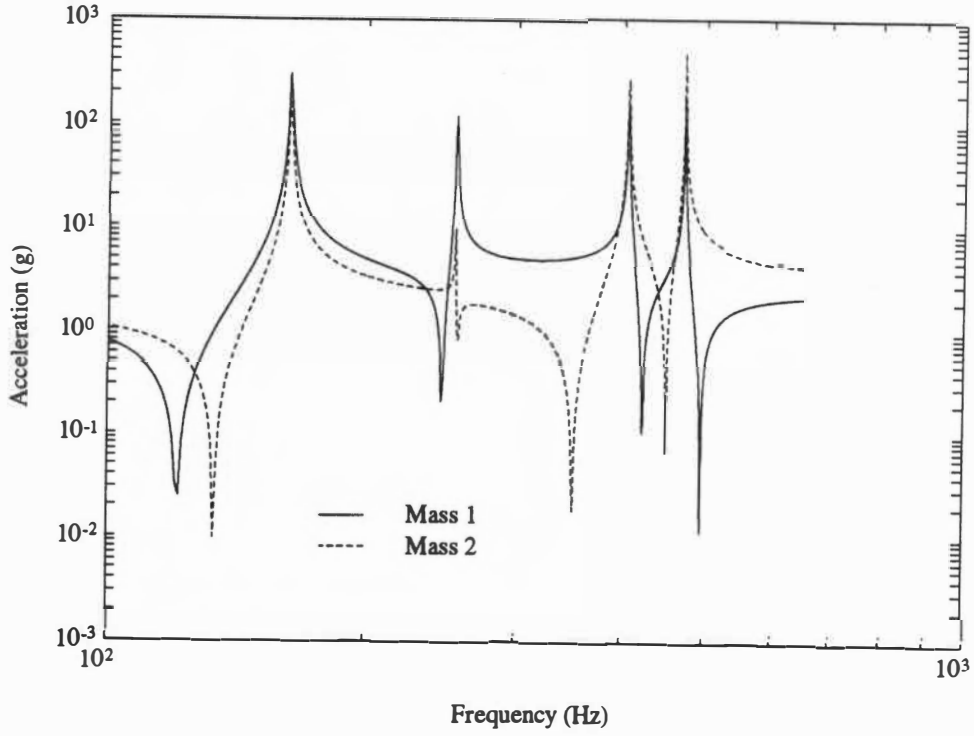

Figure 2.3 FRF of m_1 and m_2 resulting from harmonic loading at structure support masses.

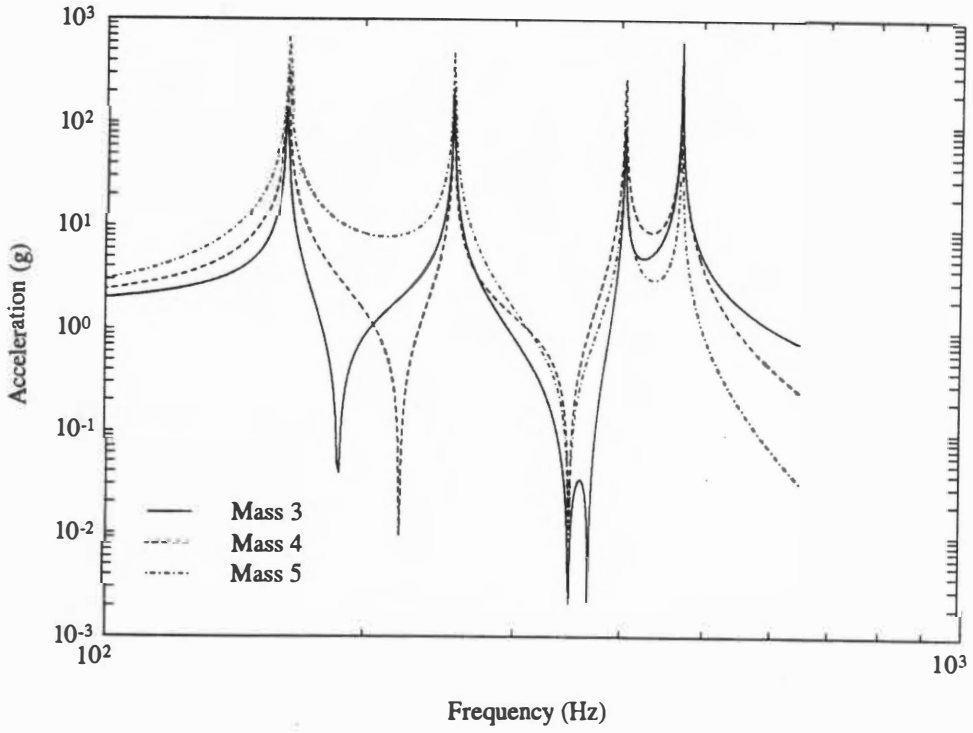

Figure 2.4 FRF of m_3, m_4, and m_5 resulting from harmonic loading at structure support masses.

applied to the support masses (m_1 and m_2). A frequency range from 100 to 650 Hz in ½ Hz increments is used. Acceleration response amplitudes are calculated at every frequency point (in g units, where $1g$ = 386 in/s^2). The resulting 5-DOF system antiresonance frequencies are then compared to the predicted theoretical antiresonance frequencies. Table 2.1 compares the antiresonance frequencies obtained from the two methods. The antiresonance frequencies obtained from the 5-DOF simulation results (Compute column, Table 2.1) correlate extremely well with those predicted from the derived, theoretical method (Theory column, Table 2.1).

Infinite Impedance Overtest

Though quite common, the use of an envelope of spectral peaks to determine vibration test levels for use in standard test procedures does not account for the occurrence of characteristic valleys (antiresonance). In other words, the dynamic loading of the equipment against its support is neglected. At test, the use of an envelope test spectrum thus will result in rather accurate vibration responses of the equipment item only close to the resonance frequencies of the combined system in the field. At all other frequencies, the response levels may be grossly in error particularly close to the fixed base natural frequencies of the equipment item (antiresonance frequencies of combined system).

To quantify the magnitude of error that can occur, a test specification based on the results of the 5-DOF system is developed and applied to the equipment only subsystem (m_4 and m_5 of Fig. 2.2). Fig. 2.5 shows the test specification as an envelope of the m_3 base characteristic peaks from the 5-DOF field results. This envelope is then applied to the equipment only subsystem as input for a hypothetical infinite impedance vibration test. Figs. 2.6 and 2.7 display the results of the equipment only subsystem test superimposed

Table 2.1 5-DOF antiresonance frequencies - theory versus computed

Harmonic Loading At Support Masses	Antiresonance Frequencies (Hz)									
	Mass 1		Mass 2		Mass 3		Mass 4		Mass 5	
	Theory	Compute	Theory	Compute	Theory	Compute	Theory	Compute	Theory	Compute
Mass 1 & Mass 2	120.57	120.5	133.15	133.0	187.53	187.5	221.13	221.0	349.64	349.5
	245.44	245.5	255.34	255.5	349.64	349.5	349.64	349.5		
	422.41	422.5	349.64	394.5	368.75	368.5				
	493.89	494.0	449.80	450.0						

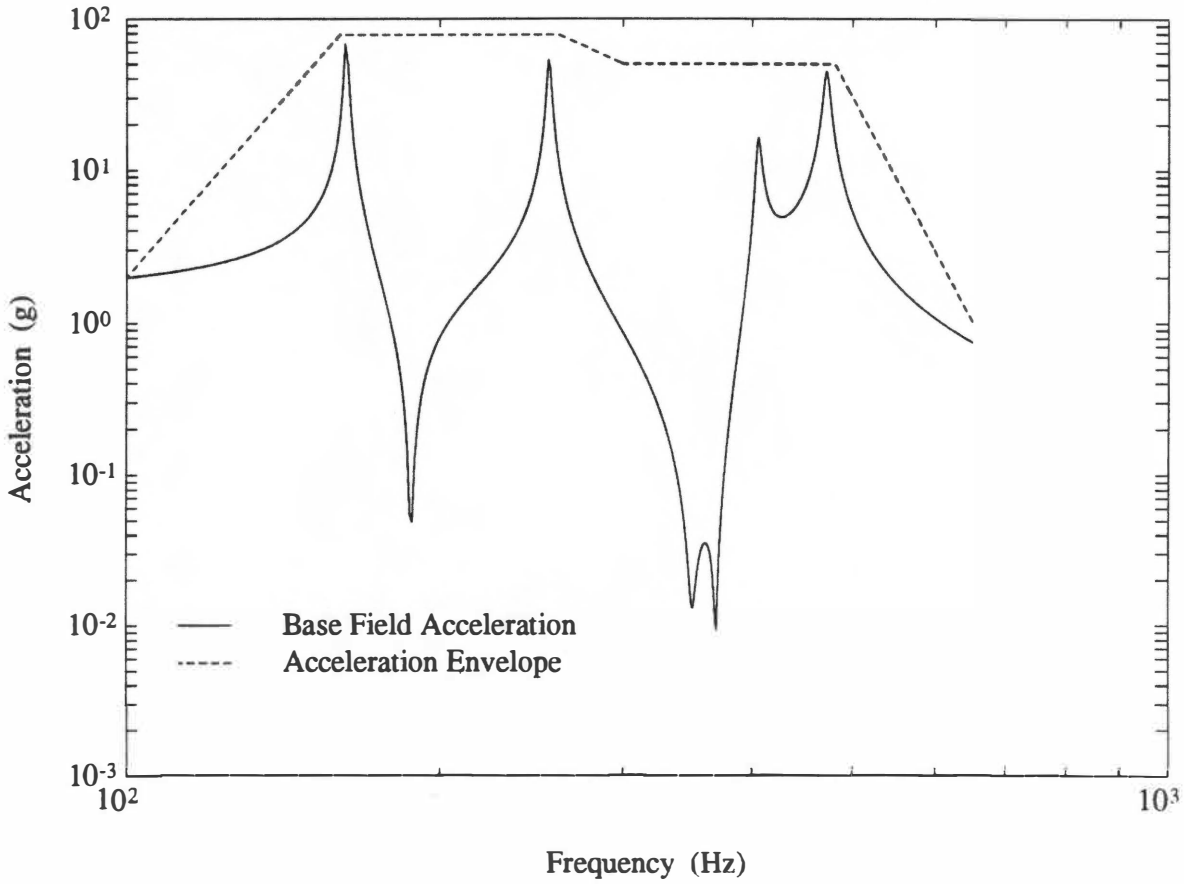

Figure 2.5 Acceleration test specification as an envelope of m_3 base field acceleration levels.

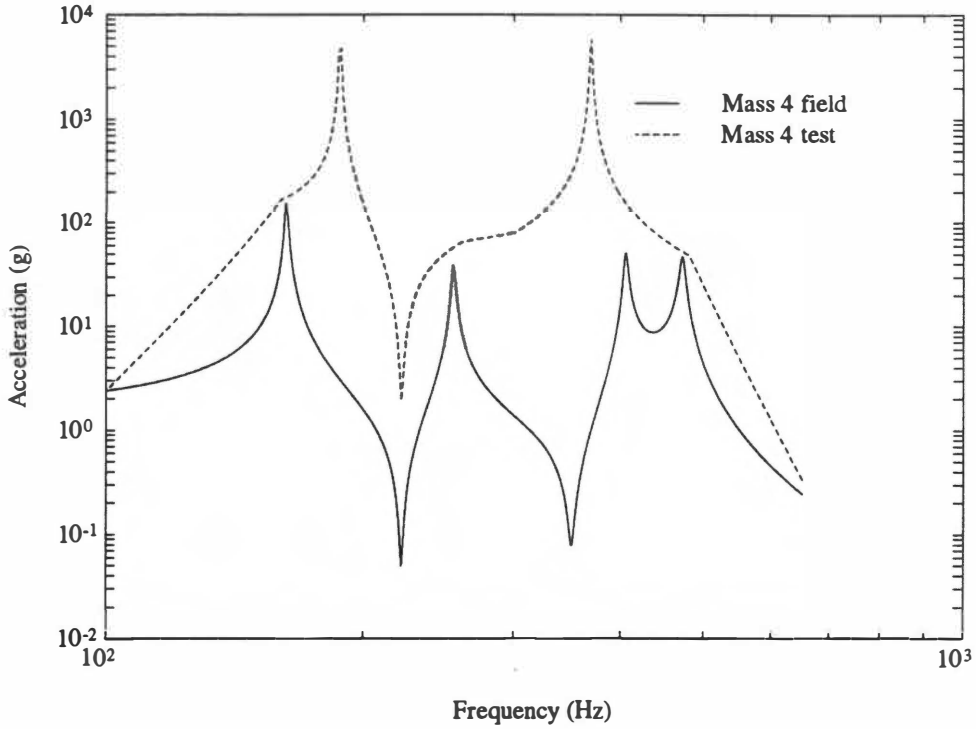

Figure 2.6 FRF of m_4 field results from 5-DOF system versus hypothetical infinite impedance equipment test.

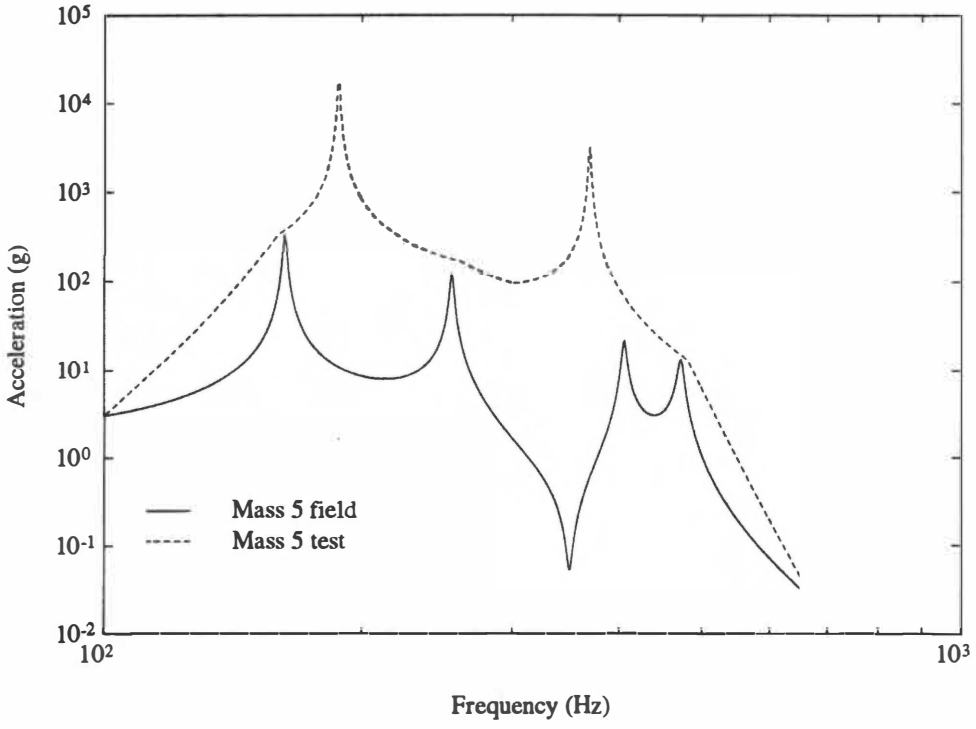

Figure 2.7 FRF of m_5 field results from 5-DOF system versus hypothetical infinite impedance equipment test.

against the field results from the original 5-DOF system. As can be observed, the amount of overtest is in error by a factor of 37 for m_4 response (153 g's field results vs. 5,720 g's equipment test) and by a factor of 52 for m_5 response (330 g's field vs. 17,097 g's equipment). Obviously, an unacceptable amount of overtesting resulted for this undamped mechanical system. The presence of structural damping will attenuate the amount of overtest error.

The magnitude of overtest error is dependent on the dynamic properties of both the equipment and supporting structure. If the interface reactions between the equipment item and its support are significant, dynamic loading of the equipment item against its support will occur. Performing an infinite impedance equipment test using enveloping techniques, as described above, will surely result in severe overtesting. What is considered significant dynamic loading? Often, the assumption that the dynamic properties of the equipment item are negligibly small compared to the supporting structure is used as a justification for infinite impedance vibration testing. This assumption needs to be investigated to characterize the effect the two systems have on each other. The dynamic interaction between connected mechanical systems is the topic of the next chapter.

CHAPTER 3

DYNAMIC INTERACTION BETWEEN EQUIPMENT AND SUPPORT

The dynamic interaction between an equipment item and its supporting structure can be characterized by using the classical two-degree-of-freedom system (2-DOF) shown in Fig. 3.1. The interaction and response of this dynamic system are well known. However, the degree of interaction will depend on the system parameters m_1, k_1, c_1, and m_2, k_2, c_2. It is this degree of interaction that is of interest. By performing a parametric study of the 2-DOF system, the degree of interaction can be realized.

Response Parameters

Curtis/Boykin [13] and Crandall/Mark [14] suggested a method for performing a 2-DOF parametric study by using random, white noise base excitation and calculating the resulting mean square responses. This is accomplished by use of the complex frequency response $H(\omega)$ method. It is a property of linear, time invariant systems that when the excitation is steady state harmonic motion then the response is also steady state harmonic motion at the same frequency. The excitation, X, is related to the response, Y, through the complex frequency response function $H(\omega)$, or more precisely $X \times H(\omega) = Y$. Since $H(\omega)$ is essentially an output measure for unit input its dimensions will have the dimensions of the quotient Y/X.

The excitation is the motion of the base, which is considered to be described by its acceleration $\ddot{x}_0$. Four different responses will be examined: the relative displacements $y_1 = x_1 - x_0$ and $y_2 = x_2 - x_1$ and the absolute accelerations of the two masses, $\ddot{x}_1$ and $\ddot{x}_2$.

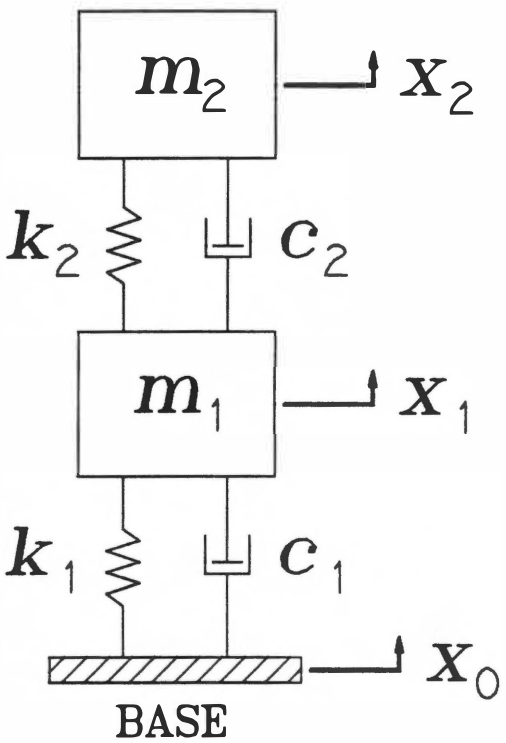

Figure 3.1 Two-degree-of-freedom system with base input motion for parametric study.

The equations of motion in terms of the relative displacements are

$$\begin{aligned} m_1\ddot{y}_1 + c_1\dot{y}_1 + k_1y_1 - c_2\dot{y}_2 - k_2y_2 &= -m_1\ddot{x}_0 \\ m_2(\ddot{y}_1 + \ddot{y}_2) + c_2\dot{y}_2 + k_2y_2 &= -m_2\ddot{x}_0 \end{aligned} \tag{3.1}$$

which connect the response quantities y_1 and y_2 with the excitation $\ddot{x}_0$. When y_1 and y_2 are known, the remaining response quantities $\ddot{x}_1$ and $\ddot{x}_2$ are found by substituting $\ddot{x}_1 = \ddot{x}_0 + \ddot{y}_1$ and $\ddot{x}_2 = \ddot{x}_0 + \ddot{y}_1 + \ddot{y}_2$ into Eq. (3.1), resulting in

$$\begin{aligned} m_1\ddot{x}_1 &= -c_1\dot{y}_1 - k_1y_1 + c_2\dot{y}_2 + k_2y_2 \\ m_2\ddot{x}_2 &= -c_2\dot{y}_2 - k_2y_2 \end{aligned} \tag{3.2}$$

The following convenient notation for the uncoupled natural frequencies ω_1 and ω_2, the uncoupled damping ratios ζ_1 and ζ_2, and the mass ratio M of the 2-DOF system is introduced to standardize subsequent treatment

$$\begin{aligned} \omega_1 &= \sqrt{\frac{k_1}{m_1}} \qquad \zeta_1 = \frac{c_1}{2m_1\omega_1} \qquad M = \frac{m_2}{m_1} \\ \omega_2 &= \sqrt{\frac{k_2}{m_2}} \qquad \zeta_2 = \frac{c_2}{2m_2\omega_2} \end{aligned} \tag{3.3}$$

The first pair of complex frequency response functions $H_{y1}(\omega)$ and $H_{y2}(\omega)$ are obtained analytically by substituting

$$\ddot{x}_0 = e^{i\omega t} \qquad y_1 = H_{y1}(\omega)e^{i\omega t} \qquad y_2 = H_{y2}(\omega)e^{i\omega t} \tag{3.4}$$

into Eq. (3.1), canceling the $e^{i\omega t}$ terms, and solving algebraically for $H(\omega)$.

$$H_{y1}(\omega) = \frac{\omega^2 - i\omega(1+M)2\zeta_2\omega_2 - (1+M)\omega_2^2}{\omega^4 - i\omega^3[2\zeta_1\omega_1 + 2(1+M)\zeta_2\omega_2] - \omega^2[\omega_1^2 + (1+M)\omega_2^2 + 4\zeta_1\zeta_2\omega_1\omega_2] + i\omega[2\zeta_1\omega_1\omega_2^2 + 2\zeta_2\omega_2\omega_1^2] + \omega_1^2\omega_2^2} \tag{3.5}$$

$$H_{y2}(\omega) = \frac{-i\omega 2\zeta_1\omega_1 - \omega_1^2}{\omega^4 - i\omega^3[2\zeta_1\omega_1 + 2(1+M)\zeta_2\omega_2] - \omega^2[\omega_1^2 + (1+M)\omega_2^2 + 4\zeta_1\zeta_2\omega_1\omega_2] + i\omega[2\zeta_1\omega_1\omega_2^2 + 2\zeta_2\omega_2\omega_1^2] + \omega_1^2\omega_2^2} \tag{3.6}$$

The last pair of frequency response functions are obtained by substituting in Eqs. (3.4), (3.5) and (3.6) into Eq. (3.2).

$$H_{\ddot{x}1}(\omega) = \frac{-i\omega^3 2\zeta_1\omega_1 - \omega^2(\omega_1^2 + 4\zeta_1\zeta_2\omega_1\omega_2) + i\omega(2\zeta_1\omega_1\omega_2^2 + 2\zeta_2\omega_2\omega_1^2) + \omega_1^2\omega_2^2}{\omega^4 - i\omega^3[2\zeta_1\omega_1 + 2(1+M)\zeta_2\omega_2] - \omega^2[\omega_1^2 + (1+M)\omega_2^2 + 4\zeta_1\zeta_2\omega_1\omega_2] + i\omega[2\zeta_1\omega_1\omega_2^2 + 2\zeta_2\omega_2\omega_1^2] + \omega_1^2\omega_2^2} \tag{3.7}$$

$$H_{\ddot{x}2}(\omega) = \frac{-\omega^2 4\zeta_1\zeta_2\omega_1\omega_2 + i\omega(2\zeta_1\omega_1\omega_2^2 + 2\zeta_2\omega_2\omega_1^2) + \omega_1^2\omega_2^2}{\omega^4 - i\omega^3[2\zeta_1\omega_1 + 2(1+M)\zeta_2\omega_2] - \omega^2[\omega_1^2 + (1+M)\omega_2^2 + 4\zeta_1\zeta_2\omega_1\omega_2] + i\omega[2\zeta_1\omega_1\omega_2^2 + 2\zeta_2\omega_2\omega_1^2] + \omega_1^2\omega_2^2} \tag{3.8}$$

It is desired to obtain the mean square values of the response parameters. If the motion of the base is a random excitation whose instantaneous values in an arbitrarily narrow frequency band have a normal probability density function, the excitation may be expressed by the power spectral density (PSD) function $S(\omega)$. The relation between the PSD of the excitation $S_X(\omega)$ and the PSD of the response $S_Y(\omega)$ is

$$S_Y(\omega) = |H(\omega)|^2 S_X(\omega) \tag{3.9}$$

The mean square $\Phi(Y^2)$ of the stationary response process Y can be obtained when the spectral density of the excitation is known.

$$\Phi(Y^2) = \int_{-\infty}^{\infty} S_Y(\omega)\,d\omega = \int_{-\infty}^{\infty} |H(\omega)|^2 S_X(\omega)\,d\omega \tag{3.10}$$

However, since the input excitation is assumed to be ideal white noise, $S_X(\omega) = S_0$, a constant for all frequencies, the integral then reduces to

$$\Phi(Y^2) = S_0 \int_{-\infty}^{\infty} |H(\omega)|^2\,d\omega \tag{3.11}$$

The closed form solution to this integral, for each frequency response function $H(\omega)$, can be determined [14] by using a general form of $H(\omega)$

$$H(\omega) = \frac{-i\omega^3 B_3 - \omega^2 B_2 + i\omega B_1 + B_0}{\omega^4 A_4 - i\omega^3 A_3 - \omega^2 A_2 + i\omega A_1 + A_0} \tag{3.12}$$

The integral for the general form of $H(\omega)$ is

$$\int_{-\infty}^{\infty} |H(\omega)|^2\,d\omega =$$

$$\pi \frac{\left(\frac{B_0^2}{A_0}\right)(A_2A_3 - A_1A_4) + A_3(B_1^2 - 2B_0B_2) + A_1(B_2^2 - 2B_1B_3) + \left(\frac{B_3^2}{A_4}\right)(A_1A_2 - A_0A_3)}{A_1(A_2A_3 - A_1A_4) - A_0A_3^2} \tag{3.13}$$

The four mean square responses are obtained by substitution of the appropriate A and B constants, from each frequency response function (Eqs. 3.5 through 3.8), into the general solution formula (Eq. 3.13).

$$\Phi(y_1^2) = [\pi S_0] \frac{\begin{array}{c} 2\zeta_1\omega_1\omega_2^2[M^2 + M(1+M)^2(\omega_2/\omega_1)^2] + 2\zeta_2\omega_2\omega_1^2\{[1 \\ -(1+M)^2(\omega_2/\omega_1)^2]^2 + M(1+M)^2(\omega_2/\omega_1)^2\} + 8\zeta_1\zeta_2^2\omega_1\omega_2^2(1+M)^2[1 \\ +(1+M)(\omega_2/\omega_1)^2] + 8\zeta_2^3\omega_2^3(1+M)^2[(1+M) + (\zeta_1/\zeta_2)^2] \end{array}}{\begin{array}{l} 4\omega_1\omega_2\{M\omega_1\omega_2(\zeta_1\omega_2 + \zeta_2\omega_1)^2 + \zeta_1\zeta_2[\omega_1^2 - (1+M)\omega_2^2]^2 \\ + 4\zeta_1\zeta_2\omega_1\omega_2[\omega_1\omega_2(\zeta_1^2 + (1+M)\zeta_2^2) + \zeta_1\zeta_2(\omega_1^2 + (1+M)\omega_2^2)]\} \end{array}} \tag{3.14}$$

$$\Phi(y_2^2) = [\pi\omega_1^2 S_0] \frac{\begin{array}{c} 2\zeta_1\omega_1[M + (\omega_1/\omega_2)^2] + 2\zeta_2\omega_2[(1+M)^2 + M(\omega_1/\omega_2)^2] \\ +8\zeta_1\zeta_2\{\zeta_1\omega_2[1 + M + (\omega_1/\omega_2)^2] + \zeta_2\omega_1[1 + M + (\zeta_1/\zeta_2)^2]\} \end{array}}{\begin{array}{l} 4\omega_1\omega_2\{M\omega_1\omega_2(\zeta_1\omega_2 + \zeta_2\omega_1)^2 + \zeta_1\zeta_2[\omega_1^2 - (1+M)\omega_2^2]^2 \\ + 4\zeta_1\zeta_2\omega_1\omega_2[\omega_1\omega_2(\zeta_1^2 + (1+M)\zeta_2^2) + \zeta_1\zeta_2(\omega_1^2 + (1+M)\omega_2^2)]\} \end{array}} \tag{3.15}$$

$$\Phi(\ddot{x}_1^2) = [2\pi\omega_1^2\omega_2 S_0] \frac{\begin{array}{c} M\zeta_1\omega_1\omega_2^3 + \zeta_2[(\omega_1^2 - (1+M)\omega_2^2)^2 + M\omega_1^2\omega_2^2] + 4\{\zeta_1^3 M\omega_1\omega_2^3 \\ +\zeta_1^2\zeta_2[(\omega_1^2 - \omega_2^2)^2 + \omega_1^2\omega_2^2 + M\omega_2^2] + \zeta_1\zeta_2^2[\omega_1^3\omega_2 + (1+M)\omega_1\omega_2^3] \\ +\zeta_2^3(1+M)\omega_1^2\omega_2^2\} + 16\omega_1\omega_2\zeta_1^2\zeta_2[(\zeta_1^2 + \zeta_2^2)\omega_1\omega_2 + (\omega_1^2 + \omega_2^2)\zeta_1\zeta_2] \end{array}}{\begin{array}{l} 4\omega_1\omega_2\{M\omega_1\omega_2(\zeta_1\omega_2 + \zeta_2\omega_1)^2 + \zeta_1\zeta_2[\omega_1^2 - (1+M)\omega_2^2]^2 \\ + 4\zeta_1\zeta_2\omega_1\omega_2[\omega_1\omega_2(\zeta_1^2 + (1+M)\zeta_2^2) + \zeta_1\zeta_2(\omega_1^2 + (1+M)\omega_2^2)]\} \end{array}} \tag{3.16}$$

$$\Phi(\ddot{x}_2^2) = [2\pi\omega_1^2\omega_2^2 S_0] \frac{\begin{array}{c} \zeta_1\omega_1(\omega_1^2 + M\omega_2^2) + \zeta_2\omega_2[M\omega_1^2 + (1+M)^2\omega_2^2] + 4\{\zeta_1^3\omega_1\omega_2^2 \\ +\zeta_1^2\zeta_2[\omega_1^2\omega_2 + (1+M)\omega_2^3] + \zeta_1\zeta_2^2[\omega_1^2 + (1+M)\omega_1\omega_2^2] \\ +\zeta_2^3(1+M)\omega_1^2\omega_2\} + 16\zeta_1^2\zeta_2^2\omega_1\omega_2(\zeta_1\omega_2 + \zeta_2\omega_1) \end{array}}{\begin{array}{l} 4\omega_1\omega_2\{M\omega_1\omega_2(\zeta_1\omega_2 + \zeta_2\omega_1)^2 + \zeta_1\zeta_2[\omega_1^2 - (1+M)\omega_2^2]^2 \\ + 4\zeta_1\zeta_2\omega_1\omega_2[\omega_1\omega_2(\zeta_1^2 + (1+M)\zeta_2^2) + \zeta_1\zeta_2(\omega_1^2 + (1+M)\omega_2^2)]\} \end{array}} \tag{3.17}$$

Dimensionless System Parameters

The dynamic characteristics of the 2-DOF system are evaluated by using the following dimensionless parameters: (1) the mass ratio $M = m_2/m_1$, (2) the frequency ratio ω_2/ω_1 between the uncoupled natural frequencies of each spring-mass system and (3) the damping ratios ζ_1 and ζ_2, associated with each spring-mass-damper system. In order to study the effects of variation of the dimensionless parameters, it is advantageous to normalize the mean square response values. The mean square responses of the relative

displacements, $\Phi(y_1^2)$ and $\Phi(y_2^2)$, are normalized in the subsequent plots by dividing by the mean square relative displacement that m_1 would have had under the same excitation if m_2 had been removed completely, i.e., with m_2 removed the system degenerates into the single-degree-of-freedom (1-DOF) system pictured in Fig 3.2. Similarly the mean square responses of the accelerations, $\Phi(\ddot{x}_1^2)$ and $\Phi(\ddot{x}_2^2)$, are normalized by dividing by the mean square acceleration that the first mass would have had under the same excitation if m_2 had been removed completely.

The relative displacement and absolute acceleration complex frequency response functions $H_{y_s}(\omega)$ and $H_{\ddot{x}_s}(\omega)$ for the 1-DOF system are obtained from the 2-DOF results by setting M, ζ_2, and ω_2 equal to zero in Eqs. (3.5) and (3.7) respectively.

$$H_{y_s}(\omega) = \frac{-1}{\omega_1^2 - \omega^2 + 2i\zeta_1\omega_1\omega} \qquad H_{\ddot{x}_s}(\omega) = \frac{i\omega(2\zeta_1\omega_1) + \omega_1^2}{\omega_1^2 - \omega^2 + 2i\zeta_1\omega_1\omega} \tag{3.18}$$

The mean square relative displacement $\phi(y_s^2)$ and the mean square absolute acceleration $\phi(\ddot{x}_s^2)$ for the 1-DOF system are similarly obtained from the 2-DOF mean square results by setting M, ζ_2, and ω_2 equal to zero in Eqs. (3.14) and (3.16) respectively.

$$\phi(y_s^2) = [\pi S_0]\frac{1}{2\zeta_1\omega_1^3} \qquad \phi(\ddot{x}_s^2) = [\pi\omega_1 S_0]\frac{1 + 4\zeta_1^2}{2\zeta_1} \tag{3.19}$$

Parametric Results

The first set of plots have uncoupled natural frequency ratio ω_2/ω_1 as abscissa and the normalized mean square responses $\Phi(y_1^2)/\phi(y_s^2)$, $\Phi(y_2^2)/\phi(y_s^2)$, $\Phi(\ddot{x}_1^2)/\phi(\ddot{x}_s^2)$, and $\Phi(\ddot{x}_2^2)/\phi(\ddot{x}_s^2)$ as ordinates. Each plot displays results for mass ratios ranging from $M = 1$ to $M = 0$ (where

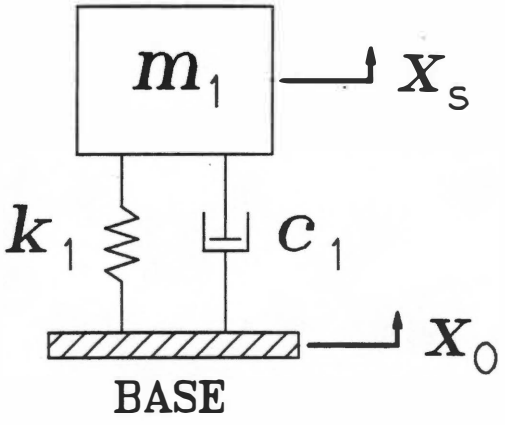

Figure 3.2 Single-degree-of-freedom system with base input motion for parametric study.

$M = 0$ being the case of an infinite m_1 source). Damping ratios were held constant for each plot ($\zeta_1 = \zeta_2 = 2\%$). The second set of plots have mass ratio M as abscissa and the normalized mean square responses as ordinates. Each of these plots display the results for uncoupled natural frequency ratios ω_2/ω_1 ranging from $\omega_2/\omega_1 = 0.4$ to $\omega_2/\omega_1 = 2.0$. Again, a constant damping ratio of $\zeta_1 = \zeta_2 = 2\%$ is used. The final set of plots have mass ratio M vs. normalized mean square response for a constant uncoupled natural frequency ratio of $\omega_2/\omega_1 = 1$. Each of these plots display the results for damping ratios ζ_1 and ζ_2 ranging from 1% to 10%.

Several general conclusions can be made from examination of plot set 1 (Figs. 3.3 through 3.6):

(1) When the coupling spring k_2 is relatively soft the uncoupled natural frequency ratio ω_2/ω_1 is small. Under these circumstances the relative displacement response of the first mass or the acceleration $\ddot{x}_1$ of this mass is not greatly effected by the presence of the second mass (Figs. 3.3 and 3.5). The mean square acceleration is affected earlier than the mean square relative displacement. Also, the larger the top mass the sooner the deviation.

(2) As ω_2/ω_1 becomes large compared to 1.0, the upper mass system has a high natural frequency (the coupling spring k_2 is relatively stiff) compared to the lower mass system, the relative displacement y_2 has a very small mean square value (Fig. 3.4) and both acceleration responses asymptotically become equal to each other and approach unity (Figs. 3.5 and 3.6). The displacement between the base and the first mass has a mean square response which, however, grows when the top mass is increased (Fig. 3.3).

(3) For values of uncoupled natural frequency ratio between 0.4 and 2.0 (which

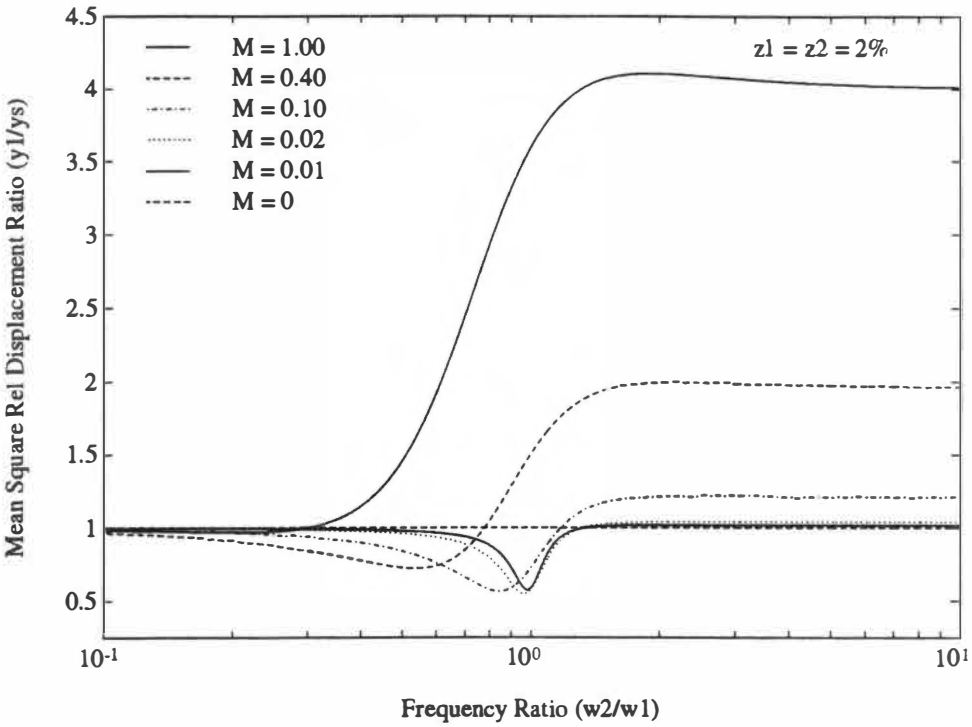

Figure 3.3 Mean square relative disp. of m_1 as a function of ω_2/ω_1 and M for $\zeta_1 = \zeta_2 = 2\%$

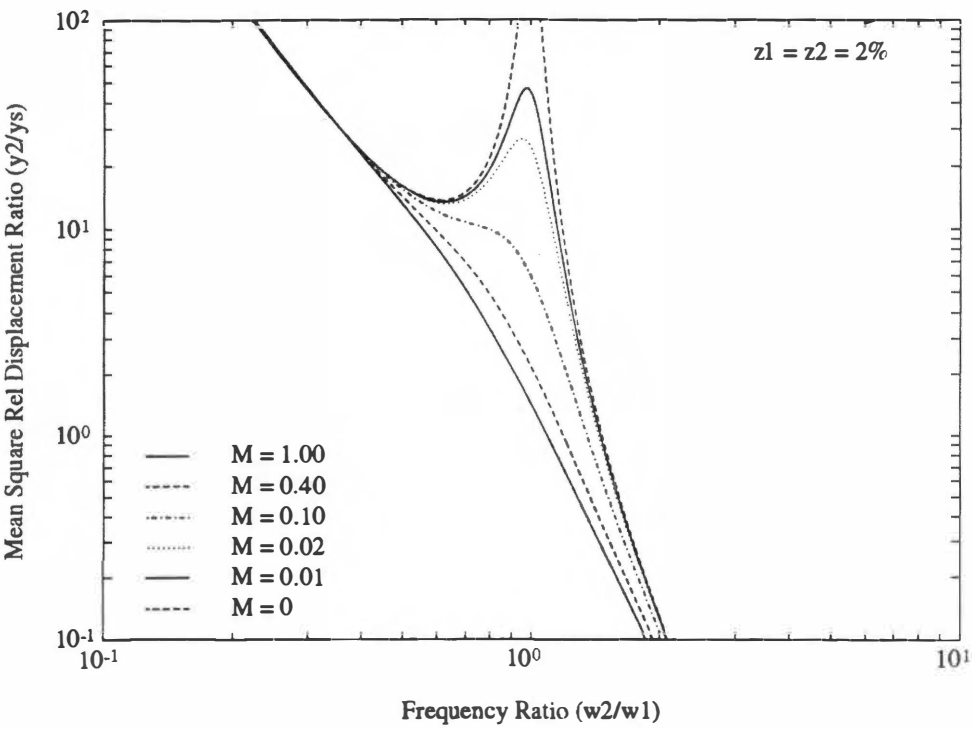

Figure 3.4 Mean square relative disp. of m_2 as a function of ω_2/ω_1 and M for $\zeta_1 = \zeta_2 = 2\%$

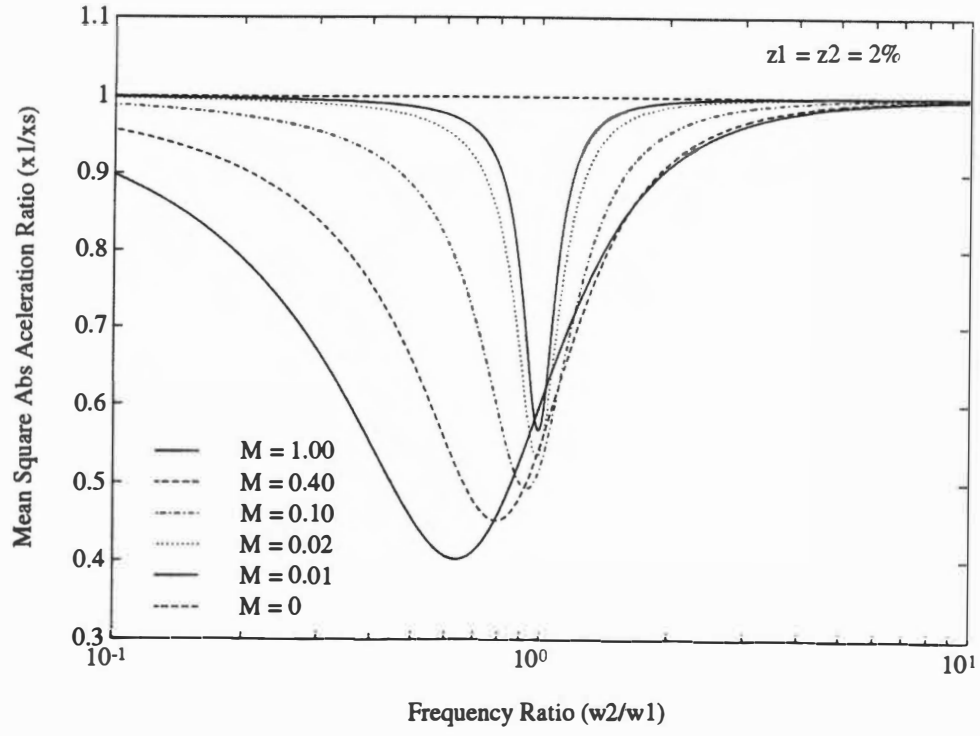

Figure 3.5 Mean square acceleration of m_1 as a function of ω_2/ω_1 and M for $\zeta_1 = \zeta_2 = 2\%$

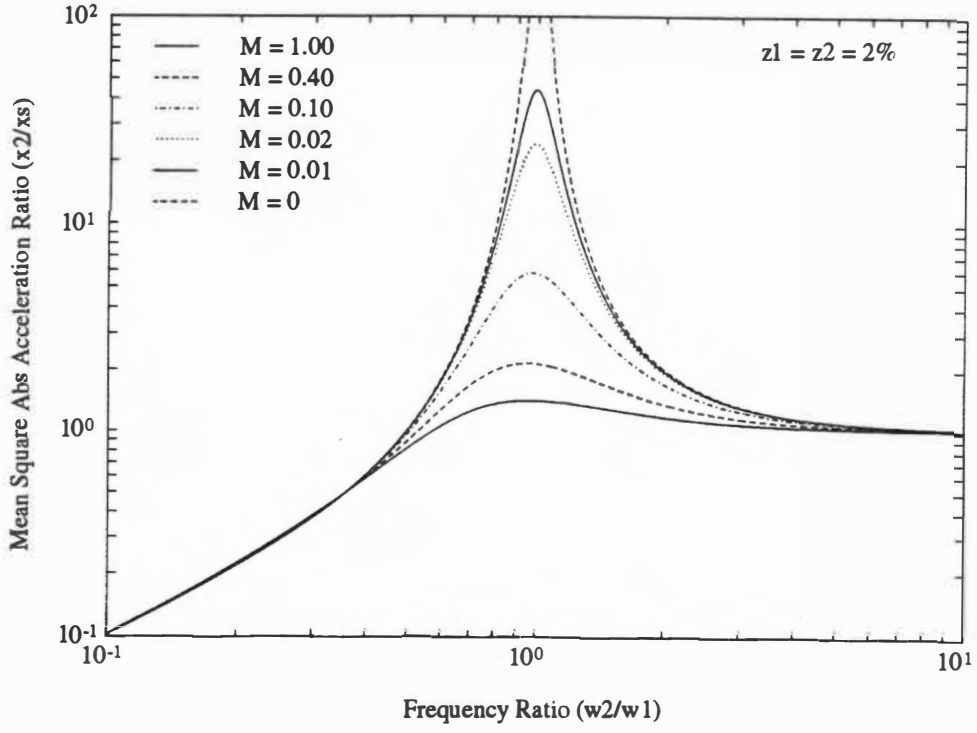

Figure 3.6 Mean square acceleration of m_2 as a function of ω_2/ω_1 and M for $\zeta_1 = \zeta_2 = 2\%$

envelopes a significant portion of real structural systems), there is evidence of the dynamic vibration absorber effect. The mean square acceleration of m_1 is decreased while the mean square acceleration of m_2 is increased (Figs. 3.5 and 3.6). This effect has sharp tuning when m_2 is small and broad tuning when m_2 is large. In other words, significant dynamic loading of the lower mass by the upper mass occurs over a wider range of frequency ratio values as the mass ratio increases.

Plot set 2 (Figs. 3.7 and 3.8) accentuates the sensitivity to the mass ratio parameter for realistic uncoupled natural frequency ratios ($0.4 < \omega_2/\omega_1 < 2.0$).

(1) The mean square relative displacement of m_1 has a fourfold increase between M = 0.1 and M = 1.0, fairly independent of frequency ratio (Fig. 3.7). For small M the only frequency ratio with significance is ω_2/ω_1 = 1.0 which displays dynamic loading out to M = .0001, but between M = .01 and .15 there is substantial deviation for other values of frequency ratio such as 0.8 and 0.4.

(2) The mean square acceleration of m_1 displays significant loading as M approaches one for all the frequency ratios (Fig. 3.8). The maximum amount of loading occurs for $\omega_2/\omega_1 < 1.0$ and for $\omega_2/\omega_1 = 1.0$ loading occurs out to M = .001.

(3) The mean square acceleration of the lower mass is always less than the 1-DOF system as the upper mass loads down the lower mass, or acts like a dynamic vibration absorber (Fig 3.8).

(4) The sensitivity to M for small M just discussed is less pronounced when the uncoupled natural frequency ratio parameter ω_2/ω_1 differs considerably from unity. There is nevertheless, ample sensitivity to M over a wide range of useful frequency ratio values.

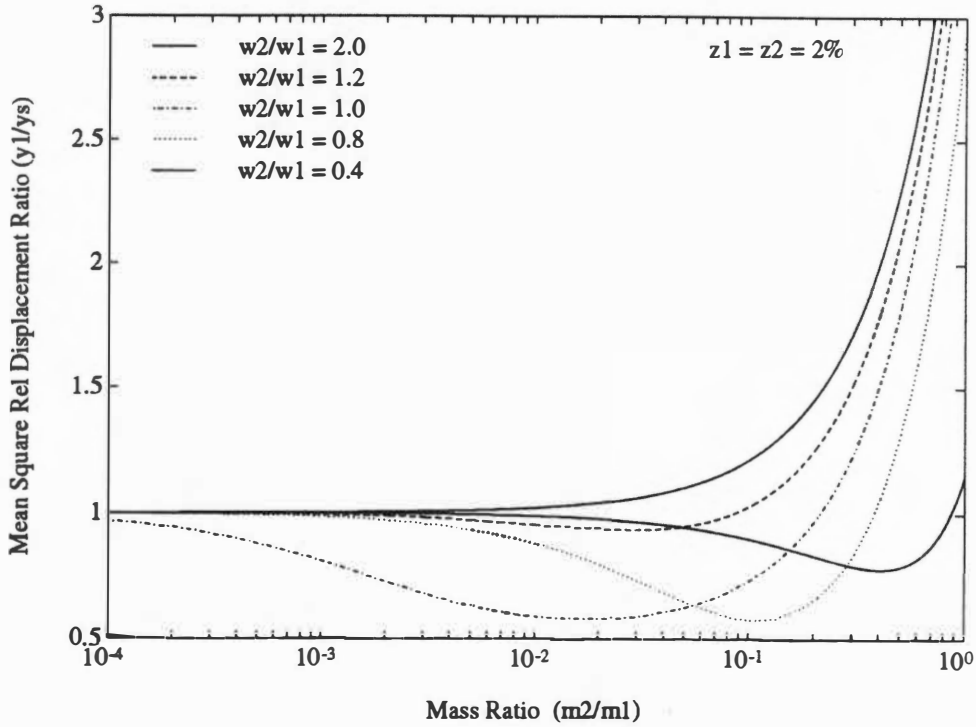

Figure 3.7 Mean square relative disp. of m_1 as a function of M and ω_2/ω_1 for $\zeta_1 = \zeta_2 = 2\%$

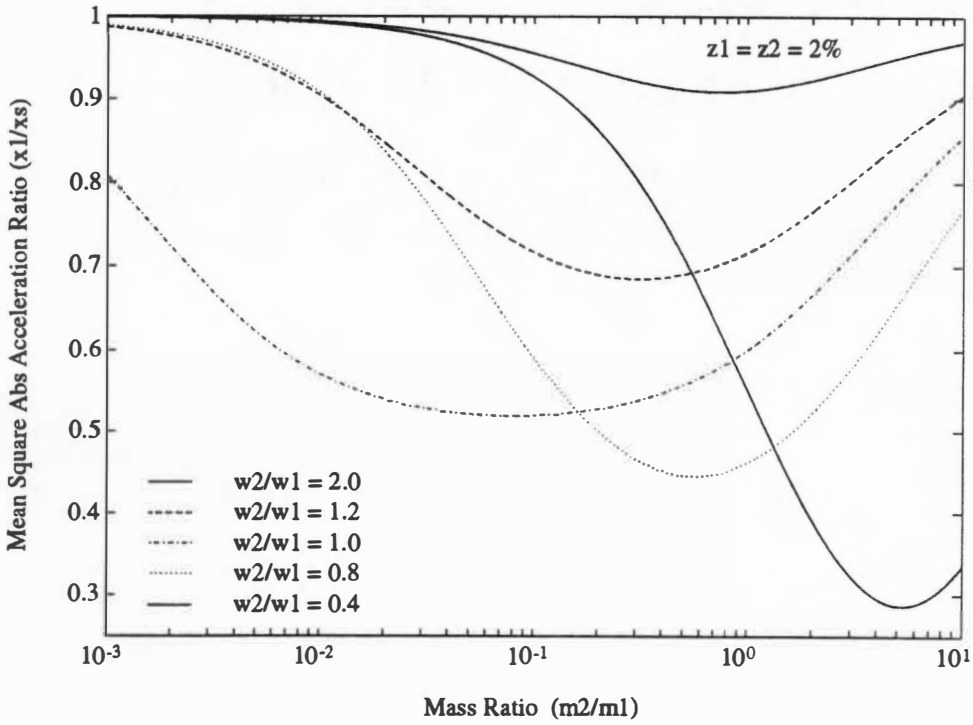

Figure 3.8 Mean square acceleration of m_1 as a function of M and ω_2/ω_1 for $\zeta_1 = \zeta_2 = 2\%$

The last plot set 3 (Figs. 3.9 through 3.14) reveals the influence system damping has on dynamic loading.

(1) For equal damping in each spring-mass-damper system ($\zeta_1 = \zeta_2$) dynamic loading is relatively independent of the damping ratio for mass ratios greater than 0.1 (Figs. 3.9 and 3.10). For mass ratios less than 0.1 an increase in equivalent damping ratio will decrease the amount of dynamic loading.

(2) For constant ζ_1 an increase in ζ_2 will increase the dynamic absorber effect on the bottom mass, or as the damping in the upper mass system increases, it is more efficient as a dynamic vibration absorber for given M and ζ_1 (Figs. 3.11 and 3.12). Also, as M approaches 1 dynamic loading is more dependent on the top damping ratio.

(3) For constant ζ_2 an increase in ζ_1 will decrease the dynamic absorber affect on the bottom mass, or as the damping in the lower mass system increases, the upper mass, for given M and ζ_2, is less efficient as a dynamic vibration absorber (Figs. 3.13, and 3.14).

This exercise thoroughly demonstrates the degree of response sensitivity, for a wide range of dimensionless parameters, that an equipment item has on its supporting structure. The conclusion can be made that very few structural systems can neglect the dynamic loading interaction between equipment and support, without risking a severe overtest at the equipment laboratory vibration test. The assumption sometimes made that the equipment dynamics are negligibly small compared to the support structure, to justify a infinite impedance test, is unfounded. In reality, the dynamic loading an equipment item exerts against its support must be considered. Now that this conclusion has been validated, the methods available to account for dynamic loading will be investigated.

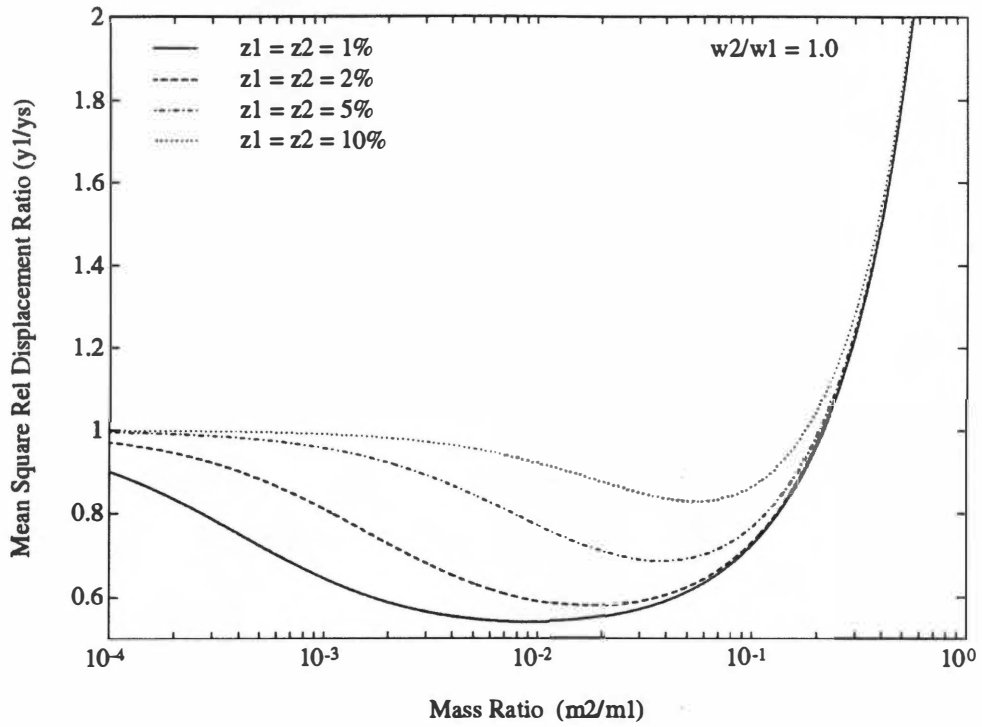

Figure 3.9 Mean square relative disp. of m_1 as a function of M and equal damping ratios for $\omega_2/\omega_1 = 1$

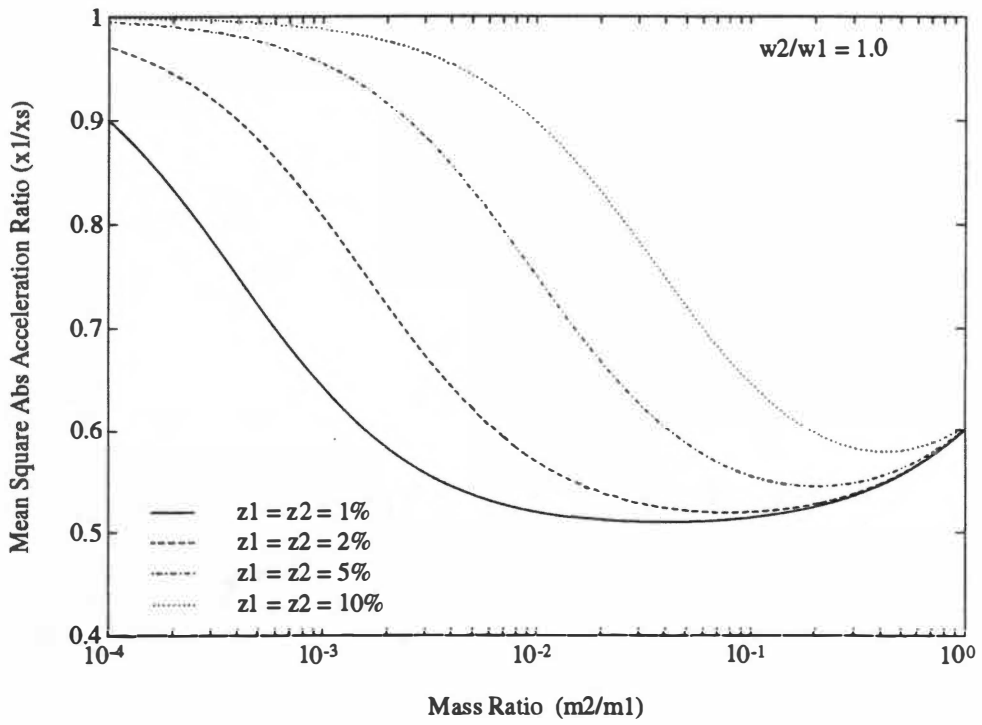

Figure 3.10 Mean square acceleration of m_1 as a function of M and equal damping ratios for $\omega_2/\omega_1 = 1$

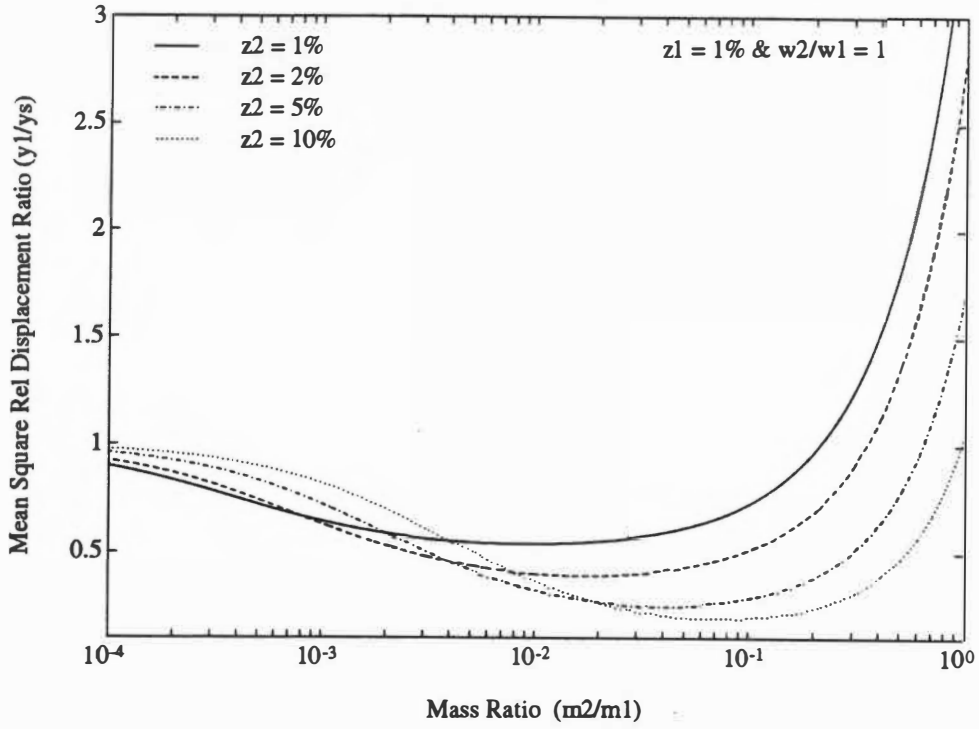

Figure 3.11 Mean square rel. disp. of m_1 as a function of M and ζ_2 for $\omega_2/\omega_1 = 1$ and $\zeta_1 = 1\%$

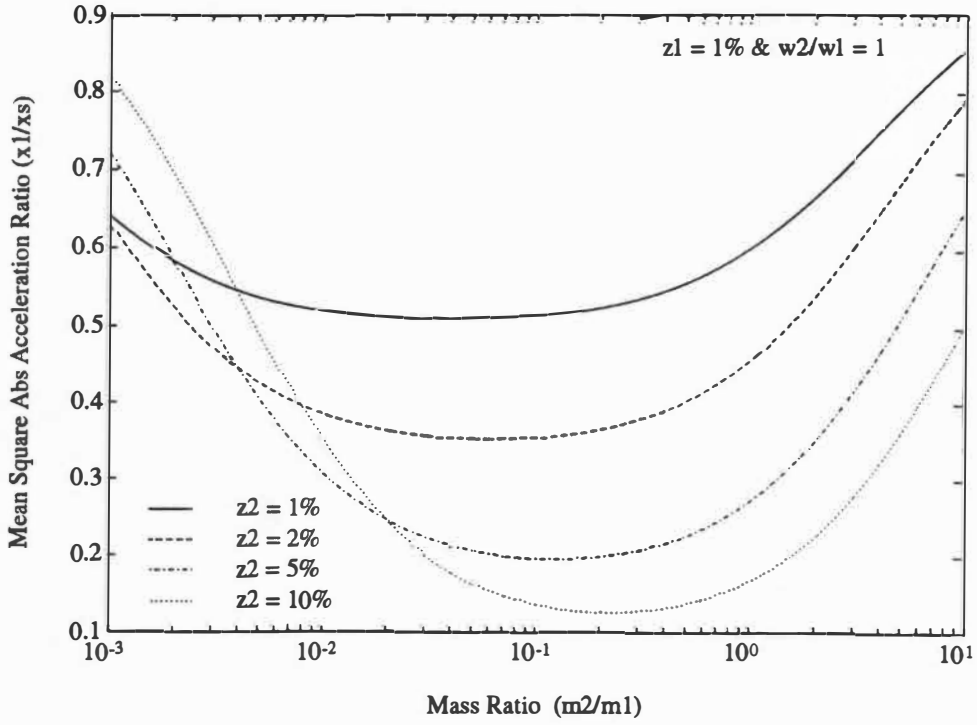

Figure 3.12 Mean square accel. of m_1 as a function of M and ζ_2 for $\omega_2/\omega_1 = 1$ and $\zeta_1 = 1\%$

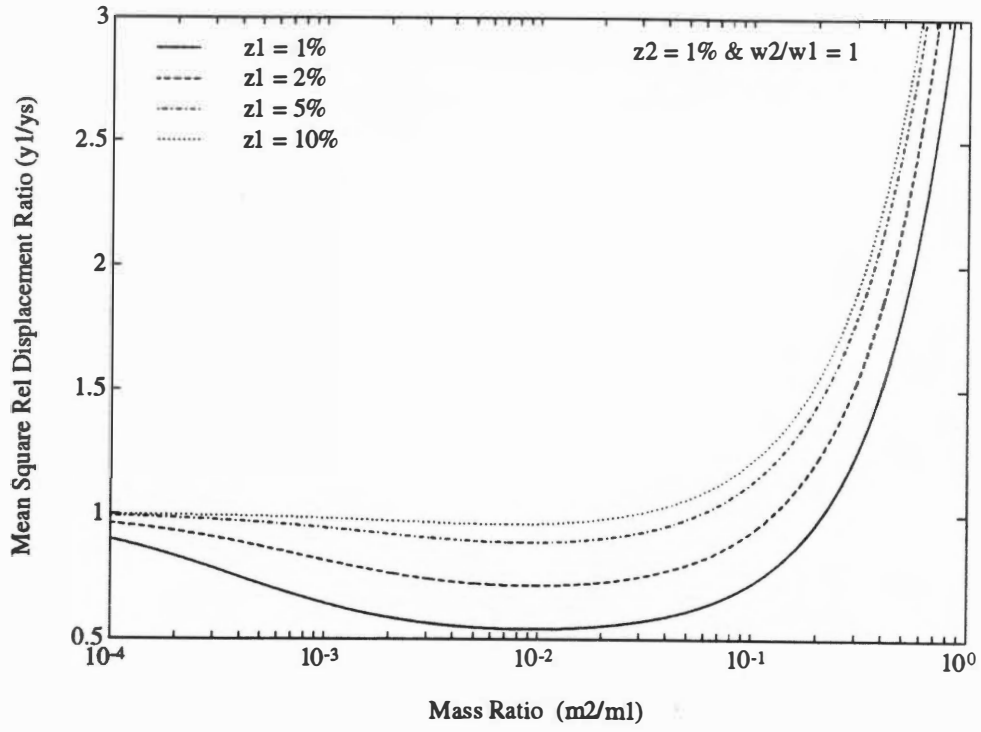

Figure 3.13 Mean square rel. disp. of m_1 as a function of M and ζ_1 for $\omega_2/\omega_1 = 1$ and $\zeta_2 = 1\%$

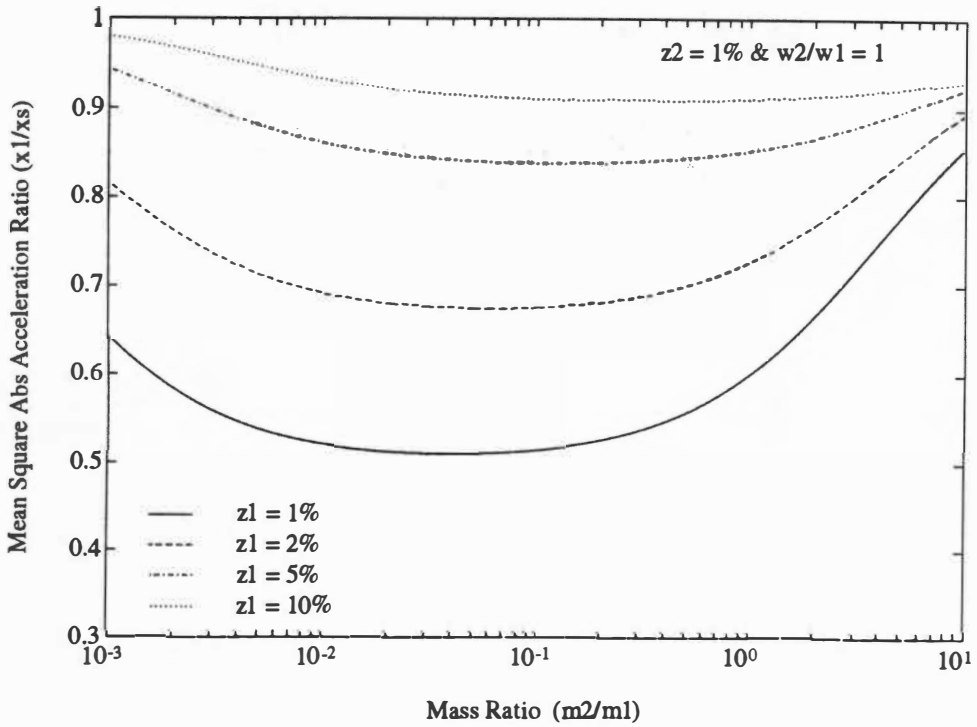

Figure 3.14 Mean square accel. of m_1 as a function of M and ζ_1 for $\omega_2/\omega_1 = 1$ and $\zeta_2 = 1\%$

CHAPTER 4

MECHANICAL IMPEDANCE AND CONNECTION OF STRUCTURES

A typical missile structure consists of several individual sections that are connected together to form the complete missile assembly. The individual missile sections perform unique functions and will be referred to as missile subsystems. Each subsystem usually consists of a number of levels or orders of structure. A level, or order, of a mechanical subsystem is that portion of a subsystem which can be identified as a single region in an overall model of the subsystem. For example, aerodynamic turbulence and rocket motor vibration excite the outermost airframe structure (first level), which drives the internal structure of the subsystem (second level), which carries an equipment mounting bracket (third level), to which is attached the case of an instrument (fourth level), which supports a module chassis (fifth level), and the module chassis is the mounting for a small component part (sixth level).

Available excitation energy originates entirely from external stimuli and not from the dynamic properties of the mechanical subsystem. Due to the limited amount of excitation energy available, the response of any level of structure within any subsystem is a function of structure response of both higher and lower orders for every subsystem. That is, when one level of structure exhibits an antiresonance, the next lower level will experience small responses. When the structure of higher order exhibits a resonance, the lower level structure will not be as constrained and will experience larger responses. Each added subsystem influences all other subsystems and all levels of structure within each subsystem. To explore this concept an introduction to mechanical impedance methods is

presented and is then extended to evaluate subsystem interface dynamic relationships.

Mechanical Impedance of Spring-Mass-Damper System

As previously stated, it is a property of linear, time invariant mechanical systems that when the excitation is steady state harmonic input then the response is also steady state harmonic motion at the same frequency. All that are required to describe completely the relationship between harmonic force and harmonic response are two parameters, the ratio of the magnitudes of the two harmonically varying quantities, and the phase angle between them. Thus, the dynamic properties of any particular structure may be fully described by these two parameters, both of which vary with the frequency of the harmonic excitation. The information conveyed by these parameters is generally referred to as mechanical impedance data. (It should be noted that the formal definition of mechanical impedance is the complex ratio of driving force over resulting velocity. The term mechanical impedance, as used in this thesis, simply implies variables that contain ratios of motion and force.)

The manner in which impedance data are derived may be conveniently illustrated using the standard single-degree-of-freedom (1-DOF) system shown in Fig. 4.1. A single coordinate $x(t)$ is required to describe its motion and a force $f(t)$ is considered to be applied to the mass. The general equation of motion for this system is

$$m\ddot{x}(t) + c\dot{x}(t) + kx(t) = f(t) \tag{4.1}$$

Now, suppose that the applied force is harmonic with a magnitude $|F|$ and a frequency ω and has a phase angle θ_F relative to some reference signal. Then by using phasor notation both quantities can be described by a single parameter.

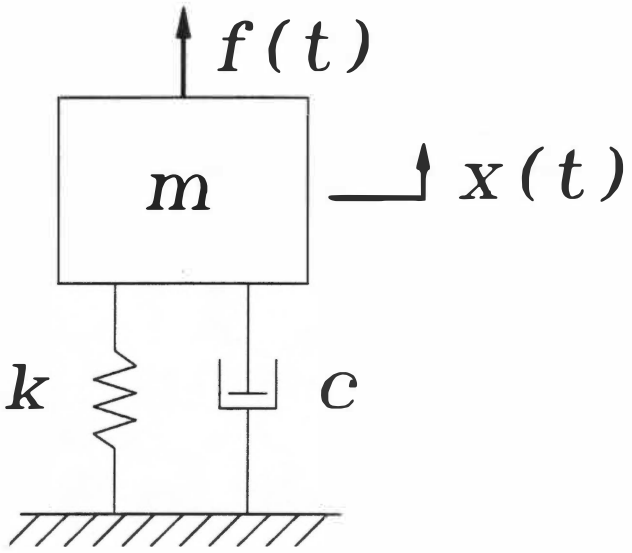

Figure 4.1 Single-degree-of-freedom system with applied force.

$$f(t) = F(\omega)e^{i\omega t} = (|F|e^{i\theta_F})e^{i\omega t} = |F|e^{i(\omega t + \theta_F)} \tag{4.2}$$

Now, assume that the system responds with harmonic displacement at the same frequency ω but with a magnitude $|X|$ and a phase angle θ_X (relative to the same reference signal). We may express this as

$$x(t) = X(\omega)e^{i\omega t} = (|X|e^{i\theta_X})e^{i\omega t} = |X|e^{i(\omega t + \theta_X)} \tag{4.3}$$

Substituting Eqs. (4.2) and (4.3) into Eq. (4.1) we have

$$(-\omega^2 m + i\omega c + k)X(\omega)e^{i\omega t} = F(\omega)e^{i\omega t} \tag{4.3}$$

dividing through by $e^{i\omega t}$ and solving for the ratio X/F yields

$$\frac{X(\omega)}{F(\omega)} = \hat{C}(\omega) = \frac{1}{-\omega^2 m + i\omega c + k} \tag{4.4}$$

The complex quantity $\hat{C}(\omega)$ fully defines the relationship between the harmonic displacement response and the harmonic force in the frequency domain (the caret ^ symbol will be used to distinguish impedance variables). The function $\hat{C}(\omega)$ is called compliance but has also been referred to in the literature as receptance or dynamic flexibility [15-17]. Both the magnitude ratio and the phase angle between the two quantities are contained within this complex quantity

$$\hat{C}(\omega) = \frac{X(\omega)}{F(\omega)} = \left(\frac{|X|}{|F|}\right)\frac{e^{i\theta_X}}{e^{i\theta_F}} = \left(\frac{|X|}{|F|}\right)e^{i(\theta_X - \theta_F)} = |\hat{C}|e^{i\theta_C} \tag{4.5}$$

with $|\hat{C}|$ the magnitude ratio of displacement/force and θ_C the phase angle between displacement and force.

Compliance, $\hat{C}(\omega)$, the ratio of displacement response to excitation force, is widely used in analytical work since equations of motion are usually formulated and solved in

terms of displacement. However, we could equally well express the response properties discussed above in terms of a velocity/force ratio (mobility, $\hat{Y}$) or an acceleration/force ratio (accelerance, $\hat{A}$) and, indeed, the acceleration/force ratio form will be adopted herein for the reason that acceleration, not displacement, is the most commonly measured motion parameter in both field and laboratory settings. Accelerance $\hat{A}(\omega)$ is related to compliance $\hat{C}(\omega)$ by an $(i\omega)^2$ factor:

$$\hat{A}(\omega) = (i\omega)^2 \hat{C}(\omega) \tag{4.6}$$

The reciprocals of these three variables, namely force/displacement ratio (dynamic stiffness, $\hat{K}$), force/velocity ratio (mechanical impedance, $\hat{Z}$), and force/acceleration ratio (effective mass, $\hat{E}$) are also equally valid response properties and are frequently encountered in the literature. Again, all six variables are referred to here as impedance variables.

Impedance of Multi-Degree-of-Freedom System

The response relationships described above are valid for multiple-degree-of-freedom lumped parameter systems and in fact, are applicable for infinite-degree-of-freedom continuous systems as well. The relationships between acceleration and force are best understood if they are written in matrix form for a general linear, elastic body under arbitrary excitation (see Fig. 4.2). It is assumed that the force $f_i(t)$ and acceleration $a_i(t)$ are in the same direction acting at the same point.

$$\begin{Bmatrix} a_1(t) \\ a_2(t) \\ a_3(t) \end{Bmatrix} = \begin{bmatrix} \hat{A}_{11} & \hat{A}_{12} & \hat{A}_{13} \\ \hat{A}_{21} & \hat{A}_{22} & \hat{A}_{23} \\ \hat{A}_{31} & \hat{A}_{32} & \hat{A}_{33} \end{bmatrix} \begin{Bmatrix} f_1(t) \\ f_2(t) \\ f_3(t) \end{Bmatrix} \tag{4.7}$$

To determine one column of the accelerance matrix (say column 2) it is necessary to apply

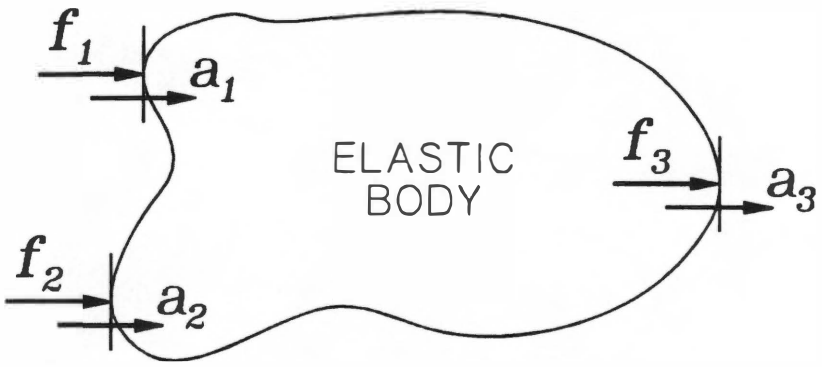

Figure 4.2 General linear elastic body subjected to arbitrary loading.

a force $f_2 = 1e^{i\omega t}$ and set $f_1 = f_3 = 0$

$$\begin{Bmatrix} a_1 \\ a_2 \\ a_3 \end{Bmatrix} = [\hat{A}] \begin{Bmatrix} 0 \\ 1e^{i\omega t} \\ 0 \end{Bmatrix} = \begin{Bmatrix} \hat{A}_{12} e^{i\omega t} \\ \hat{A}_{22} e^{i\omega t} \\ \hat{A}_{32} e^{i\omega t} \end{Bmatrix} \tag{4.8}$$

and the resulting accelerations, considering both magnitude and phase, are the desired accelerances. If the accelerance subscript $i = j$ and the force and acceleration are in the same direction at that point then the accelerance $\hat{A}_{ij}$ is called driving point accelerance. Otherwise $\hat{A}_{ij}$ $(i \neq j)$ is called transfer accelerance.

Impedance of Connected Subsystems

Consider a missile system consisting of three subsystems, joined at common connection points, as shown in Fig 4.3. The response of the combined system can be predicted using mechanical impedance methods [18]. Each subsystem contains several levels of structure. Subscripts denote missile station location and superscripts denote subsystem designator. The matrix equation for the separate subsystems before coupling is:

$$\begin{Bmatrix} a_1^I \\ a_2^I \\ a_2^{II} \\ a_3^{II} \\ a_3^{III} \\ a_4^{III} \end{Bmatrix} = \begin{bmatrix} \hat{A}_{11}^I & \hat{A}_{12}^I & 0 & 0 & 0 & 0 \\ \hat{A}_{21}^I & \hat{A}_{22}^I & 0 & 0 & 0 & 0 \\ 0 & 0 & \hat{A}_{22}^{II} & \hat{A}_{23}^{II} & 0 & 0 \\ 0 & 0 & \hat{A}_{32}^{II} & \hat{A}_{33}^{II} & 0 & 0 \\ 0 & 0 & 0 & 0 & \hat{A}_{33}^{III} & \hat{A}_{34}^{III} \\ 0 & 0 & 0 & 0 & \hat{A}_{43}^{III} & \hat{A}_{44}^{III} \end{bmatrix} \begin{Bmatrix} F_1^I \\ F_2^I \\ F_2^{II} \\ F_3^{II} \\ F_3^{III} \\ F_4^{III} \end{Bmatrix} \tag{4.9}$$

In general the individual matrix elements will also be matrices.

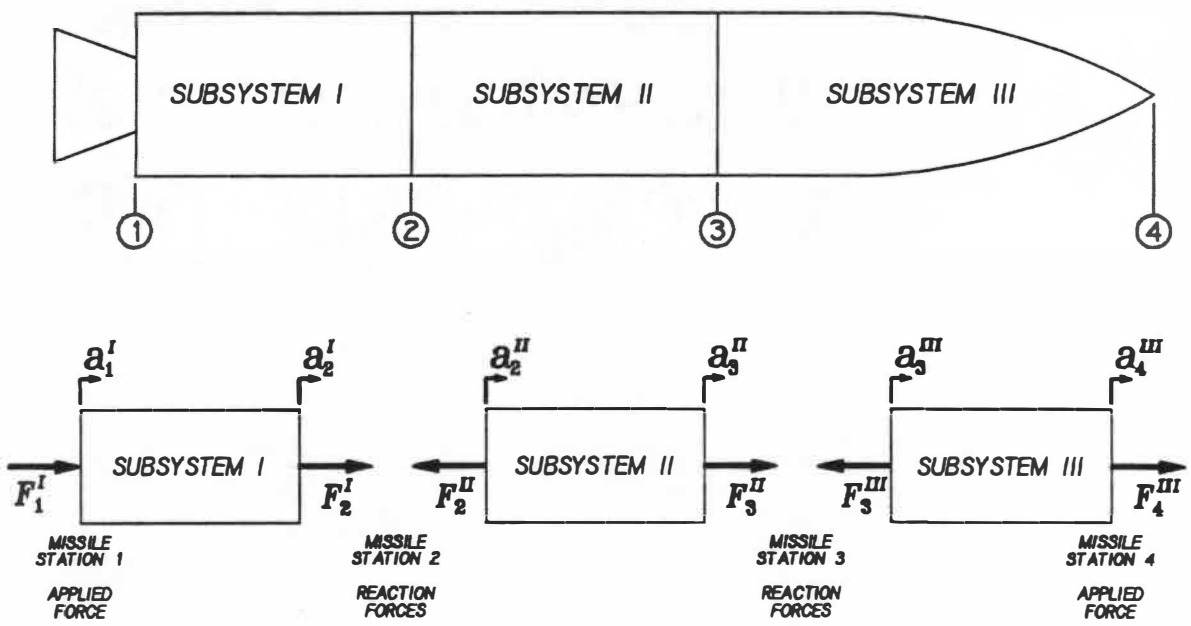

Figure 4.3 Connection of three subsystems to form a combined missile structure assembly.

To connect the three subsystems, the boundary conditions are taken as:

$$\begin{aligned} a_2^I &= a_2^{II} & a_3^{II} &= a_3^{III} \\ F_2^I &= -F_2^{II} & F_3^{II} &= -F_3^{III} \end{aligned} \tag{4.10}$$

That is, at the connection points the accelerations are equal and the sum of the internal reaction forces are equal to zero. If the accelerances of the subsystems are known and the applied input forces are specified then Eq. (4.9) may be solved first for the unknown connection forces by equating the accelerations at the connection points. Using rows 2 through 5 of Eq. (4.9) and solving simultaneously for the connection forces yields

$$F_2^I = -F_2^{II} = \frac{(\hat{A}_{23}^{II}\hat{A}_{34}^{III})F_4^{III} - (\hat{A}_{21}^{I}\hat{A}_{33}^{II} + \hat{A}_{21}^{I}\hat{A}_{33}^{III})F_1^I}{\hat{A}_{22}^{I}\hat{A}_{33}^{II} + \hat{A}_{22}^{I}\hat{A}_{33}^{III} + \hat{A}_{22}^{II}\hat{A}_{33}^{II} + \hat{A}_{22}^{II}\hat{A}_{33}^{III} - \hat{A}_{23}^{II}\hat{A}_{32}^{II}} \tag{4.11}$$

for the interface force at connection point 2 and

$$F_3^{II} = -F_3^{III} = \frac{(\hat{A}_{22}^{I}\hat{A}_{34}^{III} + \hat{A}_{22}^{II}\hat{A}_{34}^{III})F_4^{III} - (\hat{A}_{21}^{I}\hat{A}_{32}^{II})F_1^I}{\hat{A}_{22}^{I}\hat{A}_{33}^{II} + \hat{A}_{22}^{I}\hat{A}_{33}^{III} + \hat{A}_{22}^{II}\hat{A}_{33}^{II} + \hat{A}_{22}^{II}\hat{A}_{33}^{III} - \hat{A}_{23}^{II}\hat{A}_{32}^{II}} \tag{4.12}$$

for the interface force at connection point 3. All the forces are now known and the resulting accelerations may be determined directly from Eq (4.9).

$$a_1^I = \hat{A}_{11}^{I}F_1^I + \hat{A}_{12}^{I}\left(\frac{(\hat{A}_{23}^{II}\hat{A}_{34}^{III})F_4^{III} - (\hat{A}_{21}^{I}\hat{A}_{33}^{II} + \hat{A}_{21}^{I}\hat{A}_{33}^{III})F_1^I}{\hat{A}_{22}^{I}\hat{A}_{33}^{II} + \hat{A}_{22}^{I}\hat{A}_{33}^{III} + \hat{A}_{22}^{II}\hat{A}_{33}^{II} + \hat{A}_{22}^{II}\hat{A}_{33}^{III} - \hat{A}_{23}^{II}\hat{A}_{32}^{II}}\right) \tag{4.13}$$

$$a_2^I = a_2^{II} = \hat{A}_{21}^{I}F_1^I + \hat{A}_{22}^{I}\left(\frac{(\hat{A}_{23}^{II}\hat{A}_{34}^{III})F_4^{III} - (\hat{A}_{21}^{I}\hat{A}_{33}^{II} + \hat{A}_{21}^{I}\hat{A}_{33}^{III})F_1^I}{\hat{A}_{22}^{I}\hat{A}_{33}^{II} + \hat{A}_{22}^{I}\hat{A}_{33}^{III} + \hat{A}_{22}^{II}\hat{A}_{33}^{II} + \hat{A}_{22}^{II}\hat{A}_{33}^{III} - \hat{A}_{23}^{II}\hat{A}_{32}^{II}}\right) \tag{4.14}$$

$$a_3^{II} = a_3^{III} = \hat{A}_{34}^{III}F_4^{III} - \hat{A}_{33}^{III}\left(\frac{(\hat{A}_{22}^{I}\hat{A}_{34}^{III} + \hat{A}_{22}^{II}\hat{A}_{34}^{III})F_4^{III} - (\hat{A}_{21}^{I}\hat{A}_{32}^{II})F_1^I}{\hat{A}_{22}^{I}\hat{A}_{33}^{II} + \hat{A}_{22}^{I}\hat{A}_{33}^{III} + \hat{A}_{22}^{II}\hat{A}_{33}^{II} + \hat{A}_{22}^{II}\hat{A}_{33}^{III} - \hat{A}_{23}^{II}\hat{A}_{32}^{II}}\right) \tag{4.15}$$

$$a_4^{III} = \hat{A}_{44}^{III} F_4^{III} - \hat{A}_{43}^{III} \left(\frac{(\hat{A}_{22}^{I}\hat{A}_{34}^{III} + \hat{A}_{22}^{II}\hat{A}_{34}^{III}) F_4^{III} - (\hat{A}_{21}^{I}\hat{A}_{32}^{II}) F_1^{I}}{\hat{A}_{22}^{I}\hat{A}_{33}^{II} + \hat{A}_{22}^{I}\hat{A}_{33}^{III} + \hat{A}_{22}^{II}\hat{A}_{33}^{II} + \hat{A}_{22}^{II}\hat{A}_{33}^{III} - \hat{A}_{23}^{II}\hat{A}_{32}^{II}} \right) \tag{4.16}$$

The interface forces and accelerations are entirely determined without knowledge of the dynamic properties of each level of structure within each subsystem. This is the advantage of using mechanical impedance methods. Essentially, all that is necessary to fully describe the interface dynamics is to obtain the driving point and transfer accelerance functions for each subsystem at each station location, then combine them as indicated in Eqs. (4.11) through (4.16). The interface force and accelerations at each connection point are functions of accelerance variables from all three subsystems. In other words, the dynamics of the interfaces contain contributions from each subsystem. Accelerance functions for very complicated subsystems may be obtained via experimental laboratory impedance measurements or through the use of finite element analysis (FEA).

Application - Impedance Method for MDOF System

To verify this technique a ten-degree-of-freedom (10-DOF) dynamic chain analog model is broken into three subsystems then combined using Eqs. (4.11) through (4.16). Fig 4.4 details the 10-DOF system parameters and the three subsystem configurations. Driving point and transfer accelerances are determined for each subsystem at each station location. Figs. 4.5 through 4.10 present the resulting accelerance functions and Figs. 4.11 and 4.12 display the resulting connection interface force and acceleration functions using impedance method. Verification is achieved by directly solving the 10-DOF system and comparing results to those obtained with impedance method. Plots shown in Figs. 4.13 and 4.14 present impedance method results against those obtained directly from 10-DOF

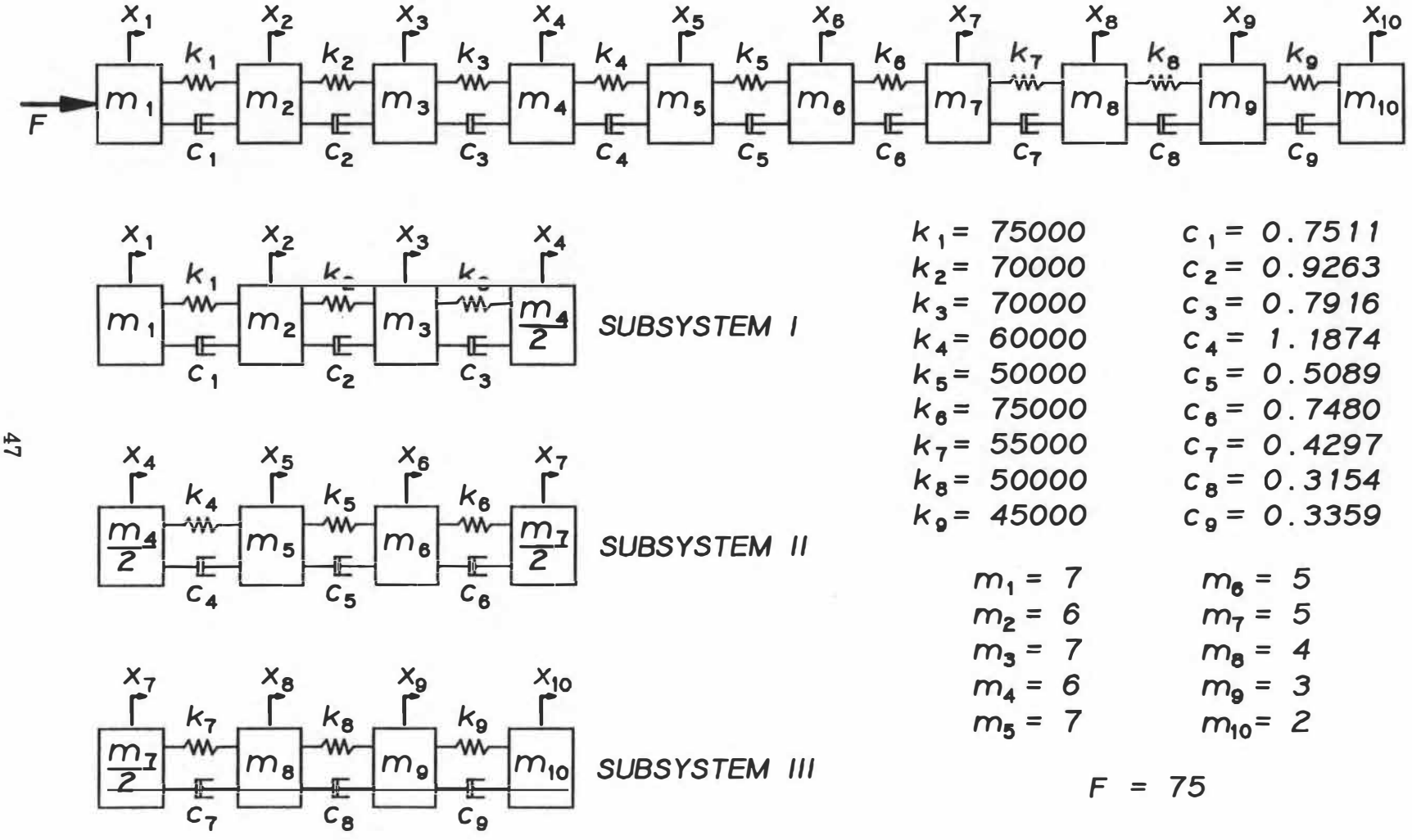

Figure 4.4 Ten-degree-of-freedom, free-free, dynamic chain analog system and the three subsystems.

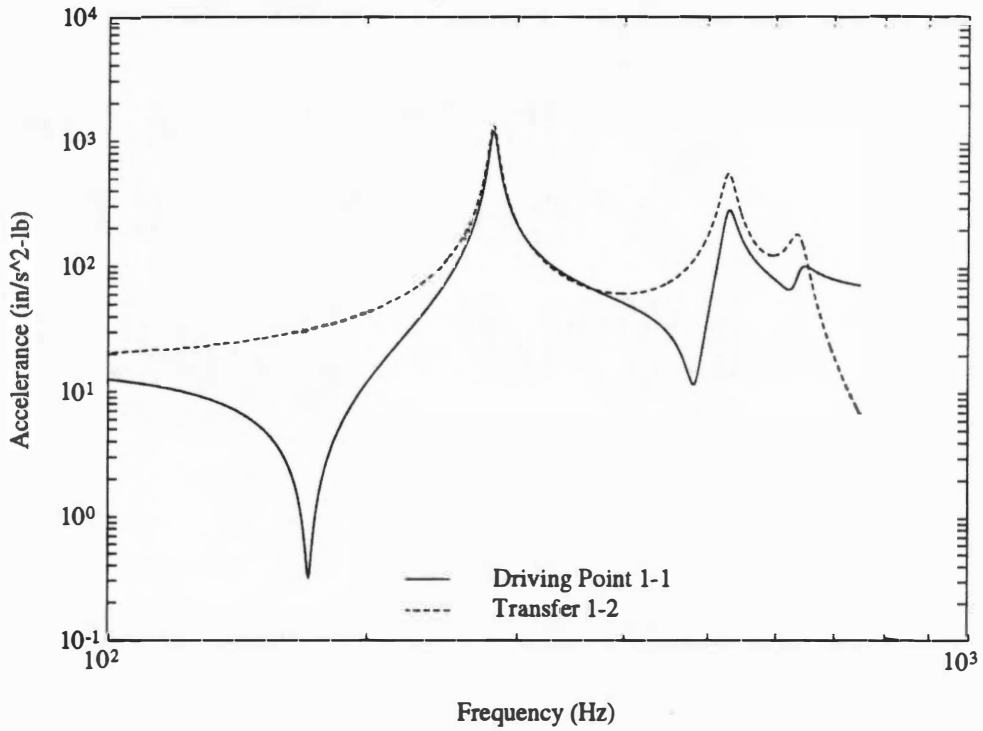

Figure 4.5 Driving point and transfer accelerance FRF of subsystem *I* at missile station 1.

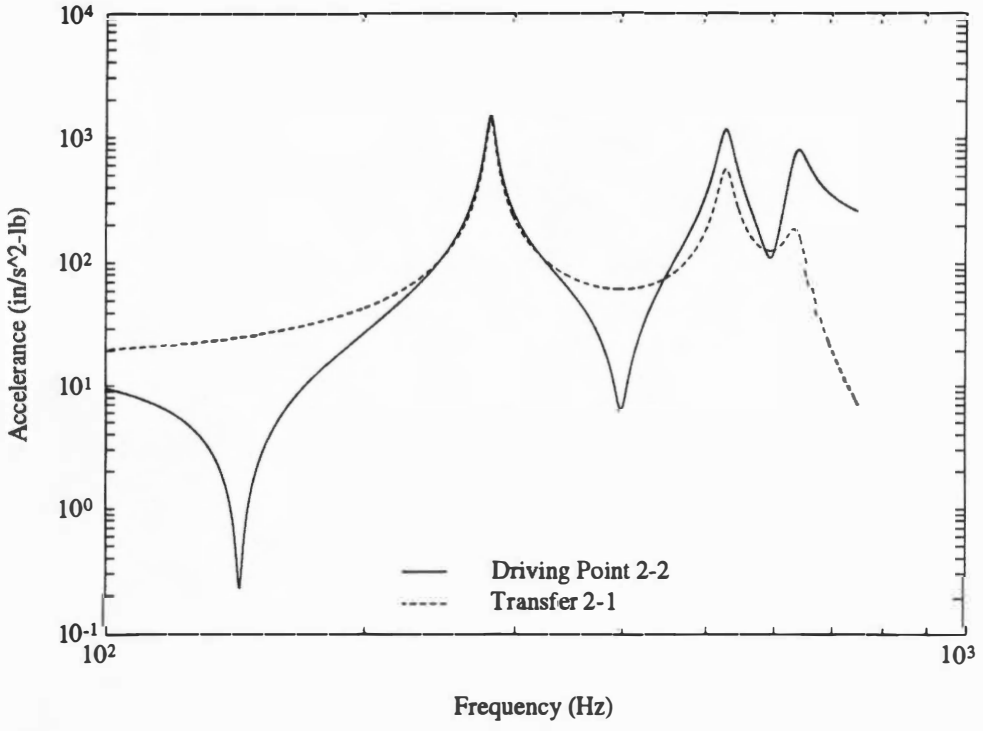

Figure 4.6 Driving point and transfer accelerance FRF of subsystem *I* at missile station 2.

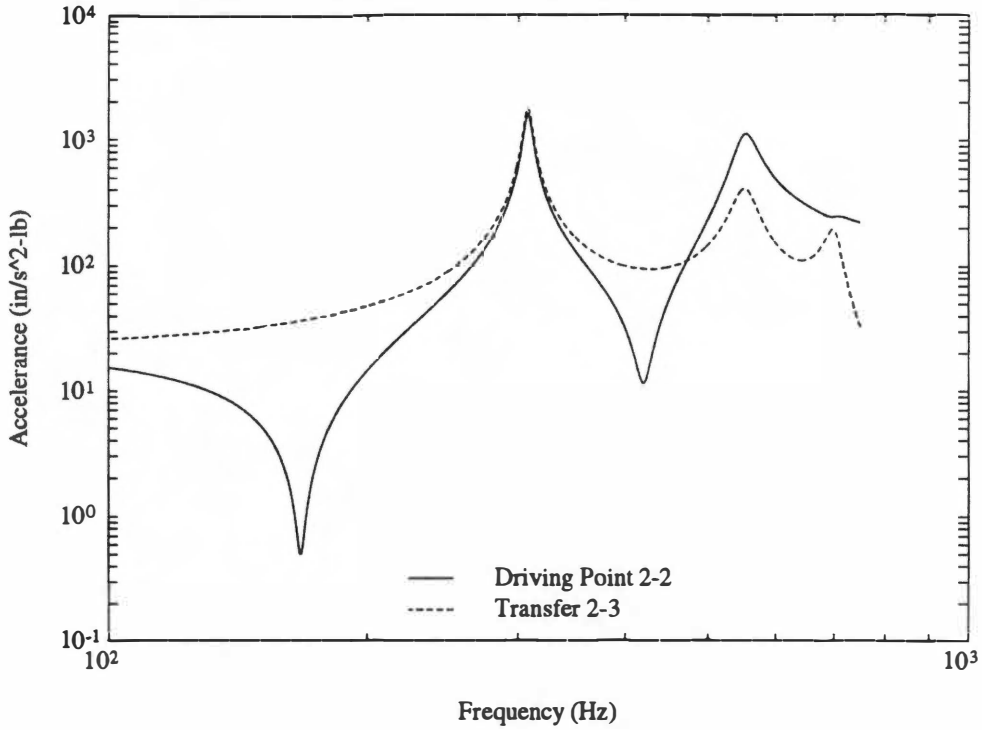

Figure 4.7 Driving point and transfer accelerance FRF of subsystem *II* at missile station 2.

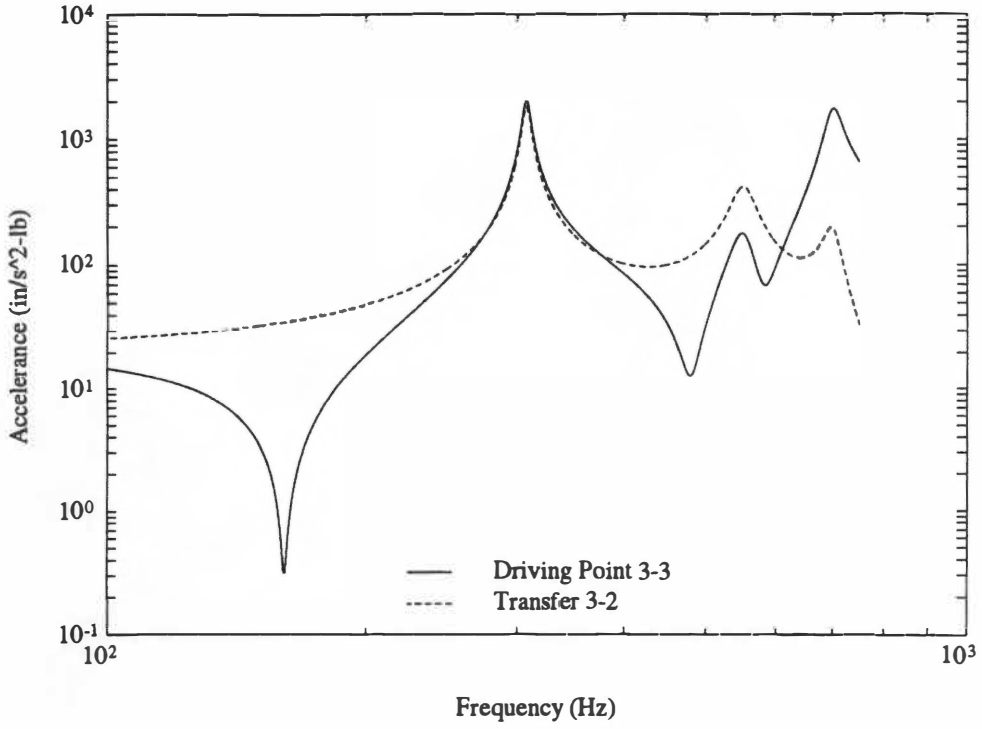

Figure 4.8 Driving point and transfer accelerance FRF of subsystem *II* at missile station 3.

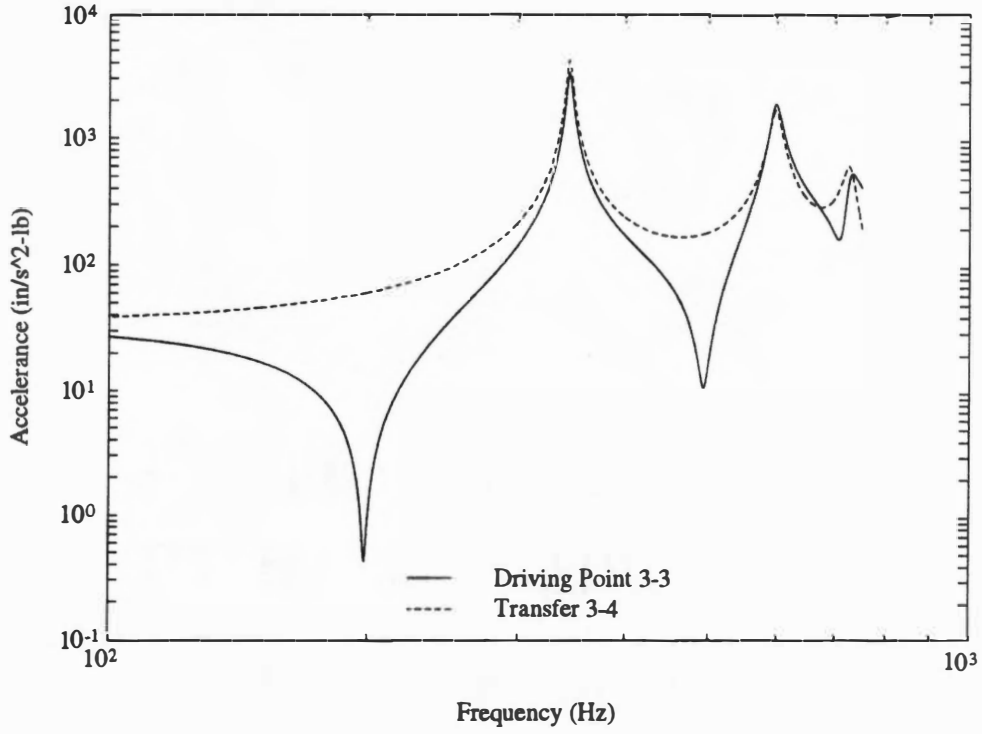

Figure 4.9 **Driving point and transfer accelerance FRF of subsystem *III* at missile station 3.**

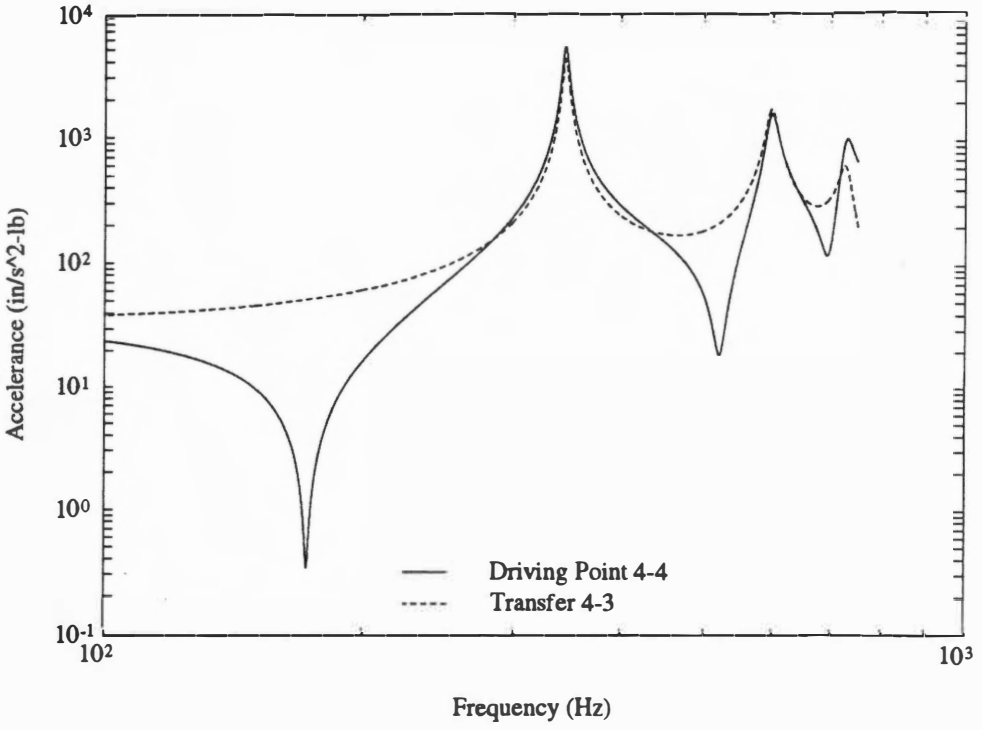

Figure 4.10 **Driving point and transfer accelerance FRF of subsystem *III* at missile station 4.**

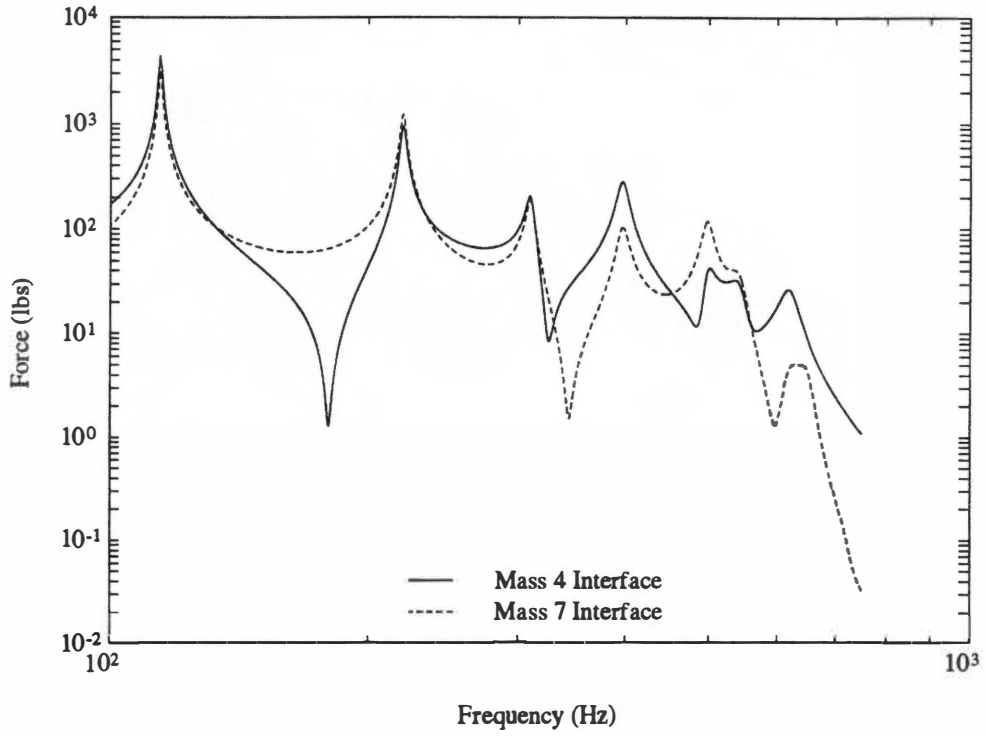

Figure 4.11 Interface force FRF at missile stations 2 and 3 resulting from impedance calculation method Eqs. (4.11) and (4.12).

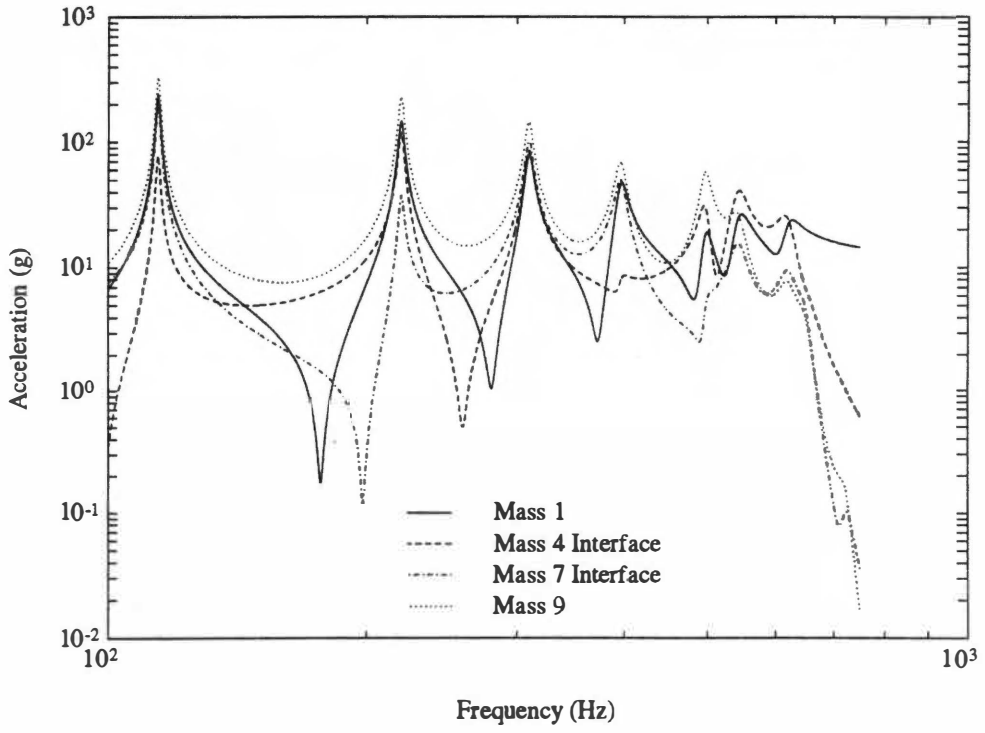

Figure 4.12 Acceleration FRF of m_1, m_4, m_7, and m_9 resulting from impedance method Eqs. (4.13) through (4.16).

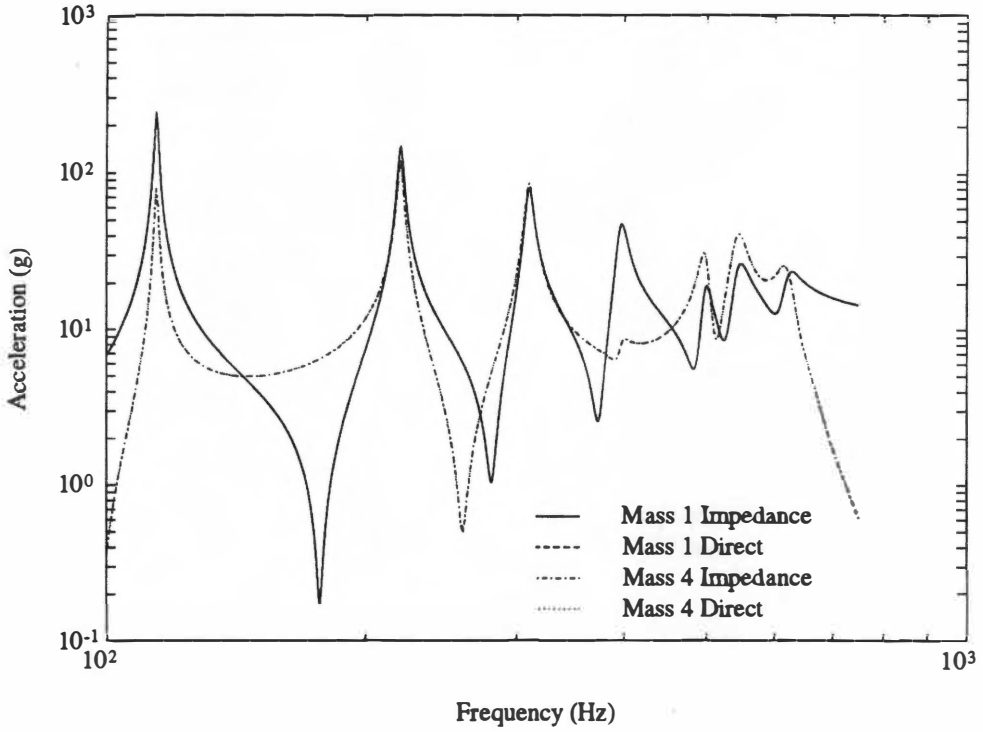

Figure 4.13 Acceleration FRF of m_1, and m_4, impedance calculation method versus direct solution.

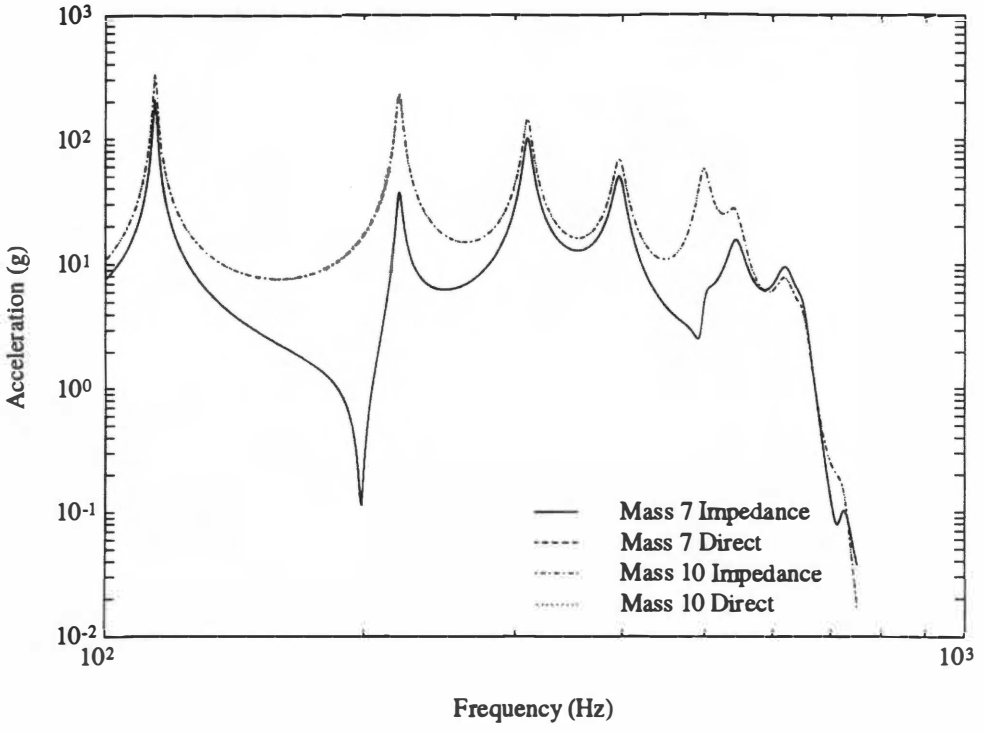

Figure 4.14 Acceleration FRF of m_7 and m_9, impedance calculation method versus direct solution.

system. As can be observed, the two results are identical (plots are coincident).

Impedance of Simplified System

The study of a simplified combined system, one in which only two subsystems are combined, offers insight into the possibility of undertesting as well as overtesting [7]. It is assumed that *subsystem I* is an active vibration source, since force vectors are applied to it, and *subsystem II* is a passive vibration load (see Fig. 4.15). The interface acceleration can be solved for in terms of effective mass $\hat{E}$ (reciprocal of accelerance) and input acceleration. Following a similar procedure as outlined above, the interface acceleration at the connection point can be shown to be

$$a_2^{\,I} = a_2^{\,II} = \left(\frac{\hat{E}_{21}^{\,I}}{\hat{E}_{22}^{\,I} + \hat{E}_{22}^{\,II}} \right) a_1^{\,I} \tag{4.17}$$

Using Norton's theorem [18] the input acceleration is related to the free acceleration of *subsystem I* when *subsystem II* is removed as

$$\left(a_2^{\,I} \right)_{fr} = -\left(\frac{\hat{E}_{23}^{\,II}}{\hat{E}_{22}^{\,I}} \right) a_1^{\,I} \tag{4.18}$$

Then by substituting Eq. (4.18) into Eq. (4.17) the interface acceleration of the combined system, in terms of effective mass and free acceleration, can be shown to be

$$a_2^{\,I} = a_2^{\,II} = \frac{\left(a_2^{\,I} \right)_{fr}}{\left(\frac{\hat{E}_{22}^{\,II}}{\hat{E}_{22}^{\,I}} + 1 \right)} \tag{4.19}$$

Examination of Eq (4.19) yields considerable information. When *subsystem I* is a

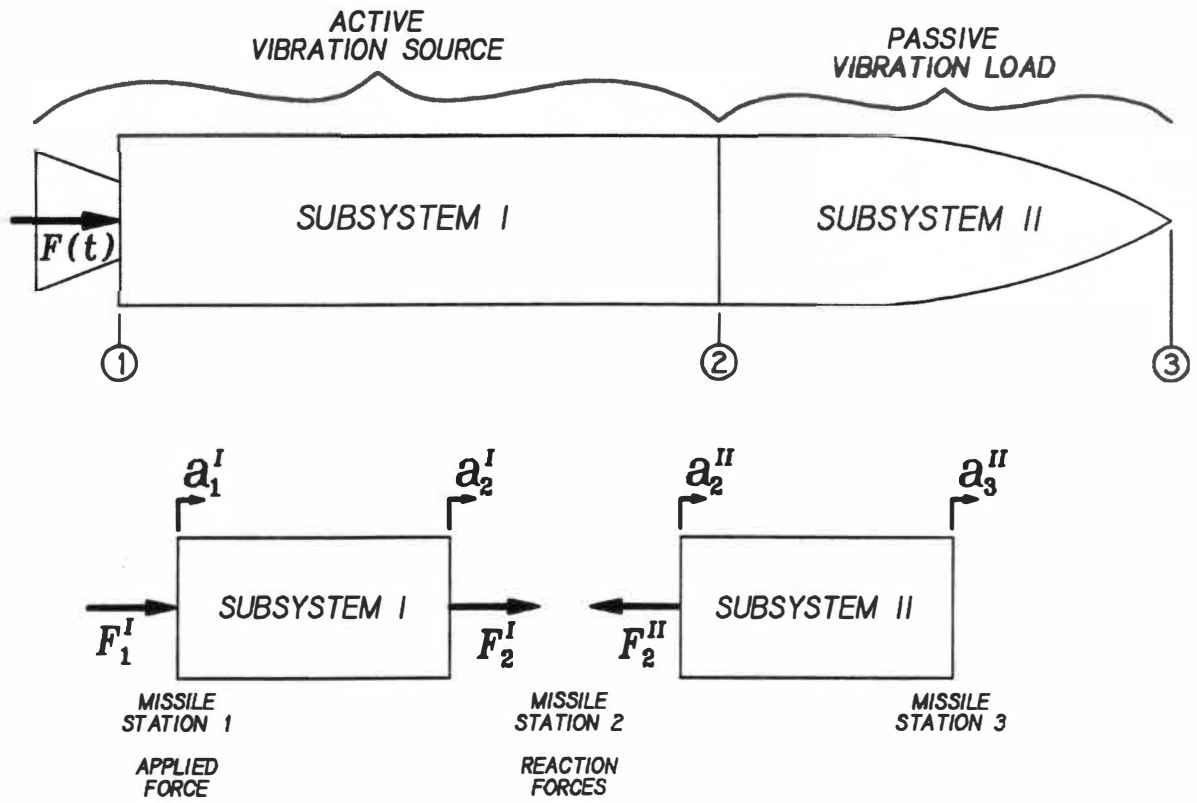

Figure 4.15 Combined system with an active vibration source (*subsystem I*) and passive vibration load (*subsystem II*).

vibration shaker ready to perform an infinite impedance vibration test, the effective mass of the structural support approaches infinity.

$$|\hat{E}_{22}^{I}| \rightarrow \infty \tag{4.20}$$

This implies from Eq. (4.19) that the interface acceleration of the combined system approaches the value of the free acceleration of *subsystem I* when *subsystem II* is removed. This is the root source of the overtest error, in other words, the subsystem test is carried out under the inaccurate assumption that

$$a_1^{I} = \left(a_2^{I}\right)_{fr} \tag{4.21}$$

is always true. In Chapter 3 it was shown that the interface acceleration of the bottom system is always less than the free acceleration of the bottom system when the top system is removed, and is significantly less at the fixed base natural frequencies of the subsystem (antiresonance of combined system).

Undertesting is also a possibility. For a simple structure, the plot of driving point effective mass vs. frequency may be divided into two general regions. At high frequencies, the structure is predominantly spring-like, and the effective mass declines with increasing frequency; at low frequencies, the structure is mass-like, and the effective mass increases with frequency. Suppose that over a given frequency range the vibration source effective mass $\hat{E}_{22}^{I}$ is compliant (spring-like) and the vibration load effective mass $\hat{E}_{22}^{II}$ is inertial (mass-like) in nature, and that there is some frequency, f_c, where these two quantities resonate:

$$\frac{\hat{E}_{22}^{II}(f_c)}{\hat{E}_{22}^{I}(f_c)} = -1 \tag{4.22}$$

The result in the field is a resonant peak of f_c with the field amplitude increased many times over that implied in Eq. (4.19). Infinite impedance testing in this case leads to serious undertesting.

In the combined mechanical system, there is an interplay of forces and accelerations due to the mechanical impedance of test object and supporting structure. This interplay renders infinite impedance testing completely unrealistic, as a means of simulating the field vibration environment. A vibration simulation test, for a subsystem mounted to a vibration shaker platform, must therefore account for both interface force and acceleration. The neglect of either one quantity is to make it impossible to avoid a considerable amount of overtesting and/or undertesting. Vibration simulation methods that account for both force and acceleration are the subject of the next chapter.

CHAPTER 5

VIBRATION TESTING USING MECHANICAL IMPEDANCE METHODS

Several techniques have been suggested taking into account the dynamic interaction between the test item and its supporting structure. For example, many proposals have been made in the past to introduce force control or combinations of force and acceleration control to reduce the gross errors that occur when using only motion control (infinite impedance testing). Otts [4] proposed force only control (zero impedance testing). Morrow [2] proposed infinite impedance testing at the lowest frequencies then switching to zero impedance testing at higher frequencies. Murfin [19] proposed acceleration control with a force limit. Witte [20-22] proposed control on the product of the magnitudes of force and acceleration as a compromise between infinite impedance testing and zero impedance testing.

The recent papers by Scharton [11, 23-25] and Smallwood [26-27] propose extremal control of force and acceleration simultaneously. This is essentially an acceleration controlled test with a force limit, or force control with an acceleration limit. Sweitzer [28] proposes a mechanical impedance correction technique by dividing the input acceleration by the equipment transmissibility function.

In spite of their advantages these methods were not widely used for several reasons. First, impedance measurements of test items and supporting structures were not generally available. Second, measurements of interface forces in both the field and laboratory were difficult to achieve. Third, it was difficult to implement the methods

using the control systems available at the time. Some of these objections still hold today, but tests based on impedance measurements and calculations are much more common today and high speed digital control methods have increased the number of options for control schemes.

The most promising of the investigated methods are: (1) force-acceleration product method, (2) dual extremal control method, and (3) transmissibility correction method. Each of these methods have distinct advantages and disadvantages. Detailed derivation, including demonstration of each method follows.

Force-Acceleration Product Method

A technique has been proposed where the laboratory test levels are defined by the product of input force and input acceleration [20-22]. This technique requires no knowledge of dynamic characteristics of the vibration source or the phase relationship between input force and input acceleration. The level of the frequency dependent product of peak input force, $F_i(\omega)$, and peak input acceleration, $a_i(\omega)$, is controlled at some specified value $K(\omega)$.

$$F_i(\omega)\, a_i(\omega) = K(\omega) \tag{5.1}$$

The test item's driving point accelerance function, $\hat{A}_T(\omega)$, is defined as the complex ratio

$$\hat{A}_T(\omega) = \frac{a_i(\omega)}{F_i(\omega)} \tag{5.2}$$

Using Eqs. (5.1) and (5.2) the relationship for peak acceleration and force as functions of the test item accelerance becomes:

$$F_i(\omega) = \sqrt{\frac{K(\omega)}{\hat{A}_T(\omega)}} \qquad a_i(\omega) = \sqrt{K(\omega)\,\hat{A}_T(\omega)} \tag{5.3}$$

The peak acceleration, $a_i(\omega)$, is a function of the square root of the test item accelerance, $\hat{A}_T(\omega)$. It attains a relative maximum value whenever the accelerance exhibits a relative maximum and becomes minimum whenever the accelerance becomes minimum. However, the peak input force, $F_i(\omega)$, is inversely proportional to the square root of the test item accelerance, $\hat{A}_T(\omega)$. It exhibits a relative maximum value whenever the accelerance reaches a relative minimum and becomes minimum at maximum accelerance values.

The essential element in using the force-acceleration product method is in specifying the frequency dependent control level, $K(\omega)$. To specify $K(\omega)$, two pieces of information are needed: (1) maximum expected acceleration levels in the field environment for the combined system (at the equipment support mounting location) and (2) the dynamic characteristics of the test specimen, which includes driving point accelerance characteristics. The control level, $K(\omega)$, can then be defined by the following relationship:

$$K(\omega) = \frac{a_{FE}^2(\omega)}{\hat{A}_{TE}(\omega)} \tag{5.4}$$

where $\hat{A}_{TE}(\omega)$ is the frequency dependent envelope of maximum values of the test specimen driving point accelerance, and $a_{FE}(\omega)$ is the frequency dependent envelope of expected maximum field acceleration levels. Using Eqs. (5.3) and (5.4) the peak input force, $F_i(\omega)$, and input acceleration, $a_i(\omega)$, can be defined as:

$$F_i(\omega) = \frac{a_{FE}(\omega)}{\sqrt{\hat{A}_{TE}(\omega)\,\hat{A}_T(\omega)}} \qquad a_i(\omega) = a_{FE}(\omega)\sqrt{\frac{\hat{A}_T(\omega)}{\hat{A}_{TE}(\omega)}} \tag{5.5}$$

The input acceleration, $a_i(\omega)$, from Eq. (5.5) can now be applied using a standard infinite impedance test procedure.

To demonstrate this method the 10-DOF analog model of Chapter 4 is used (see Fig. 4.4). The procedure is to obtain field acceleration levels from the combined 10-DOF system, calculate the driving point accelerance functions for the test specimen subsystems and then apply Eq. (5.5) to arrive at the input acceleration, $a_i(\omega)$, function. Two examples are evaluated, first, *subsystem III* is used as the test specimen and then *subsystem II* is used as the test specimen (Note: all *subsystem II* results are located in Appendix A). For demonstration purposes it is assumed that the subsystems are mounted to the combined structure at distinct, single point connections. Motion is restricted to a single axis of input. For testing, the subsystem is removed from the combined structure and mounted on a shaker with fixtures. Again, it is assumed that the input to the test subsystem during the vibration test is described by a single point in one axis.

Fig. 5.1 is a plot of m_7 response acceleration for the combined 10-DOF system (this represents the simulated field environment's maximum acceleration levels). The peak amplitudes of m_7 response acceleration are enveloped and the envelope function is $a_{FE}(\omega)$. Driving point accelerance, $\hat{A}_T(\omega)$, for *subsystem III* is displayed in Fig 5.2. The peak amplitudes of $\hat{A}_T(\omega)$ are enveloped and the envelope function is $\hat{A}_{TE}(\omega)$. To apply Eq. (5.5) the square root of the ratio of driving point accelerance over enveloped accelerance is calculated. This ratio is multiplied by the field acceleration envelope, $a_{FE}(\omega)$, to arrive at

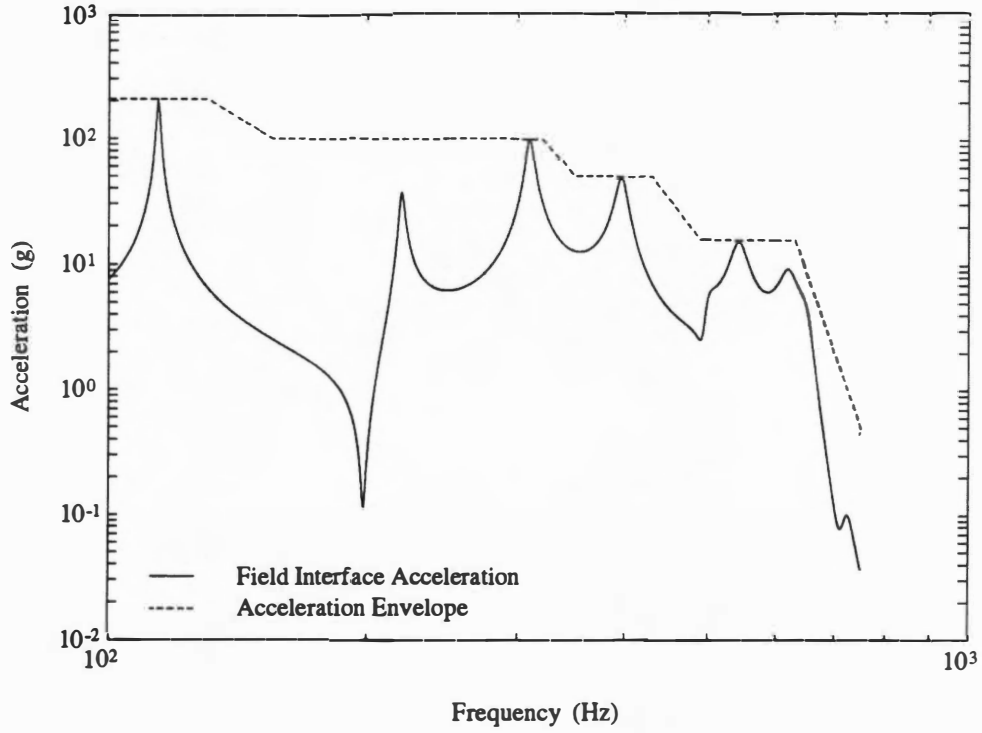

Figure 5.1 Acceleration FRF of m_7 from 10-DOF field results with envelope of peaks for force-acceleration product test.

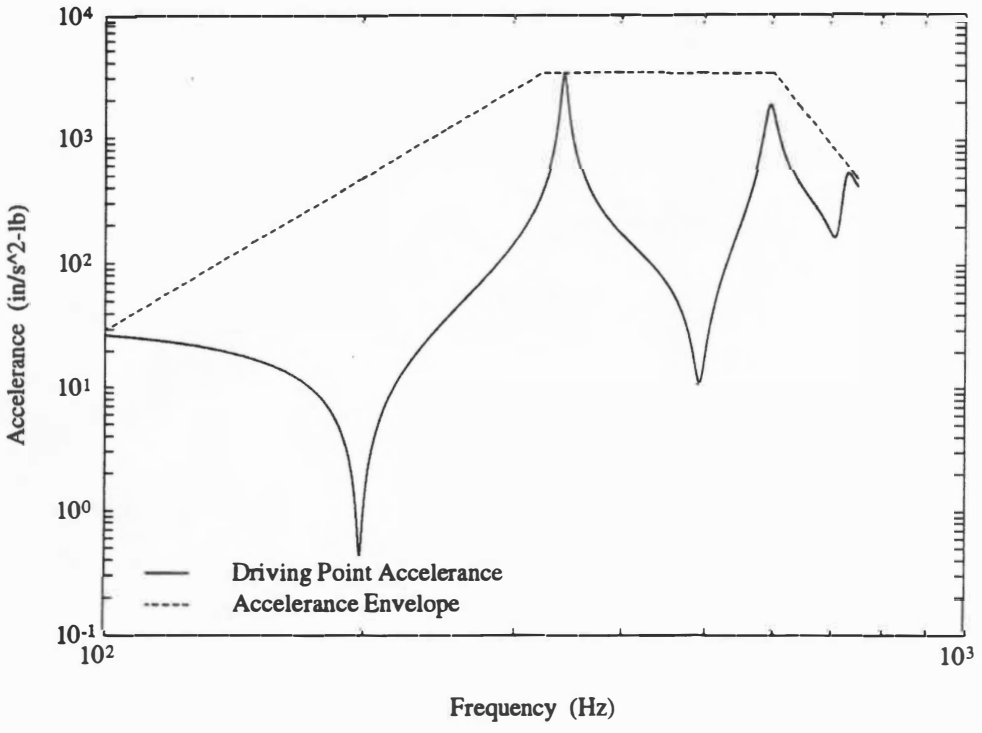

Figure 5.2 Driving point accelerance FRF of subsystem *III* with envelope of peaks for force-acceleration test.

the final test input acceleration function, $a_i(\omega)$ (see Fig. 5.3). Figs. 5.4 through 5.6 display the *subsystem III* test results using the force-acceleration product technique, superimposed against the 10-DOF field measurements.

Dual Extremal Control Method

A vibration test method has been proposed where control is accomplished using extremal control of the force and acceleration at the input to a test item [11, 23-27]. In a dual extremal test, the control is based on which parameter, input force or input acceleration, reaches its envelope first. This is accomplished by establishing both a force control spectrum and an acceleration control spectrum and then monitoring both input force and input acceleration during the vibration test. The acceleration control spectrum is established by enveloping the peaks of the interface motion from field measurements or from calculated levels (similar to the field acceleration envelope used in the force-acceleration product method). The force control spectrum is ideally determined from interface force measurements in the field environment or more commonly from calculated levels. The test will then be controlled such that the test input spectra are never larger than these two envelopes. It should be noted that there are several alternative methods used to determine the force control spectrum, the various methods used to generate this control spectrum will be reviewed in subsequent chapters.

To demonstrate this method the same 10-DOF model is used. The procedure is to envelope both field acceleration and force levels from the combined 10-DOF system, then control the subsystem test such that the test spectra are never larger than these two envelopes. The same assumptions regarding single axis input apply for this demonstration.

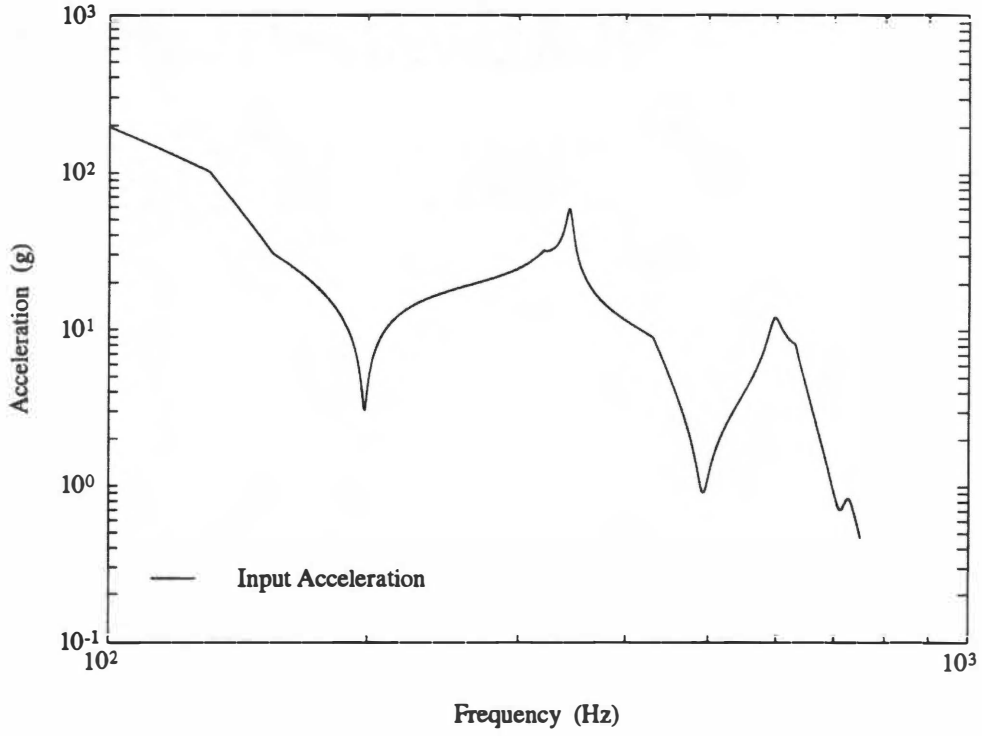

Figure 5.3 Input acceleration FRF to be applied to subsystem *III* for force-acceleration product test.

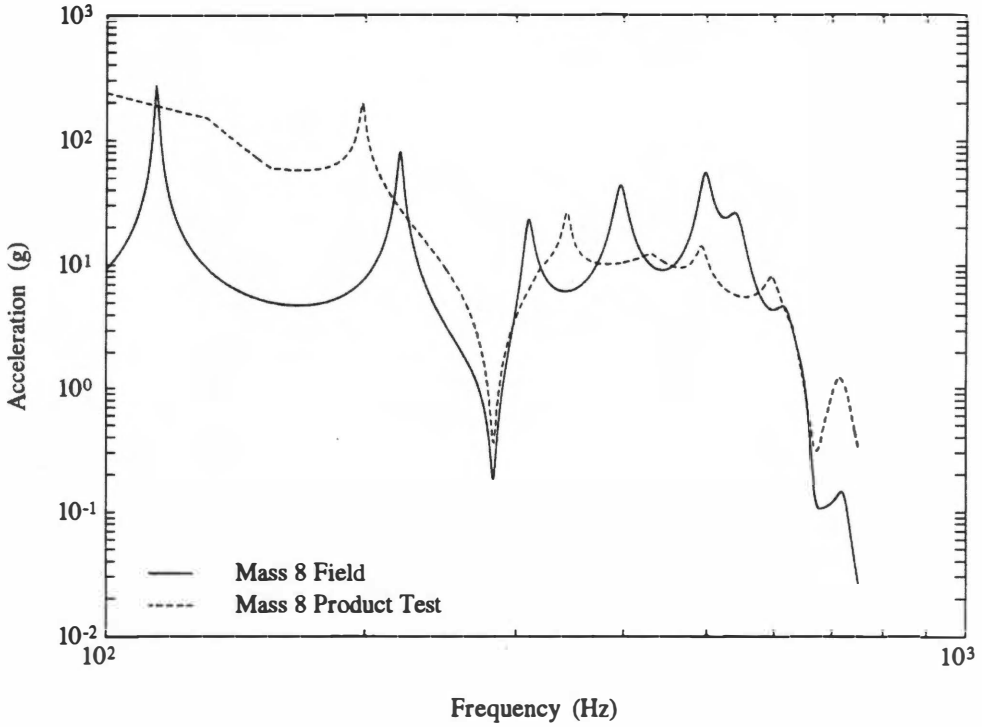

Figure 5.4 Acceleration of m_8 comparing 10-DOF field results to those obtained from subsystem *III* test using force-acceleration.

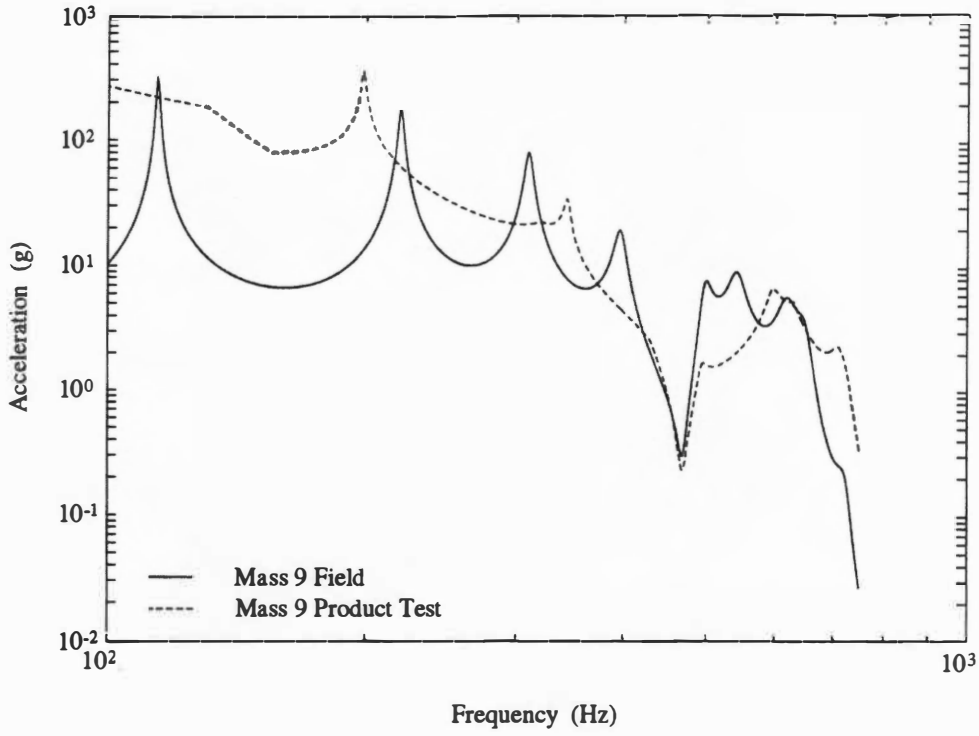

Figure 5.5 Acceleration of m_9 comparing 10-DOF field results to those obtained from subsystem *III* test using force-acceleration.

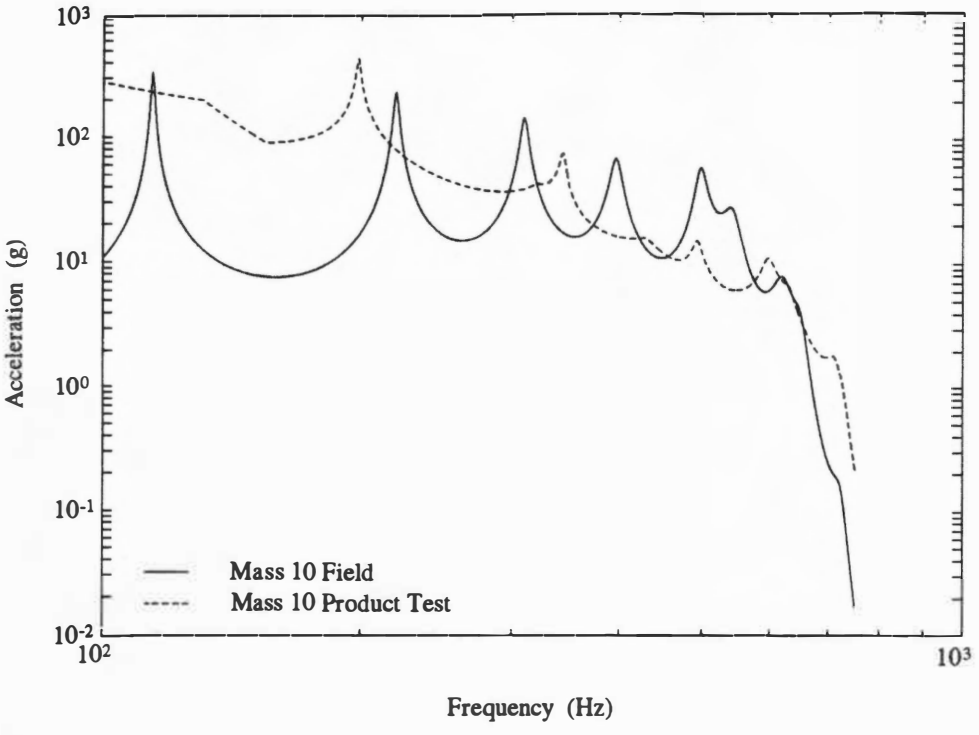

Figure 5.6 Acceleration of m_{10} comparing 10-DOF field results to those obtained from subsystem *III* test using force-acceleration

Fig. 5.7 is a plot of the acceleration control spectrum shown as an envelope of m_7 maximum interface acceleration levels measured for the 10-DOF system. Fig. 5.8 is a plot of the force control spectrum shown as an envelope of m_7 maximum interface force levels extracted from the 10-DOF system results. Fig. 5.9 displays the final input acceleration function that is automatically generated during the subsystem test based on the input force and acceleration magnitudes. Figs. 5.10 through 5.12 show the *subsystem III* test results using the dual extremal control technique, superimposed against the 10-DOF field measurements.

Transmissibility Correction Method

A vibration test method has been proposed to correct for mechanical impedance effects by reducing (notching) the vibration input during the test, around the major structural resonance of the subsystem specimen [28]. Acceleration transmissibility data collected during a preliminary low level resonance survey is used to notch the input acceleration spectrum. The input vibration notch shape is defined as the nominal input acceleration divided by the subsystem transmissibility function. Input acceleration correction is performed out to the equipment fundamental resonance, f_n, or in other words the correction frequency range starts at the lowest test frequency and continues to the upper correction frequency where the transmissibility curve becomes less than one or to the frequency where $f_c = \sqrt{2}f_n$.

The key element in using the transmissibility correction method is in deciding which level of structure, within the subsystem, is to be used for determining the transmissibility correction function. A reasonable approach is to select the most damage sensitive level of structure within the subsystem to use as the correction focal point.

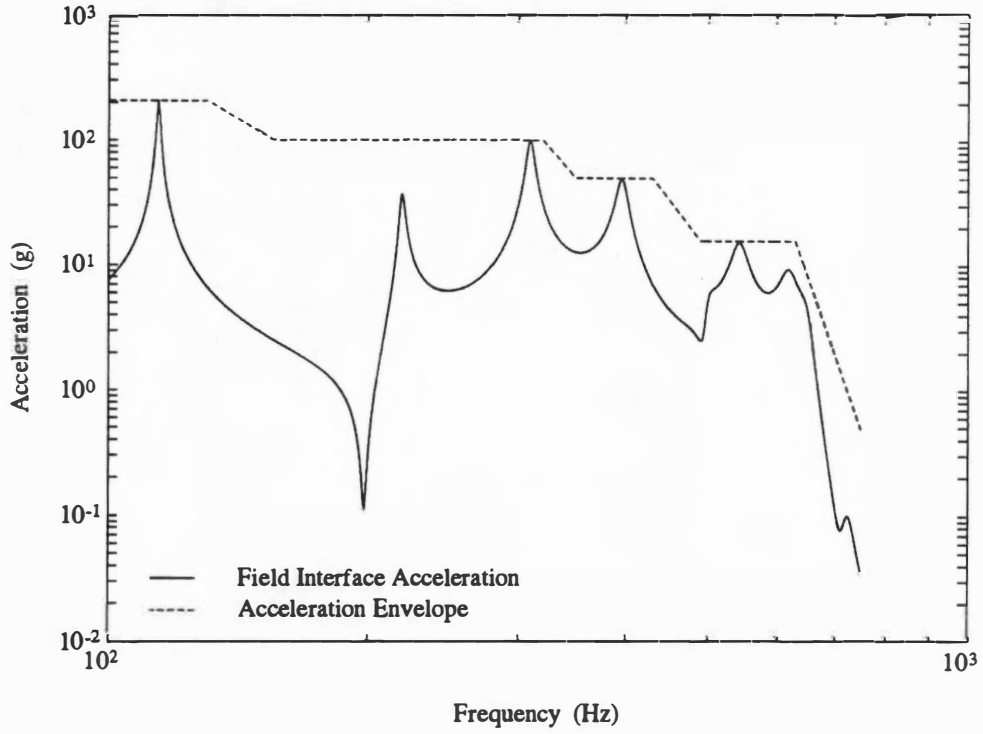

Figure 5.7 Acceleration control spectrum shown as an envelope of peak m_7 interface levels for dual control test.

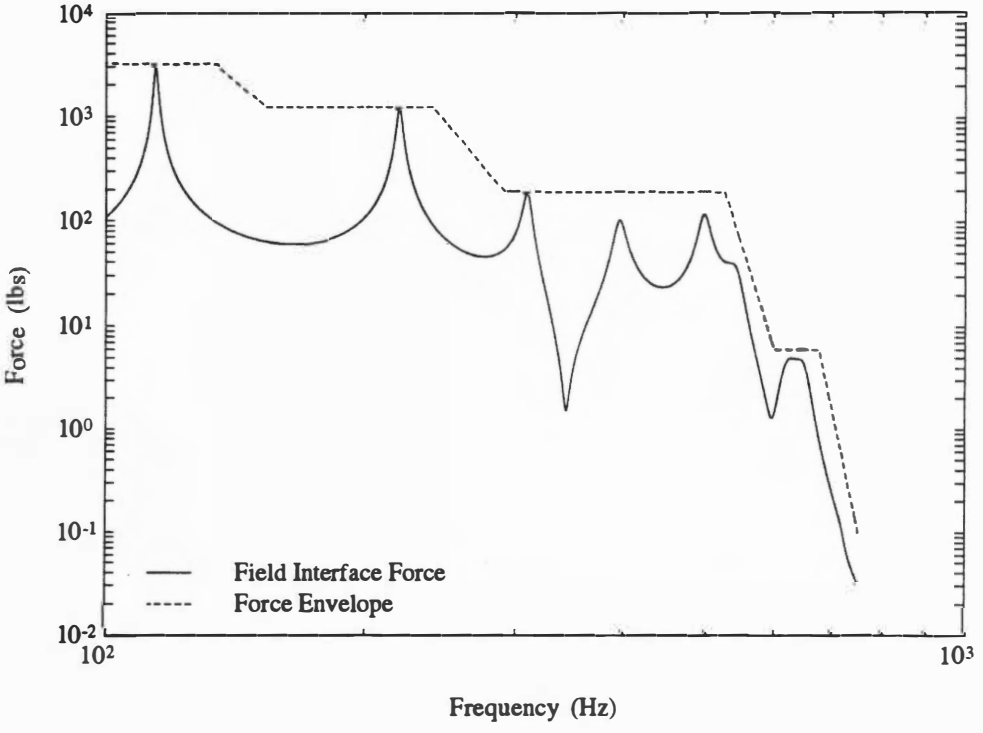

Figure 5.8 Force control spectrum shown as an envelope of peak m_7 interface levels for dual control test.

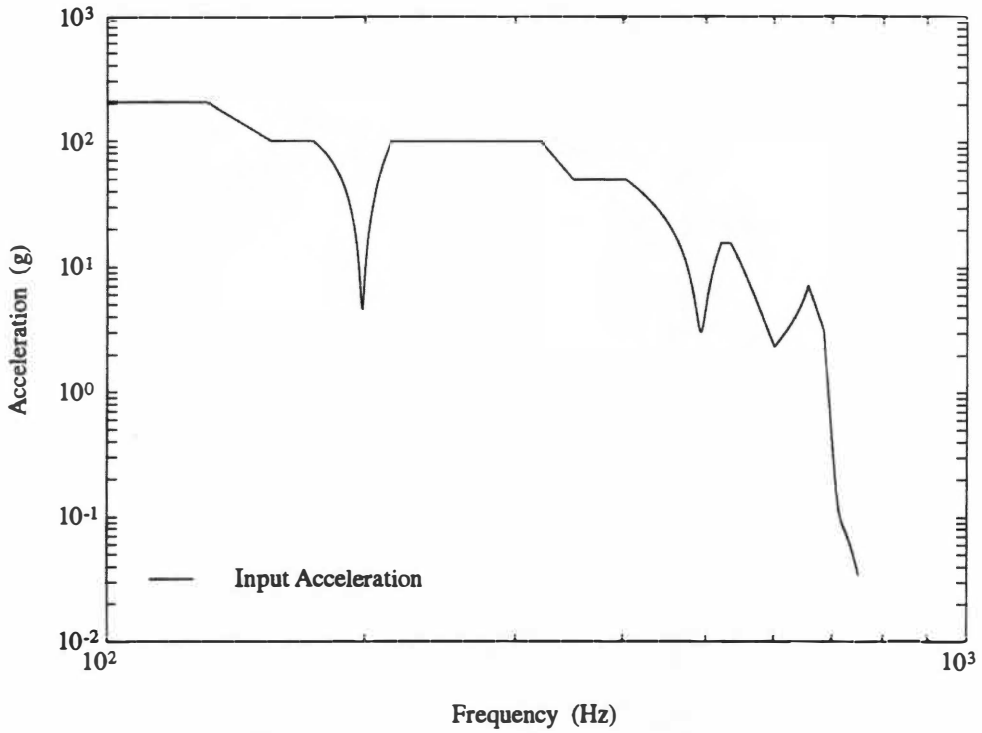

Figure 5.9 Input acceleration FRF to be applied to subsystem *III* for dual control test.

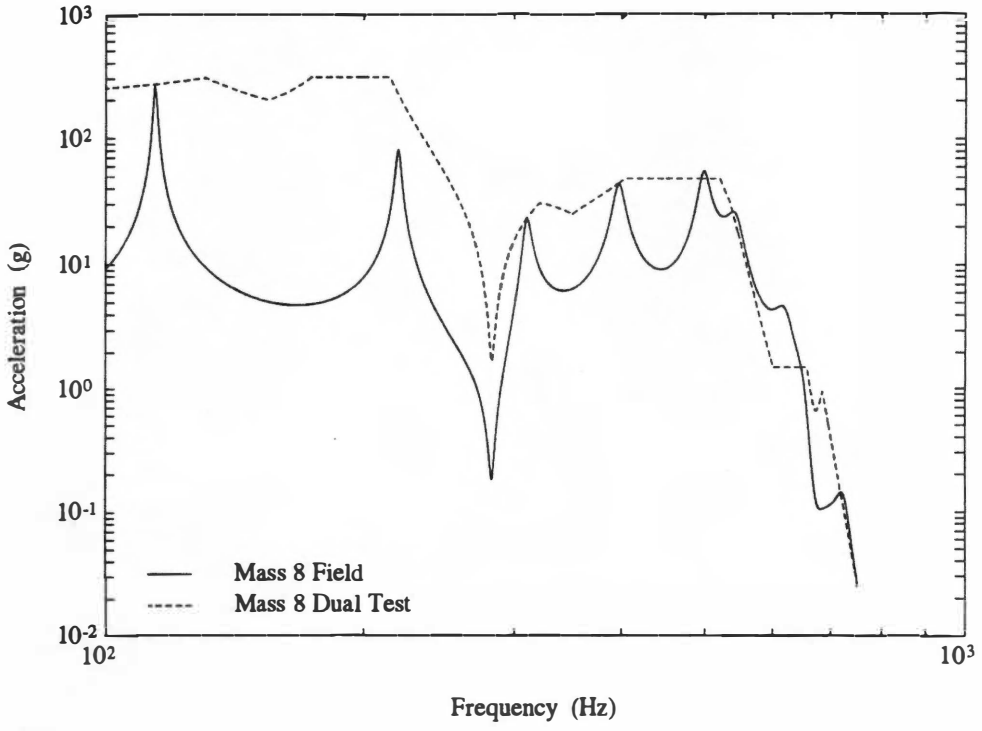

Figure 5.10 Acceleration FRF of m_8 comparing 10-DOF field results to those obtained from subsystem *III* test using dual control.

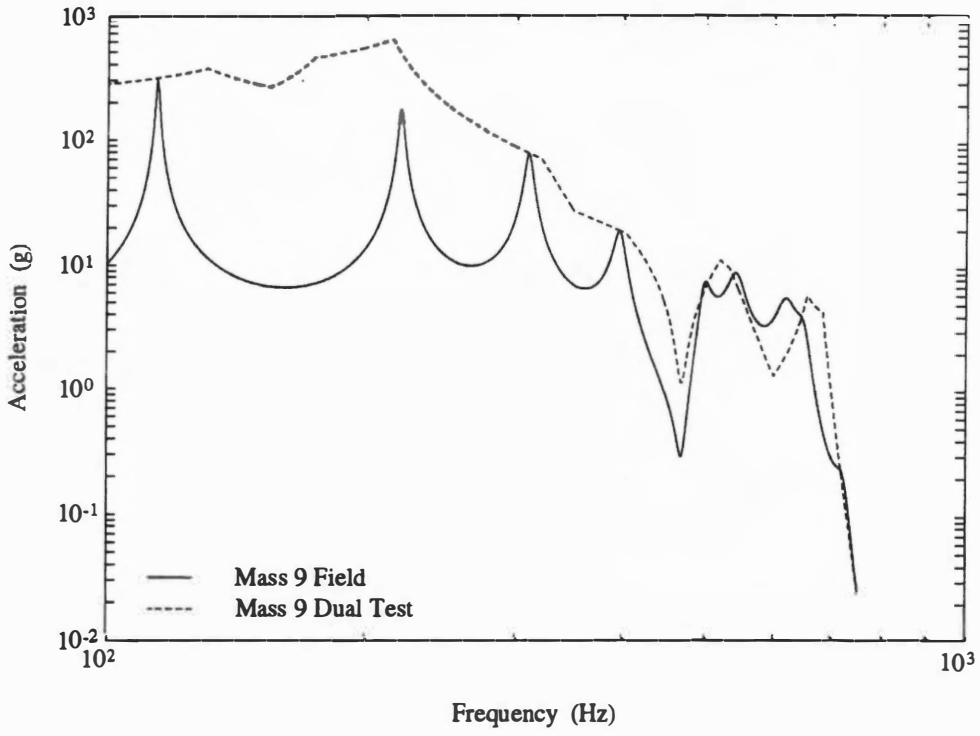

Figure 5.11 Acceleration FRF of m_9 comparing 10-DOF field results to those obtained from subsystem *III* test using dual control.

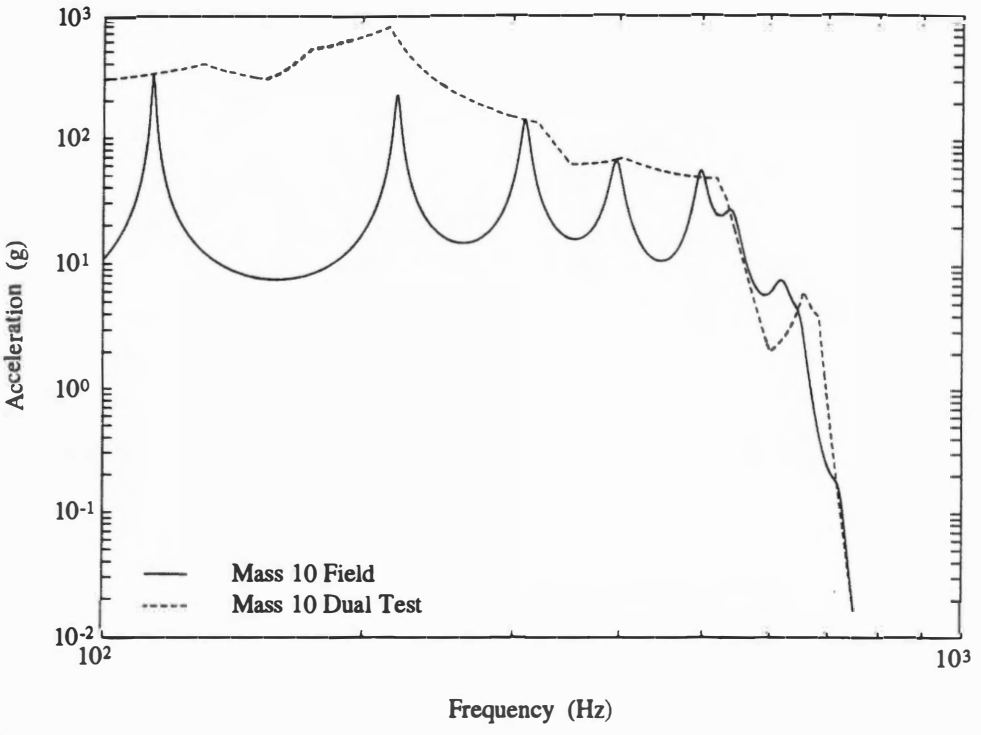

Figure 5.12 Acceleration FRF of m_{10} comparing 10-DOF field results to those obtained from subsystem *III* test using dual control.

The 10-DOF model will again be used to demonstrate this method. The procedure is to envelope the maximum field acceleration levels from the 10-DOF system, perform a low level resonance survey on the subsystem test item, calculate the subsystem transmissibility function and then divide the acceleration envelope by the subsystem transmissibility function, over the frequency correction range. The resulting ratio of acceleration envelope divided by the transmissibility function is the input acceleration, $a_i(\omega)$, which can be applied using an infinite impedance test setup.

Fig. 5.13 is a plot of the acceleration control spectrum shown as an envelope of m_7 maximum interface acceleration levels from the 10-DOF system. In this example m_{10} represents a damage sensitive instrument and therefore transmissibility correction is based on the m_{10} location within *subsystem III* (m_7 is used for *subsystem II* test). Fig. 5.14 displays the m_{10} transmissibility function and Fig 5.15 is the ratio of enveloped acceleration divided by the m_{10} transmissibility, over the frequency correction range (the final input acceleration). Figs. 5.16 through 5.18 display the *subsystem III* test results using the transmissibility correction method, superimposed against the 10-DOF field measurements.

Vibration Test Method Comparison

The three impedance vibration test methods demonstrate considerable realism when compared to a motion controlled, infinite impedance test (realism being defined as a close approximation of the field vibration environment). Each method allows the test specimen dynamics to affect the input vibration environment, and thus, the possibility of a serious overtest is eliminated. Figs. 5.19 through 5.21 compare results obtained using an infinite impedance test versus test data using the three mechanical impedance

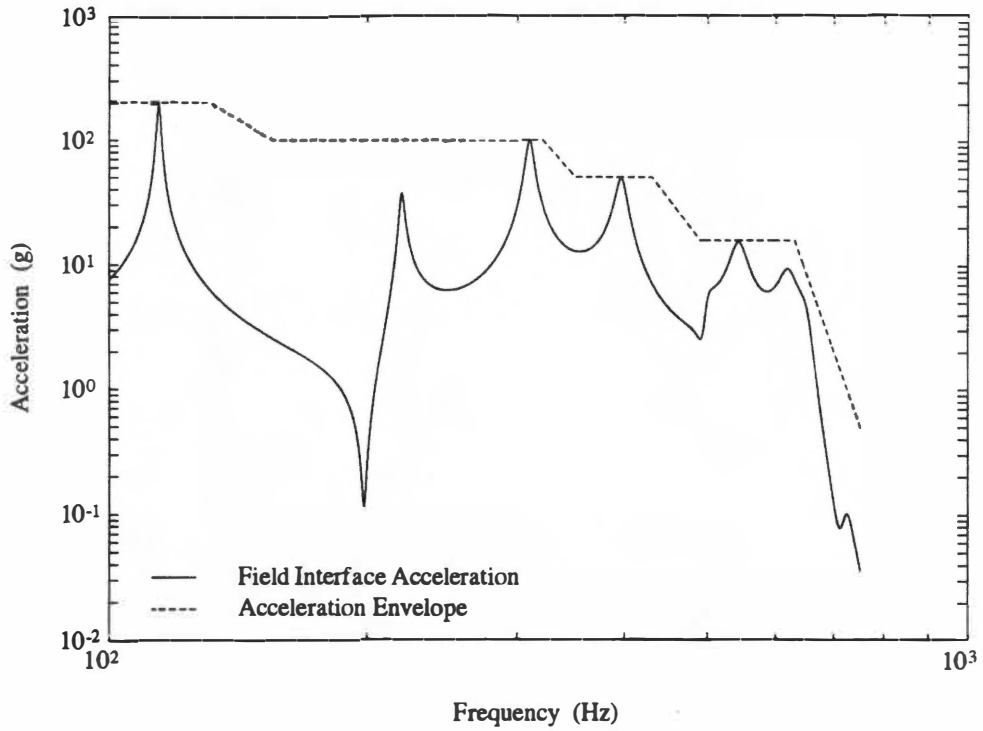

Figure 5.13 Acceleration FRF of m_7 from 10-DOF field results with envelope of peaks for transmissibility correction test.

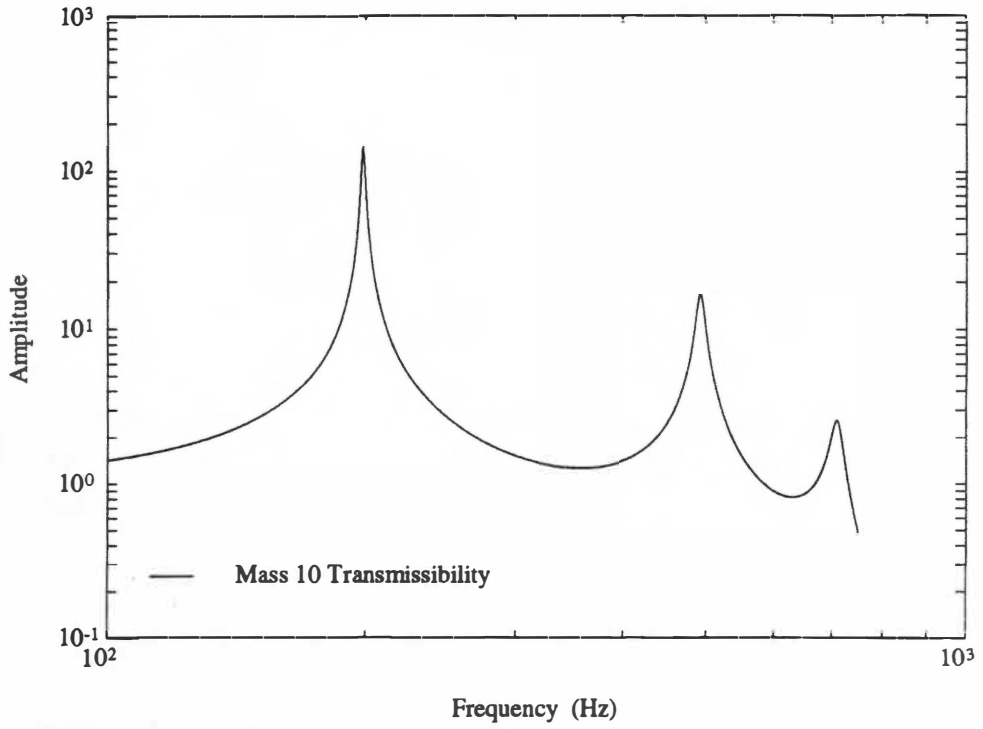

Figure 5.14 Transmissibility FRF of m_{10} for transmissibility correction test.

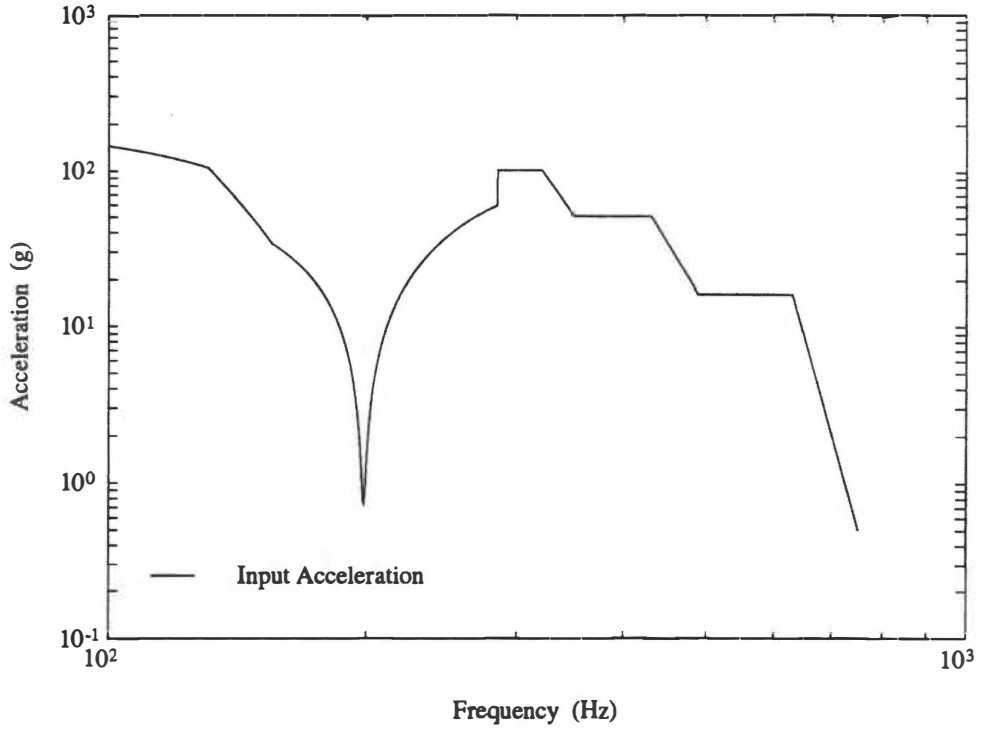

Figure 5.15 Input acceleration FRF to be applied to subsystem *III* for transmissibility correction test.

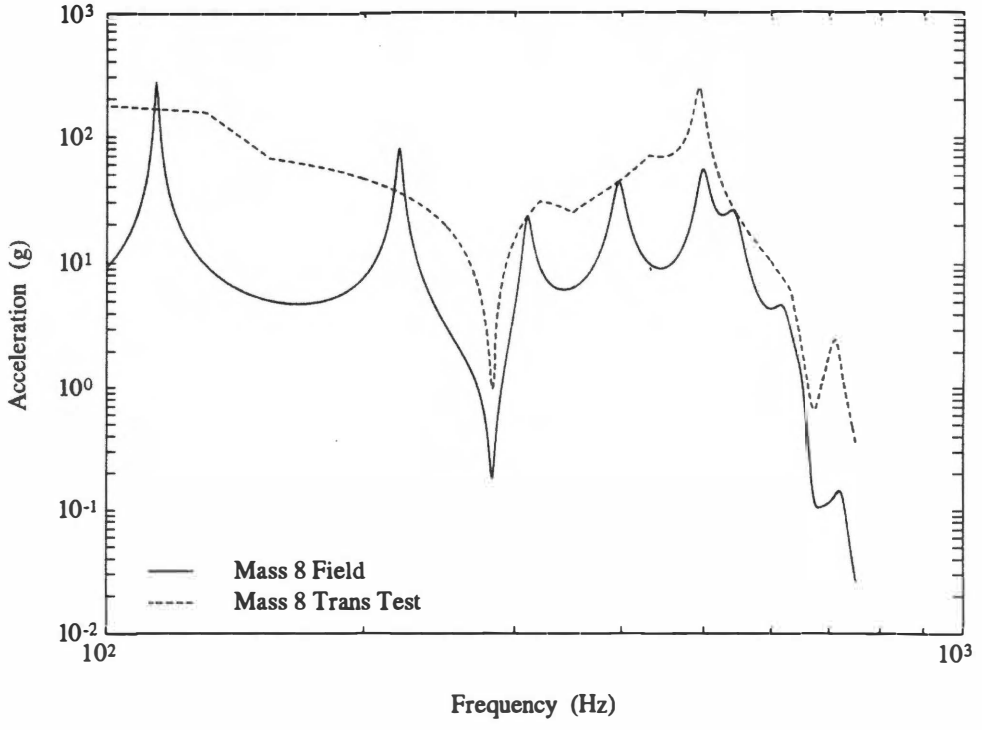

Figure 5.16 Acceleration of m_8 comparing 10-DOF field results to those from subsystem *III* test using transmiss. correction.

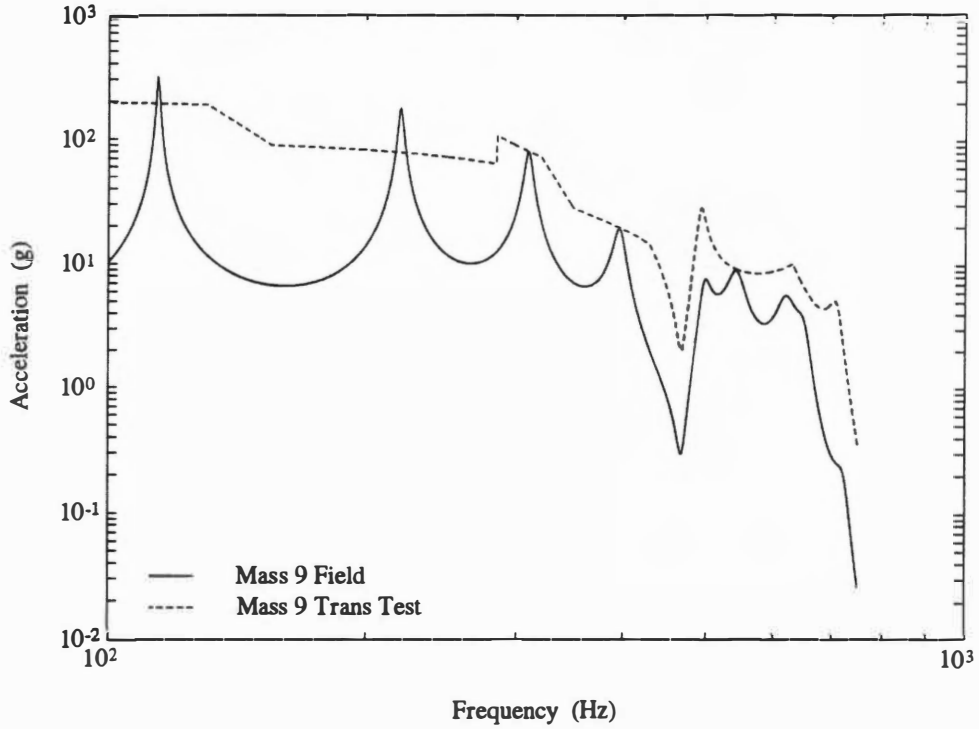

Figure 5.17 Acceleration of m_9 comparing 10-DOF field results to those from subsystem *III* test using transmiss. correction.

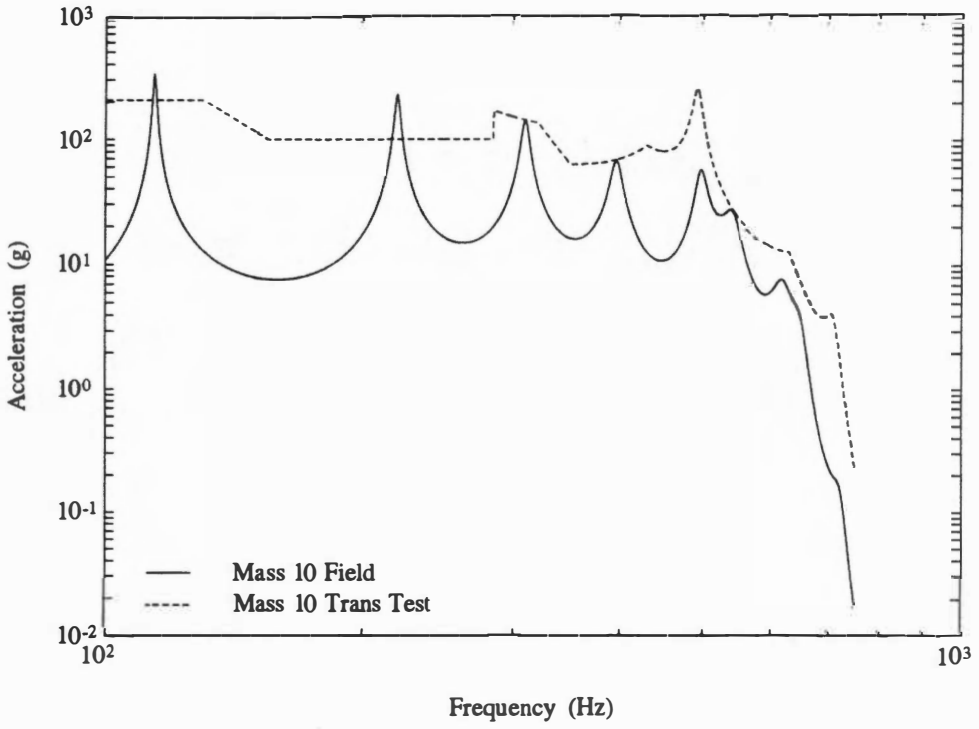

Figure 5.18 Acceleration of m_{10} comparing 10-DOF field results to those from subsystem *III* test using transmiss. correction.

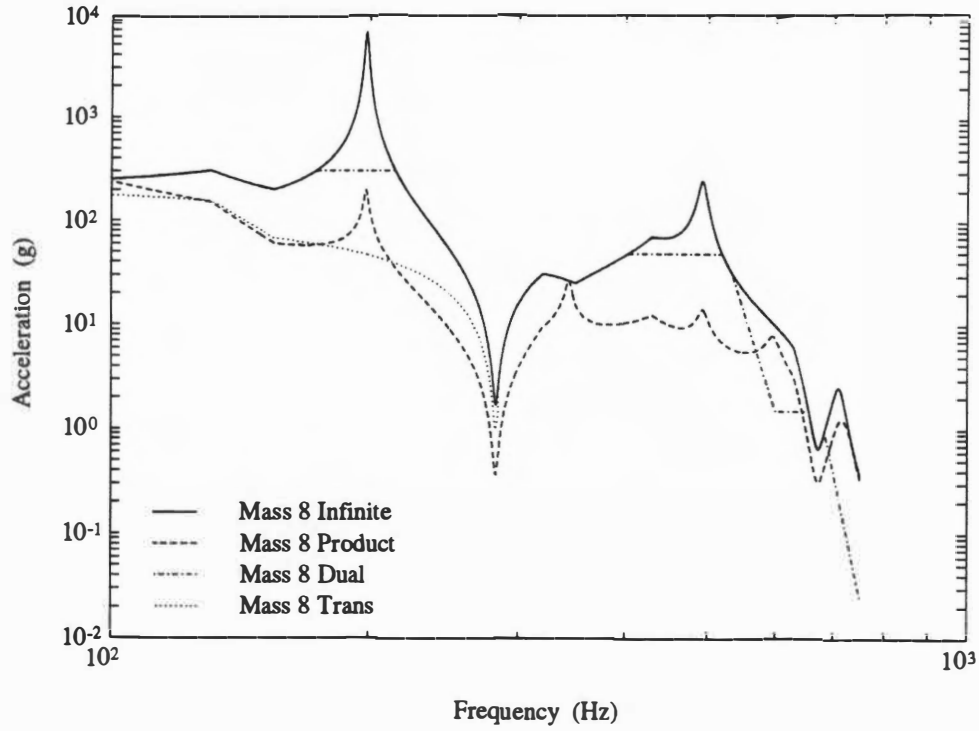

Figure 5.19 Acceleration FRF of m_8 comparing the three impedance test methods vs. an infinite impedance test for subsystem *III*.

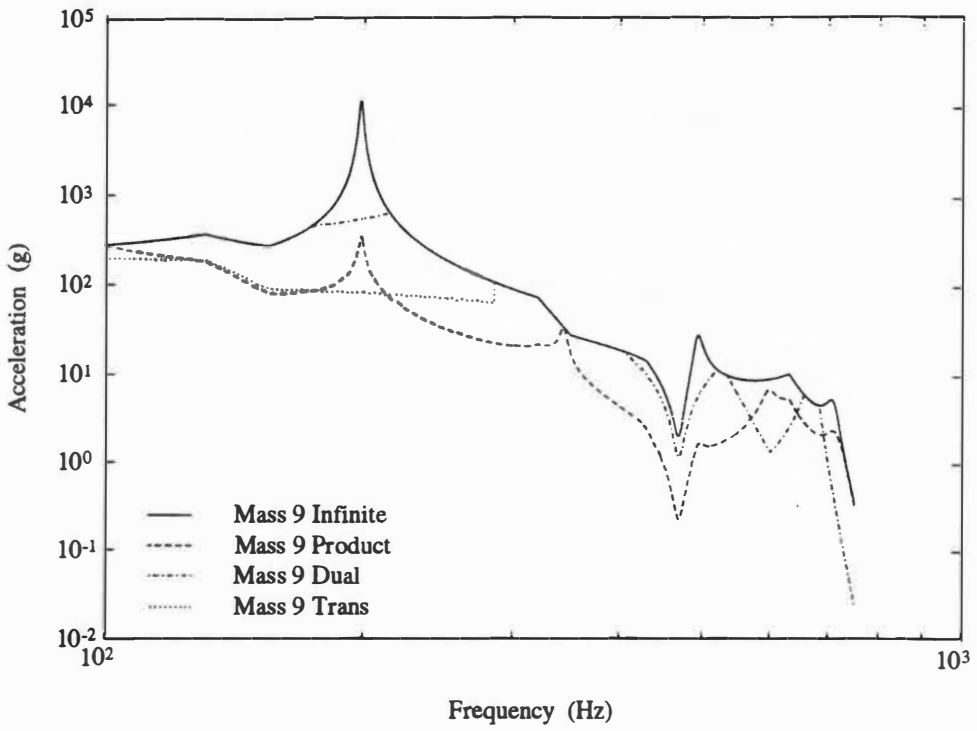

Figure 5.20 Acceleration FRF of m_9 comparing the three impedance test methods vs. an infinite impedance test for subsystem *III*.

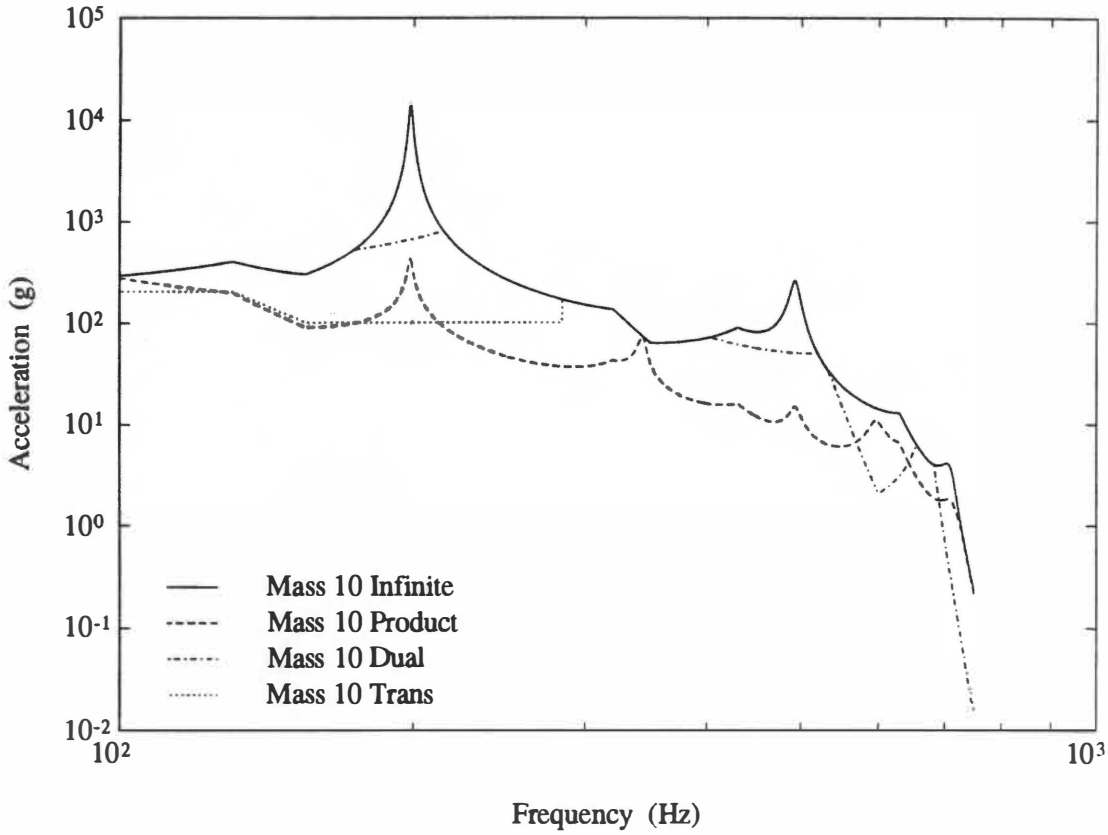

Figure 5.21 Acceleration FRF of m_{10} comparing the three impedance test methods vs. an infinite impedance test for subsystem *III*.

methods. As can be observed, all three impedance methods are drastic improvements over the unrealistic infinite impedance test.

Determination of the impedance method which most closely duplicates the field vibration environment is not easily discernable from the frequency response plots. In order to quantify the amount of vibration each method imparts into the test specimen, a vibration equivalence calculation based on accumulated damage is required. The next chapter evaluates vibration equivalence for a real structural system to determine which of the three impedance methods most closely duplicates the real vibration environment.

CHAPTER 6

VIBRATION EQUIVALENCE - SIMULATION OF FIELD ENVIRONMENT

Vibration equivalence based on cumulative damage theory is assumed to exist when two or more vibration experiences produce like amounts of damage in a given specimen. All vibration experiences are assumed to cause damage, and the relationship between vibration experience and damage must be known or assumed. The concept of cumulative damage is that every load cycle causes incremental damage, which is accumulated until a certain level of damage is reached at which the specimen will fracture. Equivalences based on cumulative damage draw heavily on various theories developed to explain material fatigue processes [29].

Linear Cumulative Damage

Miner's [30] method of linear cumulative damage is the most universally applied damage criterion and is relatively simple to apply. Miner's theory propounds a simple summation of the fraction of usable specimen life consumed at each load level during a specimens load history. Fatigue damage is assumed to be proportional to work absorbed in the test specimen. The absorbed work in turn is considered proportional to a ratio of the number of applied stress cycles to the number of stress cycles that will produce failure at the given stress level. It is assumed that the amount of damage required to fail a specimen is constant, that the amount of damage is a simple function of load, and that damage is independent of load sequence. Failure is predicted when a sum of the fractional damage from all sources of cyclic stress is equal to one:

$$D = \sum_{i=1}^{m} \frac{n_i}{N_i} = 1 \ (\textit{at failure}) \tag{6.1}$$

where n_i equal the number of cycles experienced by the specimen at load i, and N_i equals the number of cycles to failure at load i obtained from an appropriate material S-N curve.

Experimental Study

To compare the three impedance test methods of Chapter 5 it is necessary to calculate the cumulative damage each method imparts into a test specimen. To accomplish this task a simple structural system is needed to perform vibration testing and to calculate the resulting cumulative damage for each test method. A mild carbon steel (ANSI 1018) beam structure is fabricated to serve as the structural test system. Fig. 6.1 is an isometric view of the fabricated test structure (detailed fabrication drawings are located in Appendix B). The beam structure is designed such that the bottom base plate bolts to a shaker mounting platform and the top beam/block assembly can be detached from the combined structure and mounted directly to the shaker platform. In this regard, the top beam/block assembly can be considered as an equipment item to which a vibration test is to be developed. Fig. 6.2 is an isometric view of the detached top beam/block assembly and will be referred to herein as the subsystem test structure.

The combined structure is instrumented using six piezoelectric accelerometers (Endevco model 2222C) at the locations indicated in Fig. 6.3. Accelerometer #6 is used as the reference control accelerometer. A constant amplitude (3 g input) logarithmic sine sweep vibration test is performed from 20 to 2,000 Hz. The sine sweep test is run for a total of 1,500 seconds and represents the field vibration environment for the combined

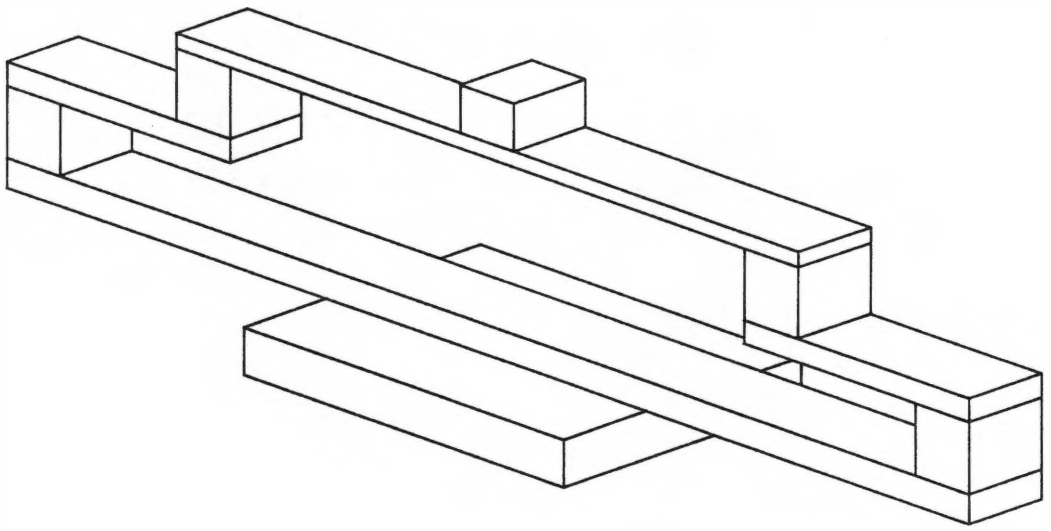

Figure 6.1 Isometric view of beam and block combined test structure for use in combined system vibration testing.

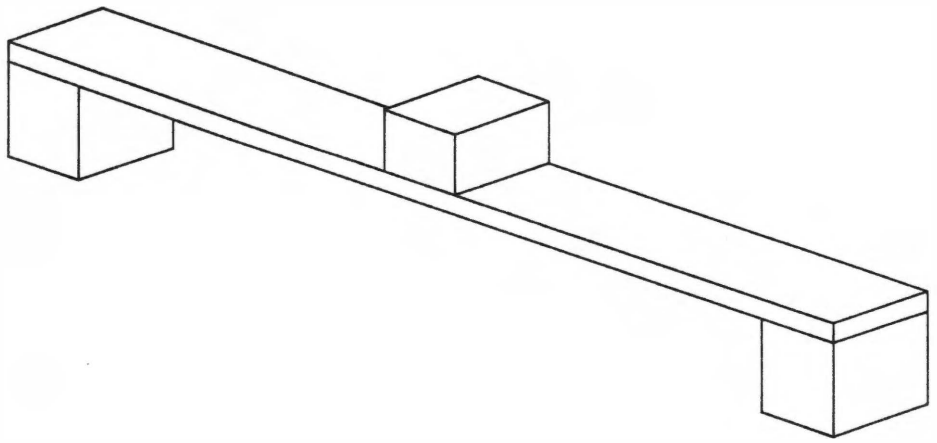

Figure 6.2 Isometric view of subsystem beam and block structure for use in subsystem vibration testing.

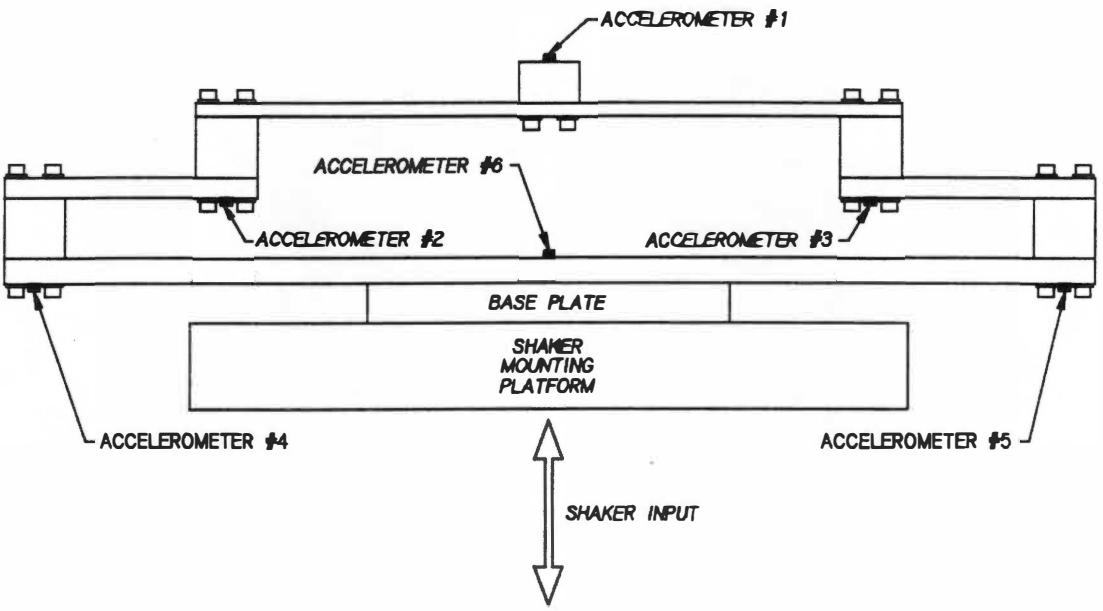

Figure 6.3 Location of accelerometers as instrumented on combined structural system.

structural system. Accelerometer data is recorded on magnetic tape then transferred to a personal computer for data reduction.

Figs. 6.4 through 6.6 display the experimental sine sweep test results for the combined structural system. The results obtained using the two midpoint location accelerometers (Fig. 6.5) and the two bottom point location accelerometers (Fig. 6.6) are in close agreement to each other (#2 vs. #3 and #4 vs. #5). This is a good indicator that no major errors were made during setup, testing and data reduction (the structure is symmetrical).

A detailed mathematical finite element model (FEM) is generated of the combined structural system. The FEM is generated using the ANSYS general purpose finite element computer program. The computer model is a two-dimensional plane stress representation of the combined structure, with the depth dimension (2 inches) input as a material constant. The material densities are based on weight measurements taken from the real structure. Since the bolted connections, attaching the beams and block, are neither fixed or simply supported these connections are modeled using longitudinal and lateral spring elements. The advantage of using local springs, at the bolted connection locations, is in the ability to "tune" the FEM to match the natural frequencies of the real test structure.

A modal analysis is performed to determine the FEM's undamped natural frequencies and mode shapes. As indicated, several iterations are performed, adjusting the spring rate values, until the natural frequencies match the experimental results. Figs. 6.7 through 6.12 display the resulting mode shapes. A comparison of experimental versus

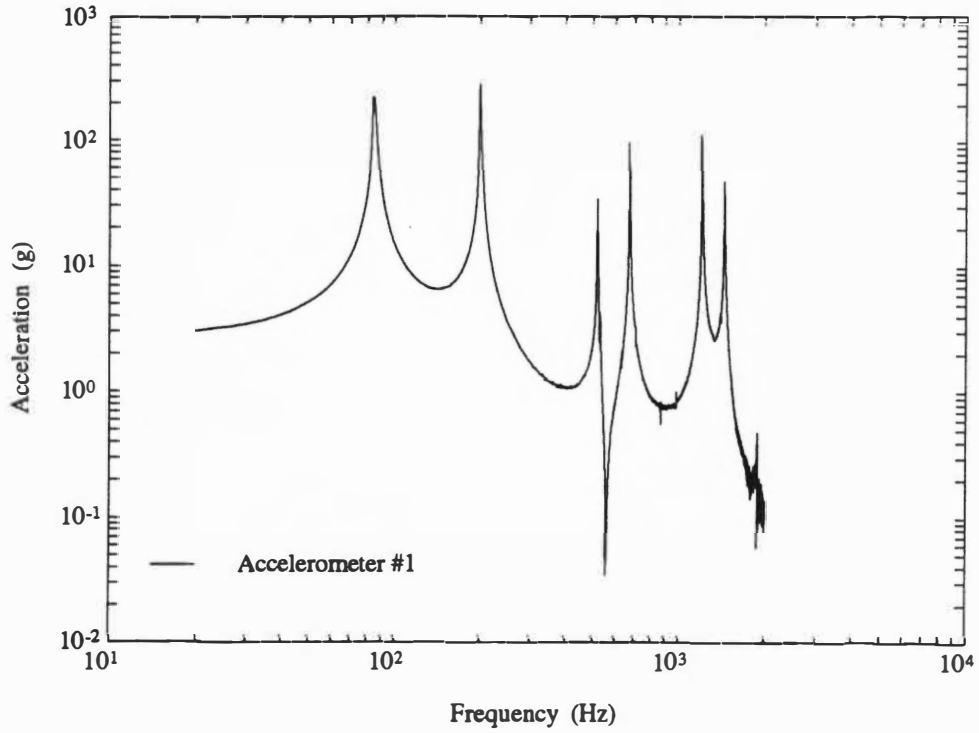

Figure 6.4 **Experimental test data results for combined system - accelerometer location #1.**

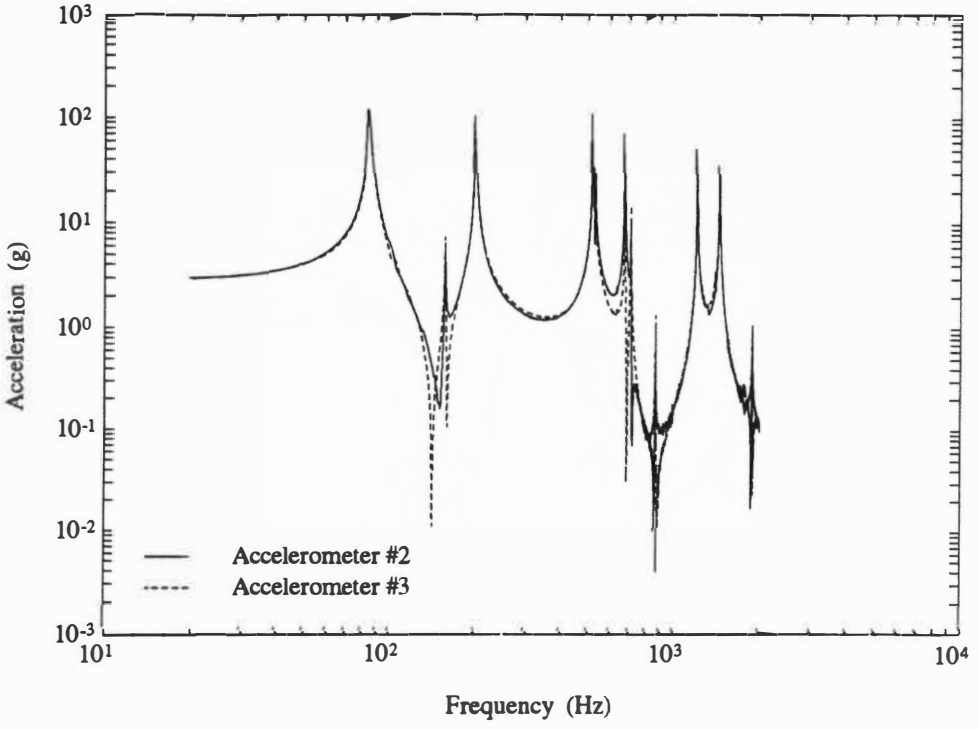

Figure 6.5 **Experimental test data results for combined system - accelerometer locations #2 and #3.**

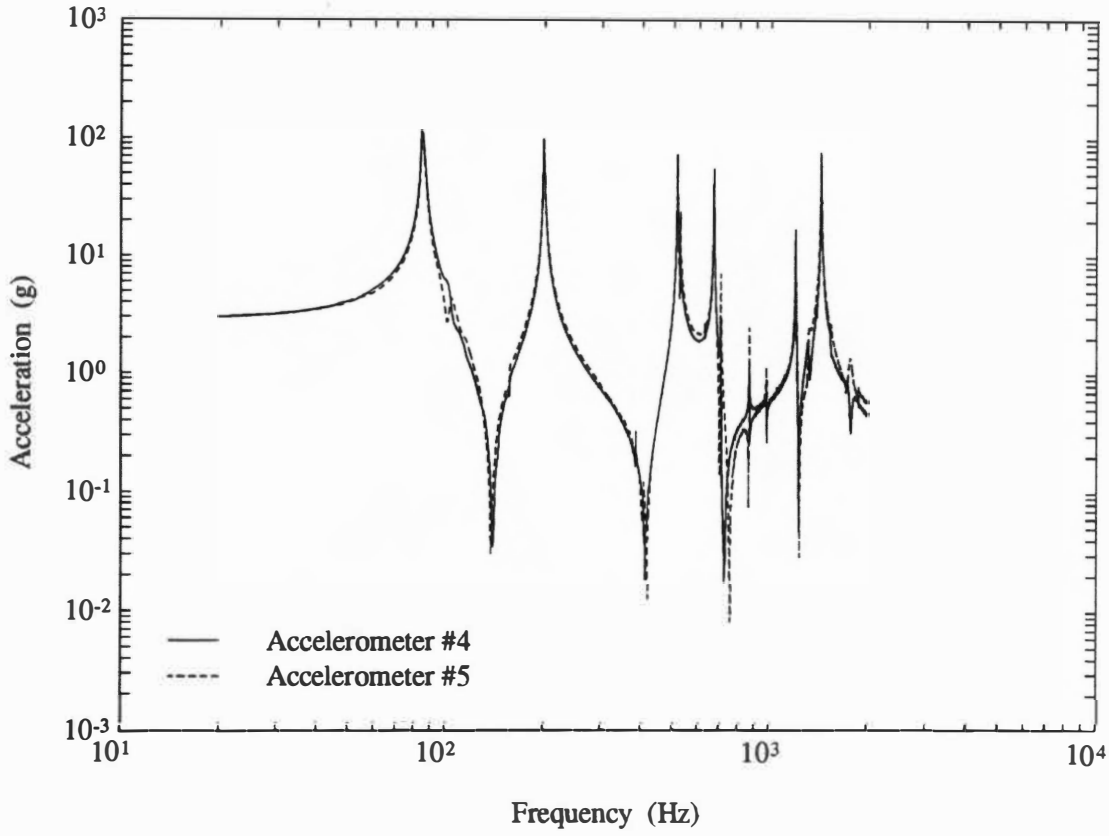

Figure 6.6 **Experimental test data results for combined system - accelerometer locations #4 and #5.**

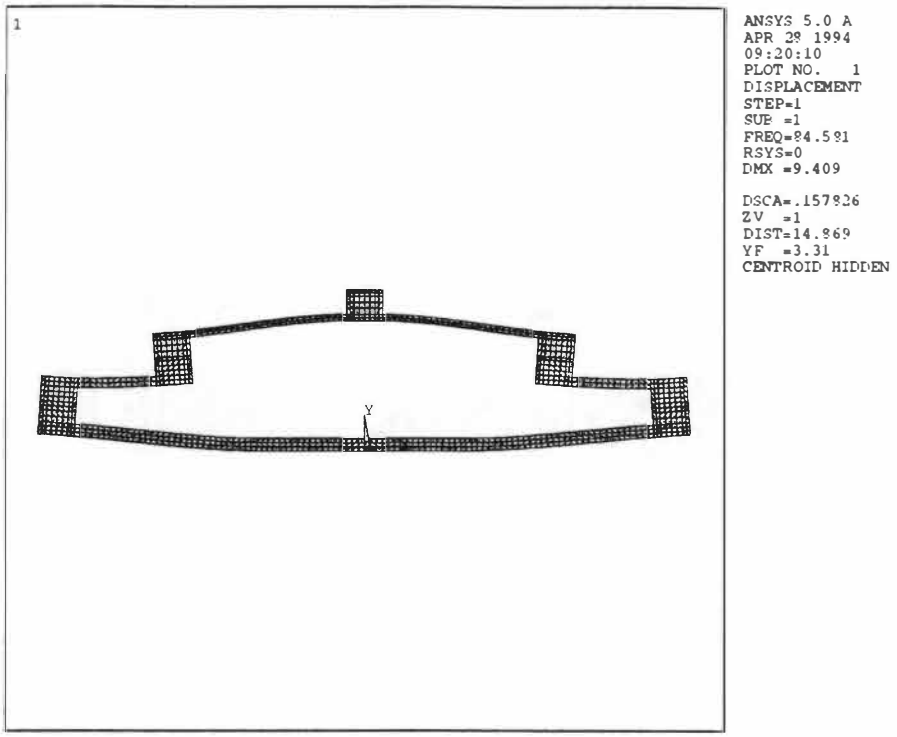

Figure 6.7 First mode shape from finite element modal analysis of the combined structural system.

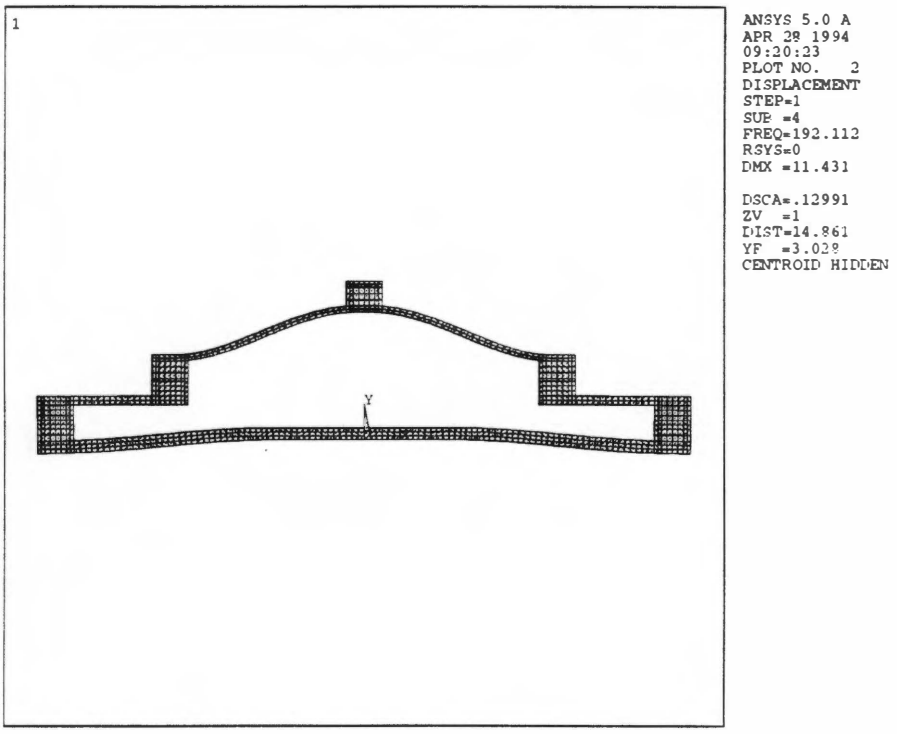

Figure 6.8 Second mode shape from finite element modal analysis of the combined structural system.

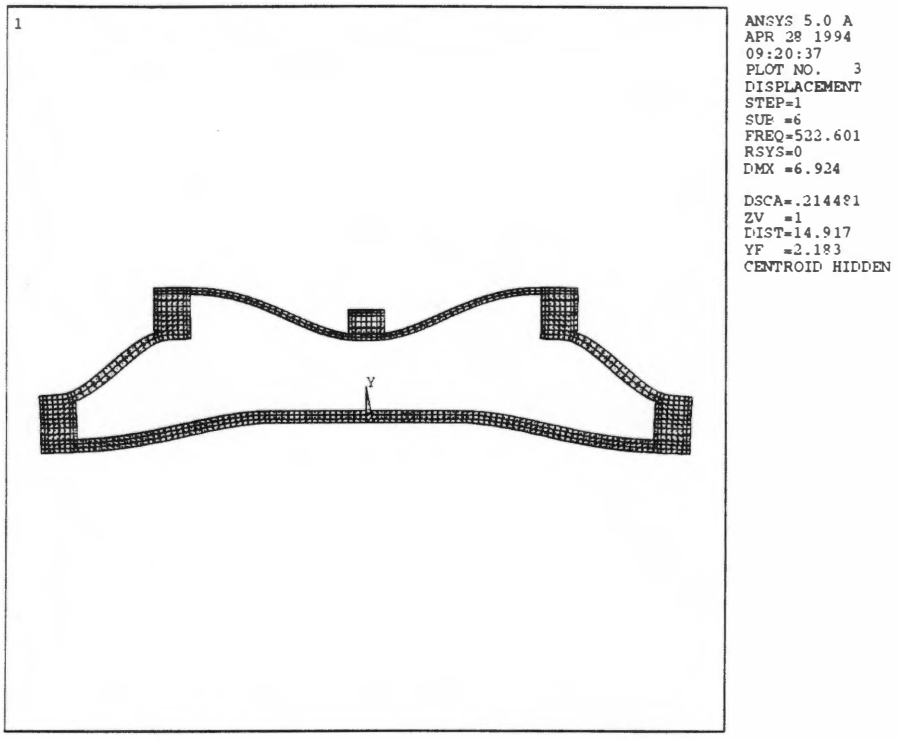

Figure 6.9 **Third mode shape from finite element modal analysis of the combined structural system.**

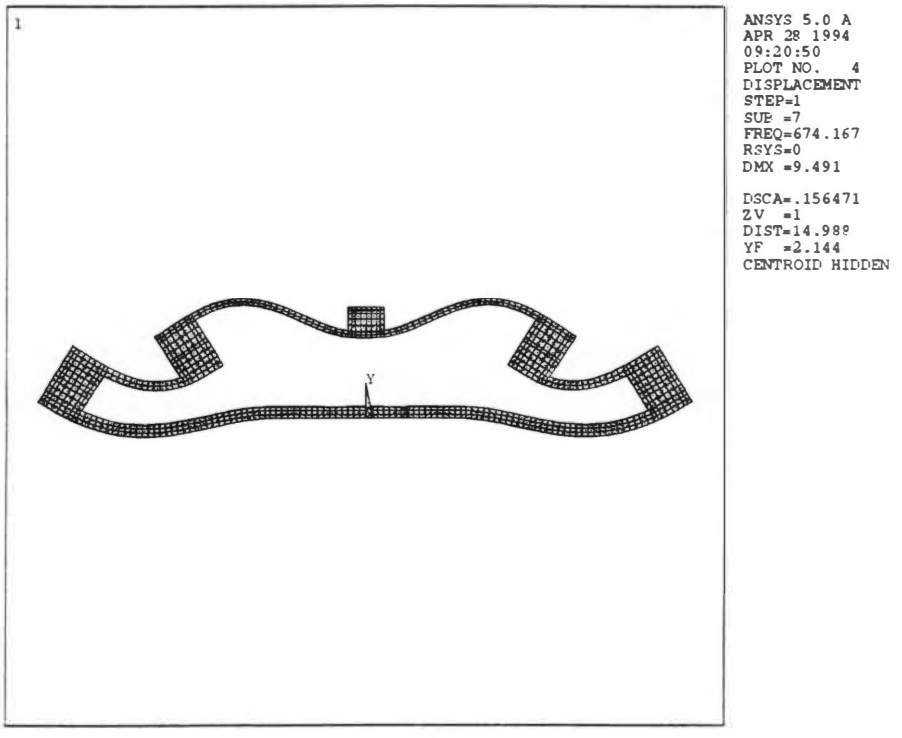

Figure 6.10 **Fourth mode shape from finite element modal analysis of the combined structural system.**

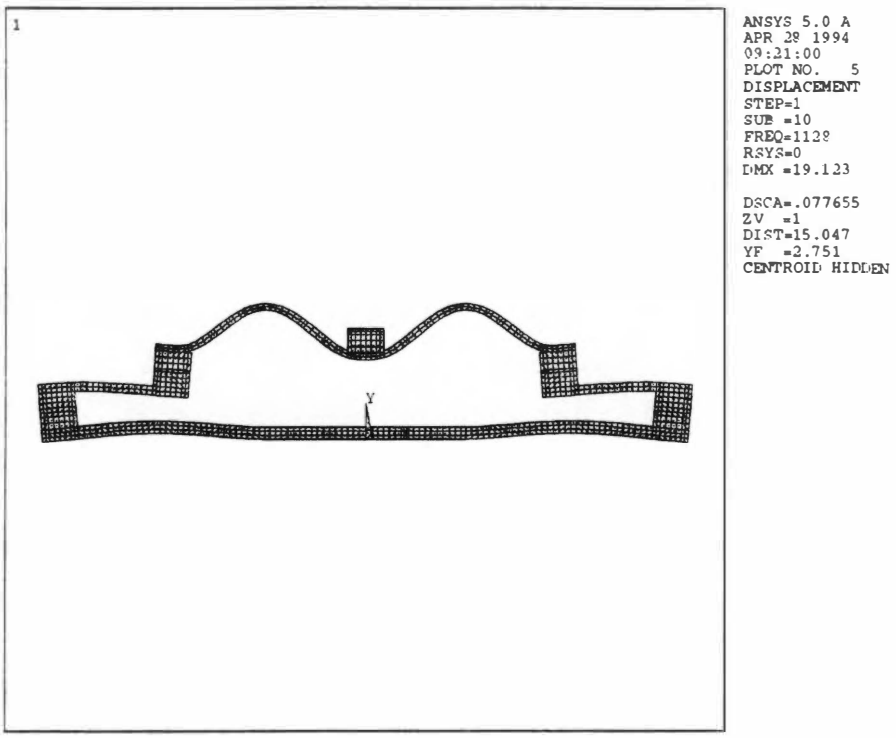

Figure 6.11 Fifth mode shape from finite element modal analysis of the combined structural system.

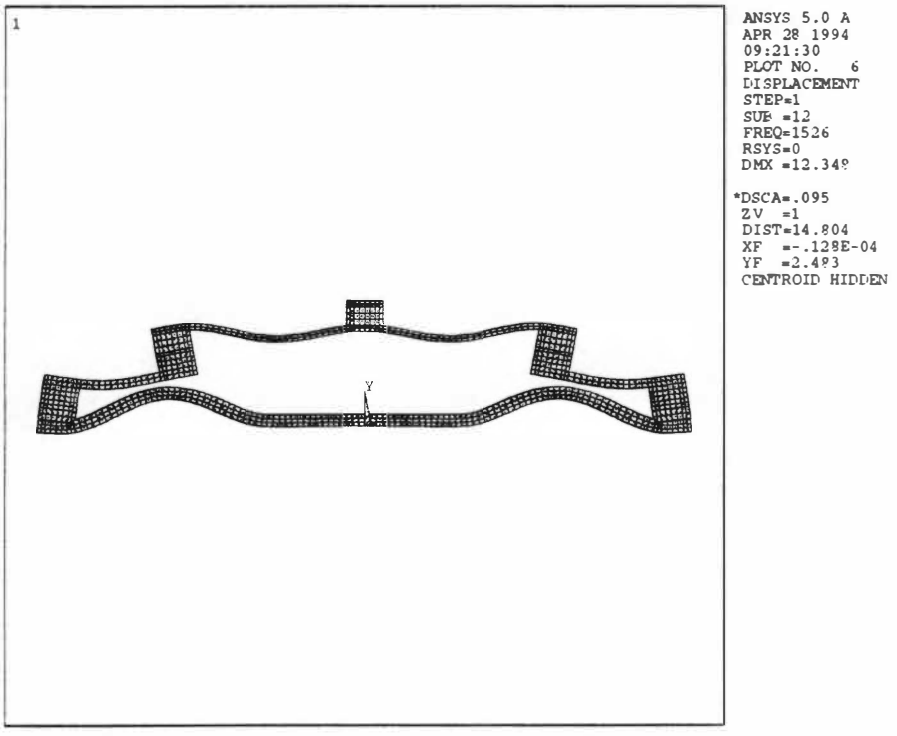

Figure 6.12 Sixth mode shape from finite element modal analysis of the combined structural system.

calculated natural frequencies for the combined structural system is summarized in the following table.

Table 6.1 Experimental vs. calculated natural frequencies, combined system

Experimental (Hz)	Calculated (Hz)	Difference (%)
$f_1 = 85$	$f_1 = 85$	0.00
$f_2 = 199$	$f_2 = 193$	3.02
$f_3 = 518$	$f_3 = 523$	0.97
$f_4 = 673$	$f_4 = 674$	0.15
$f_5 = 1203$	$f_5 = 1128$	6.23
$f_6 = 1441$	$f_6 = 1526$	5.90

The finite element results are in good agreement out to the fifth and sixth modes where a 6.2% and 5.9% deviation exists.

A harmonic analysis is performed on the computer model to duplicate the sine sweep experimental test (3 *g* input from 20 to 2,000 Hz). Figs. 6.13 through 6.15 display the harmonic analysis computer results superimposed against the experimental data. The computer results track closely with the experimental data. The only inconsistencies occur at 782 Hz and 1,900 Hz for the midpoint location experimental data (accelerometer #2), where additional response spikes are present. These spikes may be off-axis coupling or test data anomalies. In either case, the discrepancy is inconsequential since these spikes contribute negligible power into the test specimen (the area under these spikes is small).

The subsystem test can now be attempted. However, to avoid over stressing the

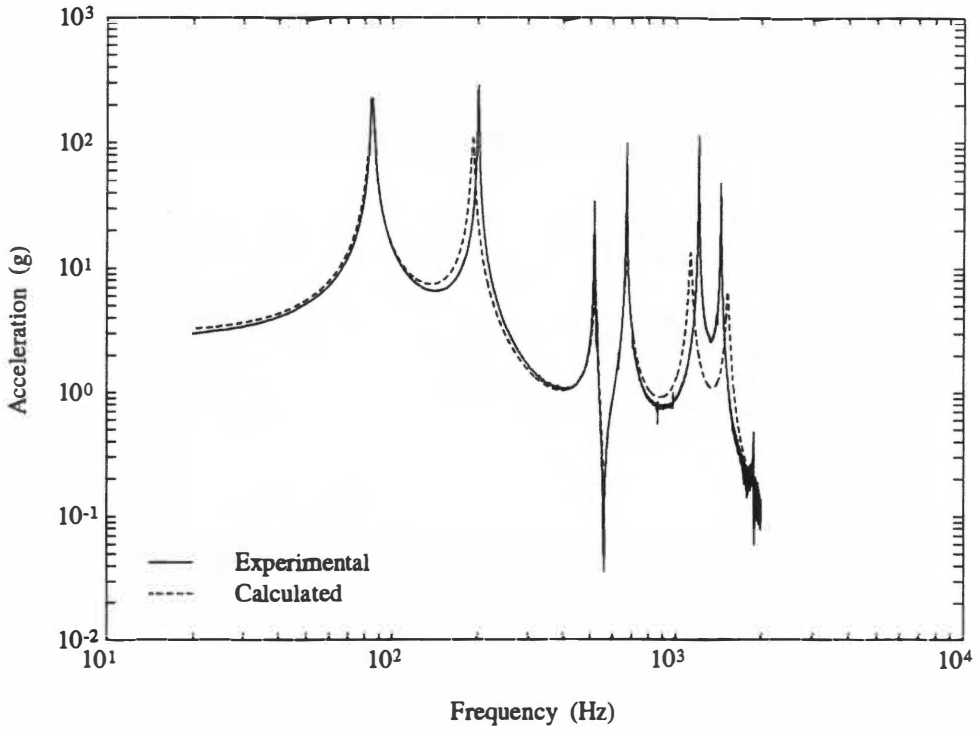

Figure 6.13 Comparison of experimental versus calculated response at accelerometer location #1 for combined system.

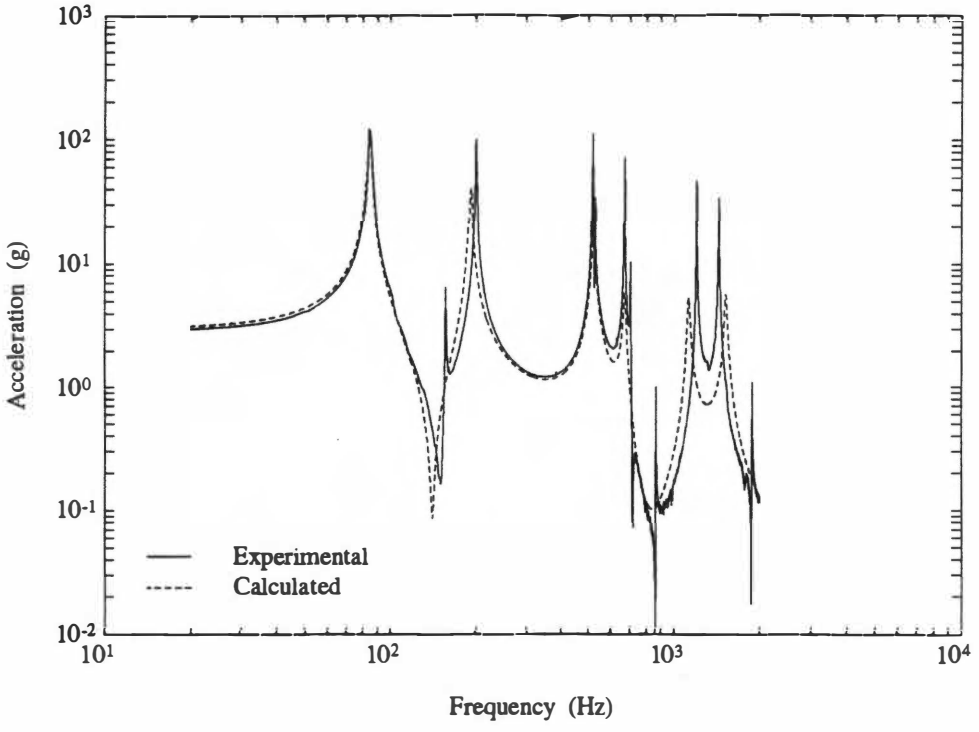

Figure 6.14 Comparison of experimental versus calculated response at accelerometer location #2 for combined system.

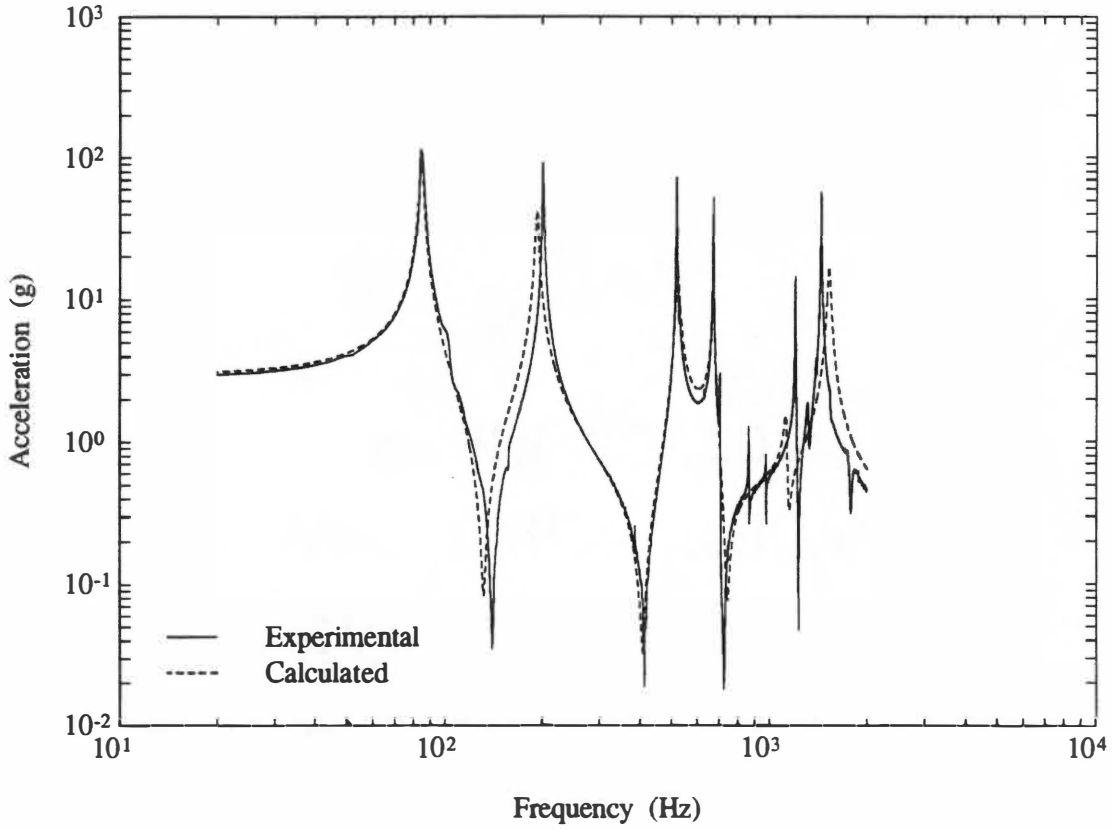

Figure 6.15 Comparison of experimental versus calculated response at accelerometer location #4 for combined system.

steel beam beyond its yield strength (FT_Y = 36,000 psi), a preliminary low level sine sweep subsystem test is performed. The subsystem is removed from the support structure and is directly secured to the shaker platform. The subsystem is instrumented using two accelerometers at the locations indicated in Fig. 6.16. A constant amplitude (1 *g* input) logarithmic sine sweep test is performed from 20 to 2,000 Hz for a total of 1,500 seconds. Accelerometer data is recorded and transferred to PC for data reduction. Fig. 6.17 displays the experimental low level sine sweep test results for the subsystem structure.

A computer modal analysis of the subsystem is performed to determine the subsystem's undamped natural frequencies and mode shapes. Figs. 6.18 and 6.19 display the resulting mode shapes. A comparison of experimental and calculated natural frequencies for the subsystem is as follows:

Table 6.2 Experimental vs. calculated natural frequencies, subsystem

Experimental (Hz)	Calculated (Hz)	Difference (%)
f_1 = 169	f_1 = 169	0.00
f_2 = 1120	f_2 = 1129	0.80

A harmonic analysis is performed on the subsystem computer model, again, to duplicate the low level sine sweep subsystem test (1 *g* input from 20 to 2,000 Hz). Fig. 6.20 displays the harmonic analysis computer results superimposed against the experimental data. The computer results are almost coincident with the experimental data.

The numerical finite element solutions, for both combined and subsystem tests,

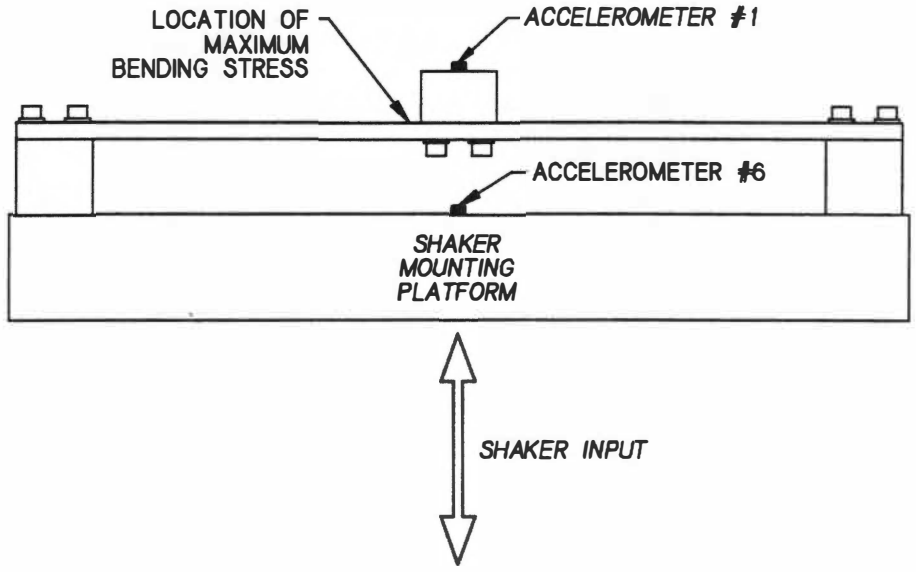

Figure 6.16 Location of accelerometer as instrumented on subsystem structure.

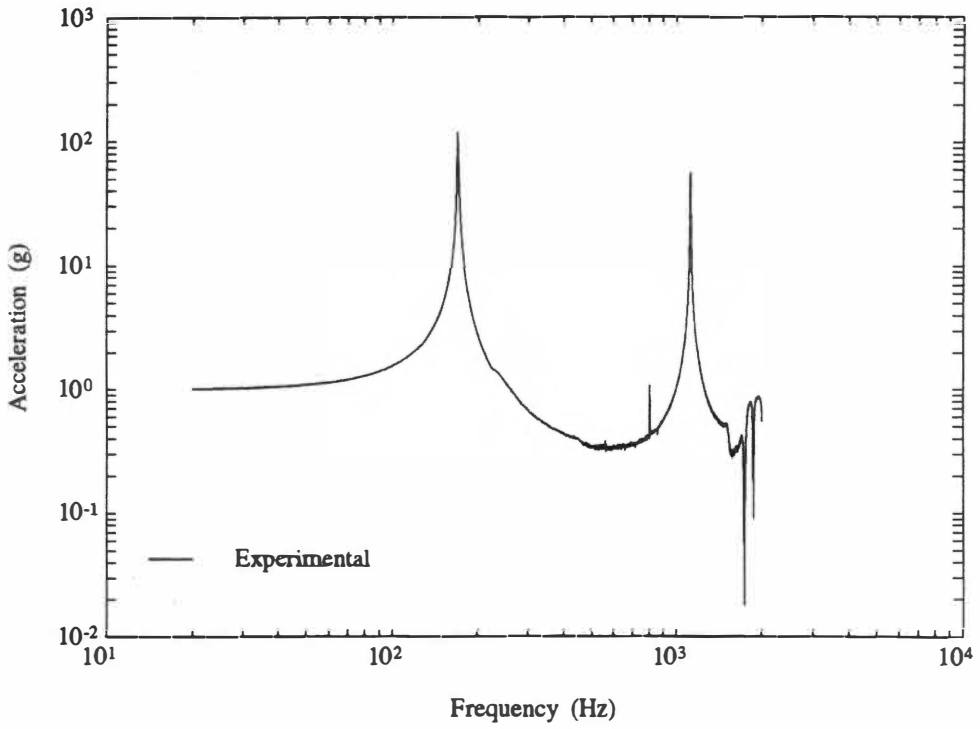

Figure 6.17 Experimental test data results for subsystem structure, accelerometer location #1.

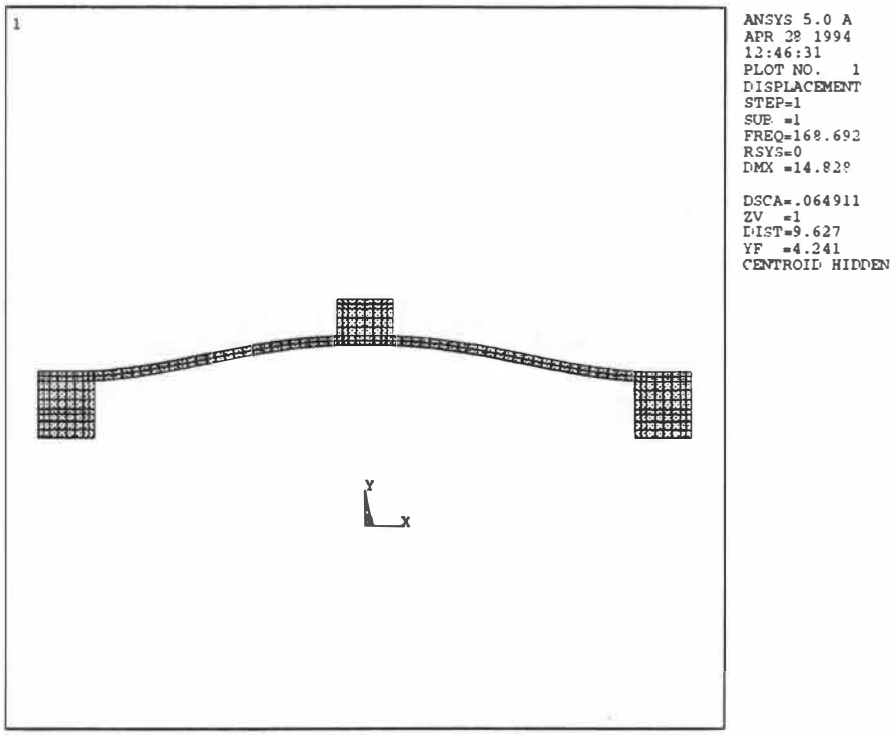

Figure 6.18 First mode shape from finite element modal analysis of the subsystem structure.

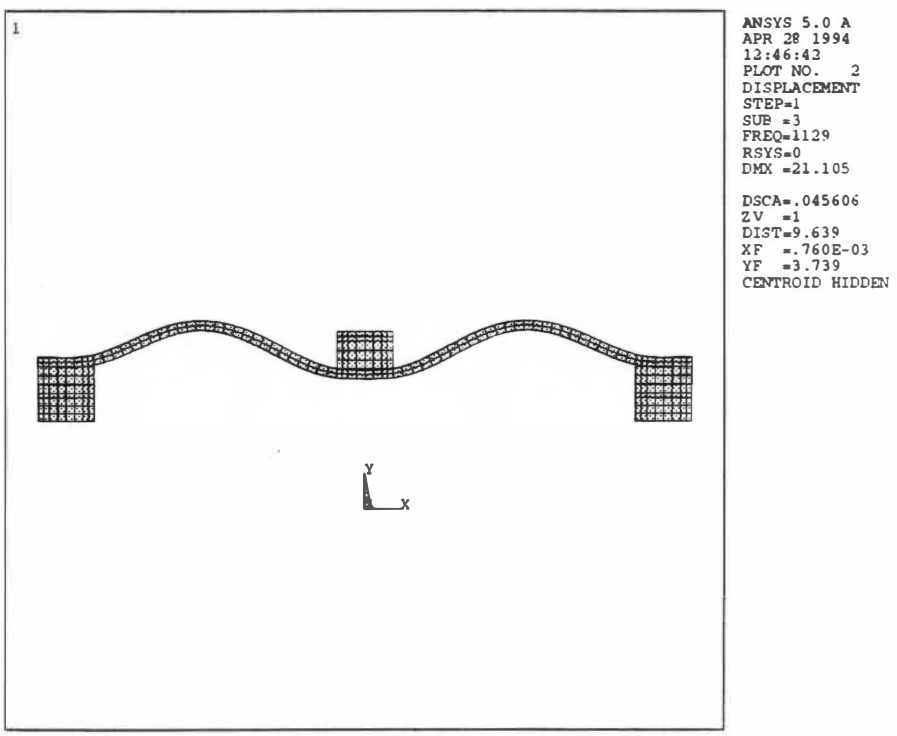

Figure 6.19 Second mode shape from finite element modal analysis of the subsystem structure.

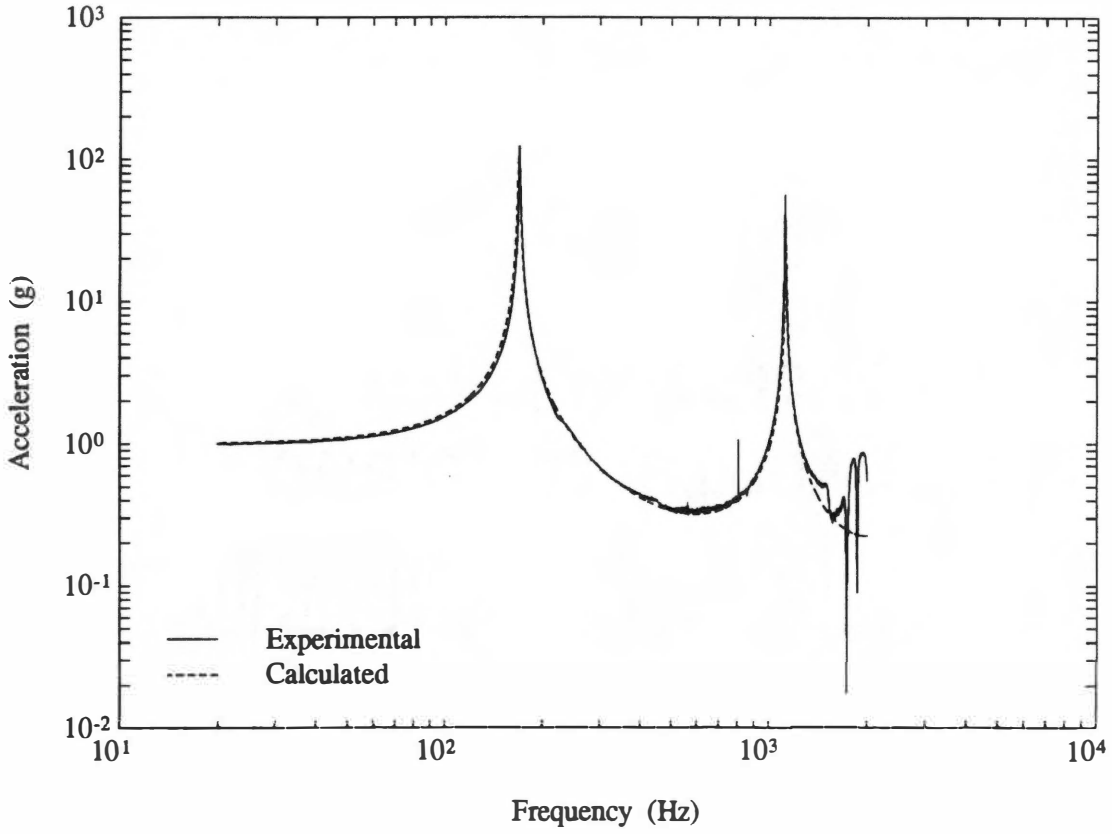

Figure 6.20 Comparison of experimental versus calculated response at accelerometer location #1 for subsystem structure.

compare quite favorably to the experimental data. The benefit of these numerical calculations can now be realized. Implementation of the force-acceleration product method requires subsystem accelerance measurements and implementation of the dual control method requires interface force measurements. Cumulative damage calculations require determination of beam bending stresses for all three methods. These requirements are easily obtained from the finite element analysis results performed above. Since the numerical models are correlated to the experimental results, a high level of accuracy is assured in using the numerical results to compare the three impedance test methods.

Vibration Equivalence

To implement the force-acceleration product method two pieces of information are required: (1) maximum expected interface acceleration levels in the field environment and (2) driving point accelerance function for the subsystem structure. The field acceleration levels are those obtained during the combined structure test (see Fig. 6.5). The peak amplitudes of accelerometer #2 are enveloped and the enveloped function is displayed in Fig. 6.21. Driving point accelerance for the subsystem structure is obtained from the finite element results and the peak amplitudes are enveloped and plotted in Fig. 6.22. The square root of the ratio of driving point accelerance over enveloped accelerance is calculated and this ratio is multiplied by the field acceleration envelope to arrive at the final subsystem test input acceleration (see Fig. 6.23). Maximum subsystem structure bending stress occurs near the center block location (see Fig. 6.16). The subsystem stress FRF using the force-acceleration product technique, superimposed against the combined structure field stress results, is displayed in Fig. 6.24.

Implementation of the dual control technique also requires two pieces of

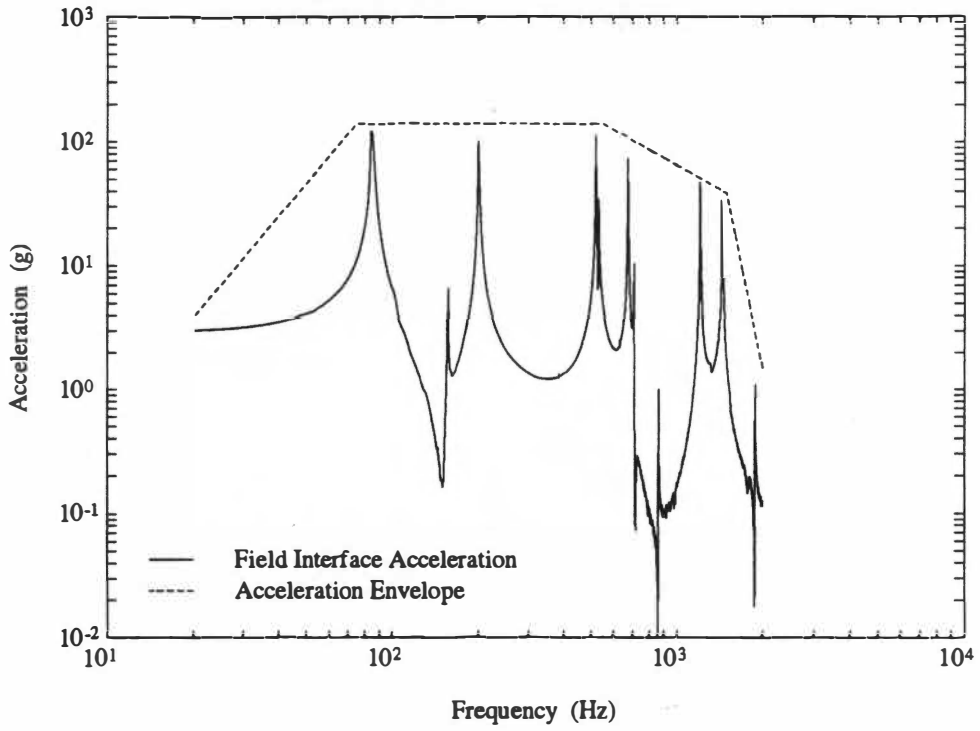

Figure 6.21 Acceleration FRF from interface of combined system with envelope of peak amplitudes of accelerometer #2.

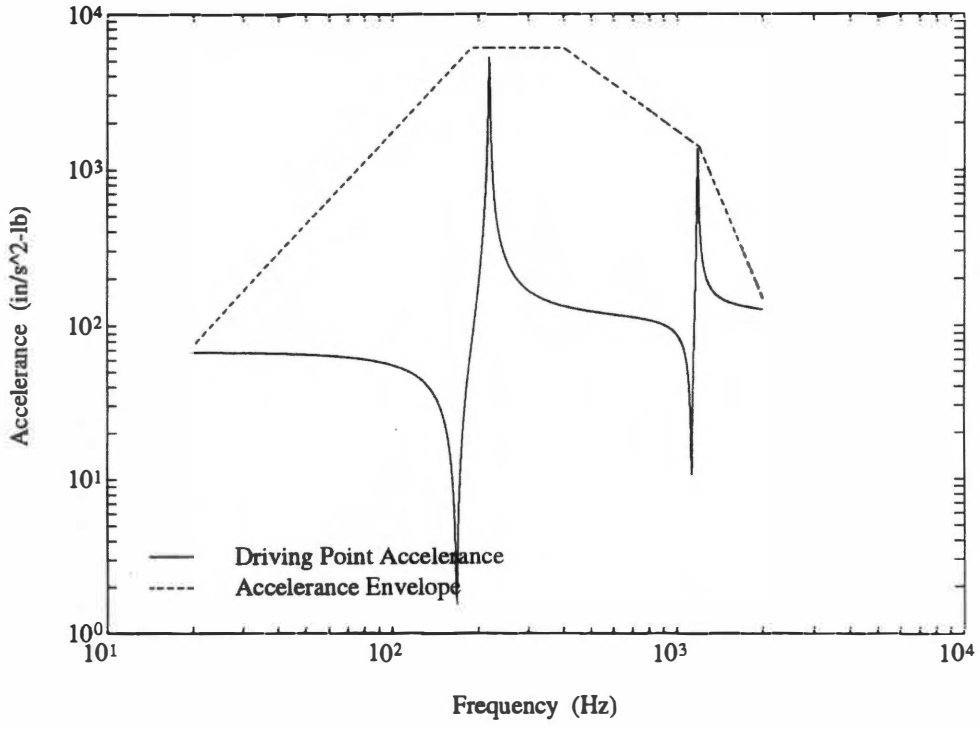

Figure 6.22 Driving point accelerance FRF of subsystem structure with envelope of peak amplitudes.

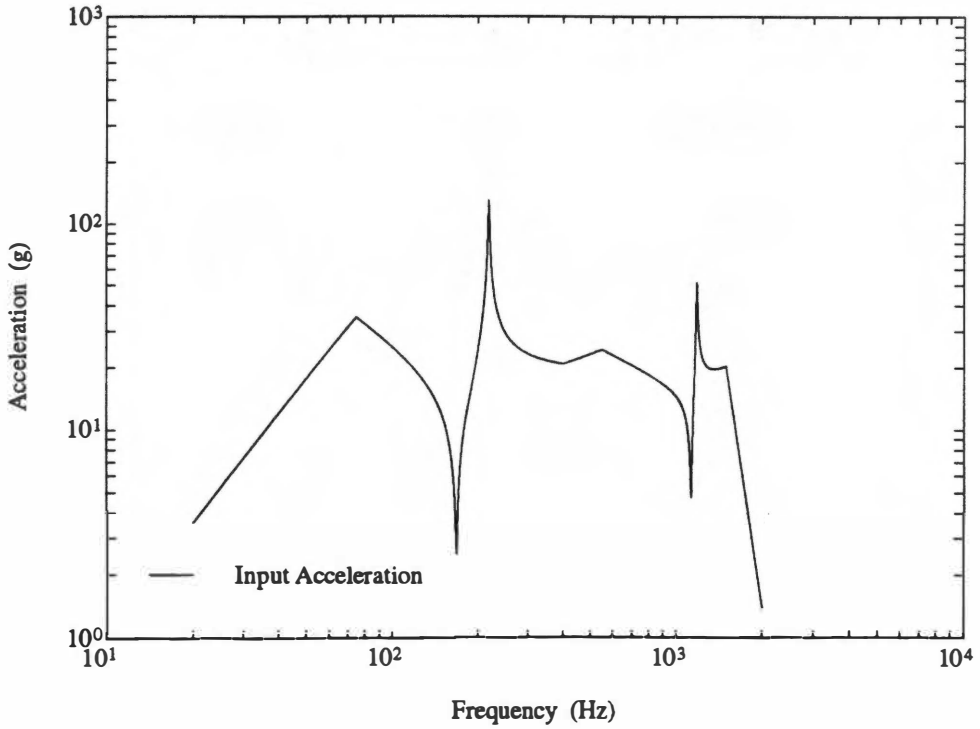

Figure 6.23 Final input acceleration FRF for subsystem test using force-acceleration product method.

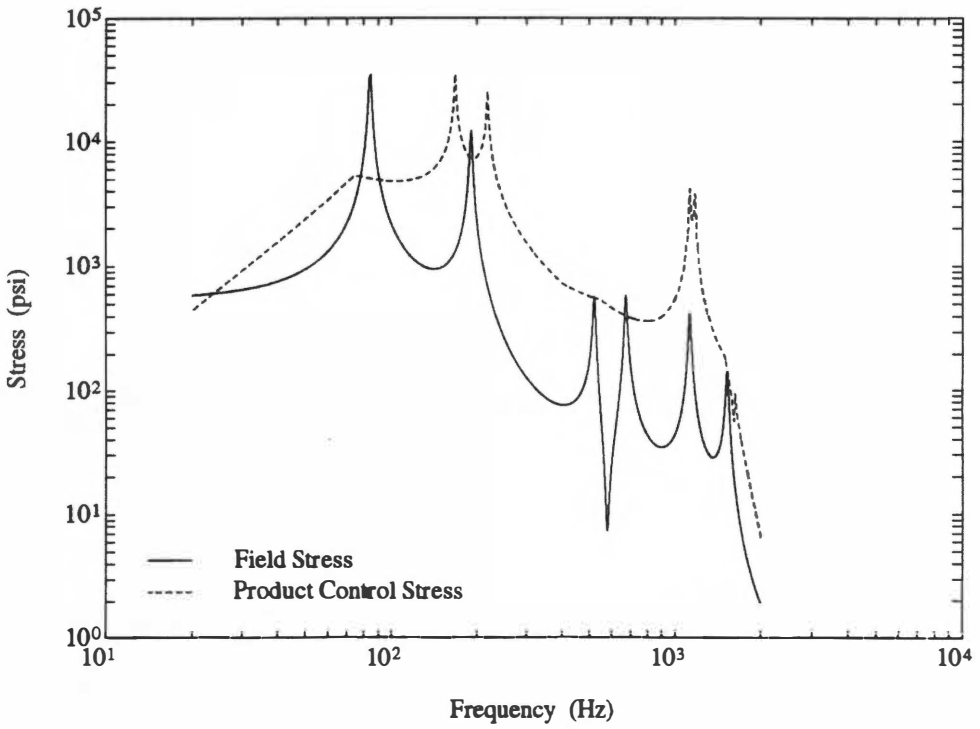

Figure 6.24 Maximum subsystem structure bending stress FRF resulting from force-acceleration product test method.

information: (1) maximum expected interface acceleration levels in the field environment and (2) maximum expected interface force levels in the field environment. The acceleration control spectrum is the same as used in force-product method (Fig. 6.21). The maximum expected interface force levels are taken from the finite element results for the combined system. Fig. 6.25 is a plot of the force control spectrum shown as an envelope of maximum interface force levels from the combined system results. Input control is performed such that neither input force or acceleration exceeds its control spectrum. If at a certain frequency the input force exceeds its maximum level, then the shaker controller reduces the input acceleration until the input force magnitude is less than or equal to the force control spectrum. The resulting final input acceleration into the subsystem structure is shown in Fig. 6.26. The subsystem bending stress FRF using the dual control technique, superimposed against the combined structure field stress results, is displayed in Fig. 6.27.

The transmissibility correction method requires no force or accelerance measurements. All that is required is a transmissibility function for a damage sensitive item within the subsystem. The transmissibility of the top block is used for this purpose and Fig. 6.28 displays this transmissibility function. The input acceleration envelope (Fig. 6.21) is corrected from 20 to 263 Hz, or to the location where the transmissibility curve becomes less than one after the fundamental frequency. The resulting test input acceleration is displayed in Fig. 6.29. The subsystem bending stress FRF using the transmissibility correction method, superimposed against the combined structure field stress results, is displayed in Fig. 6.30.

Comparison of the three impedance methods along with the test results for an

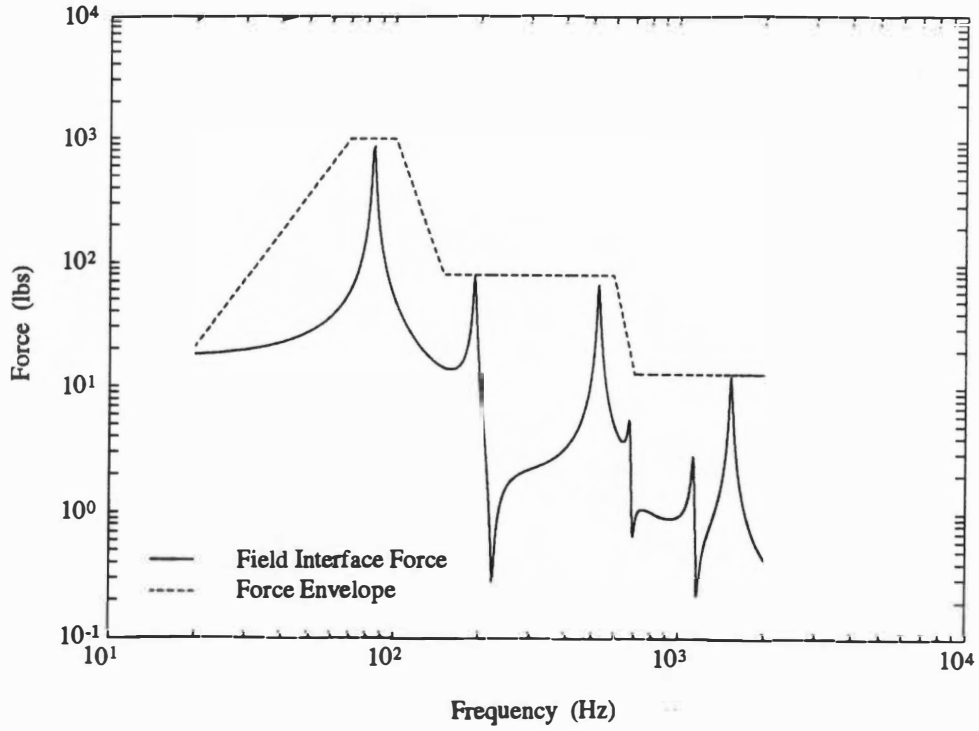

Figure 6.25 Force control spectrum shown as an envelope of peak interface force levels from combined system.

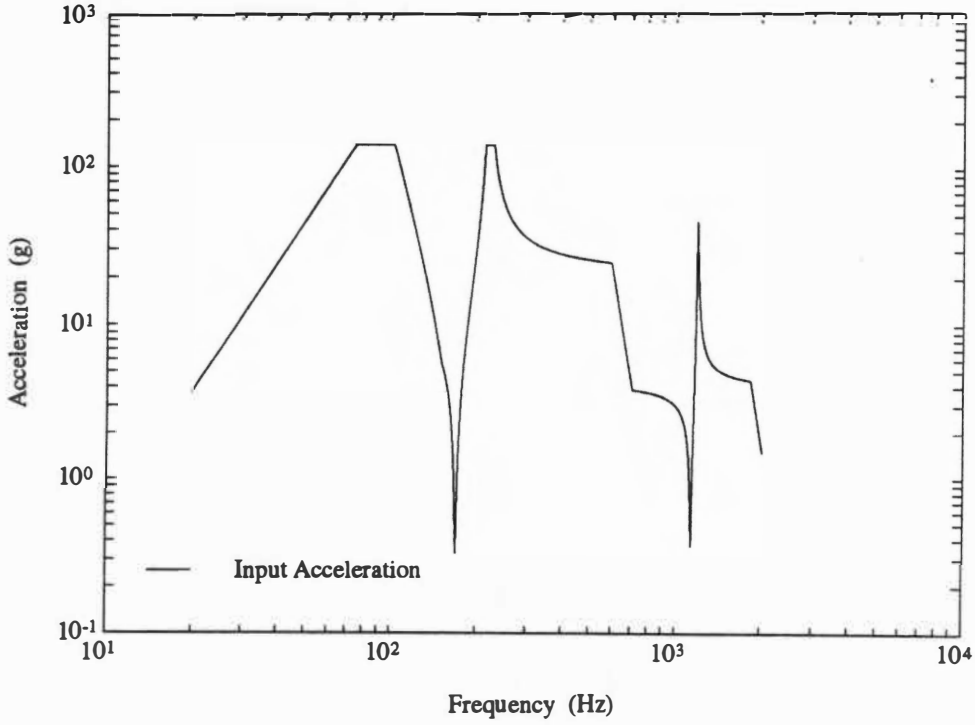

Figure 6.26 Final input acceleration FRF for subsystem test using the dual extremal control test method.

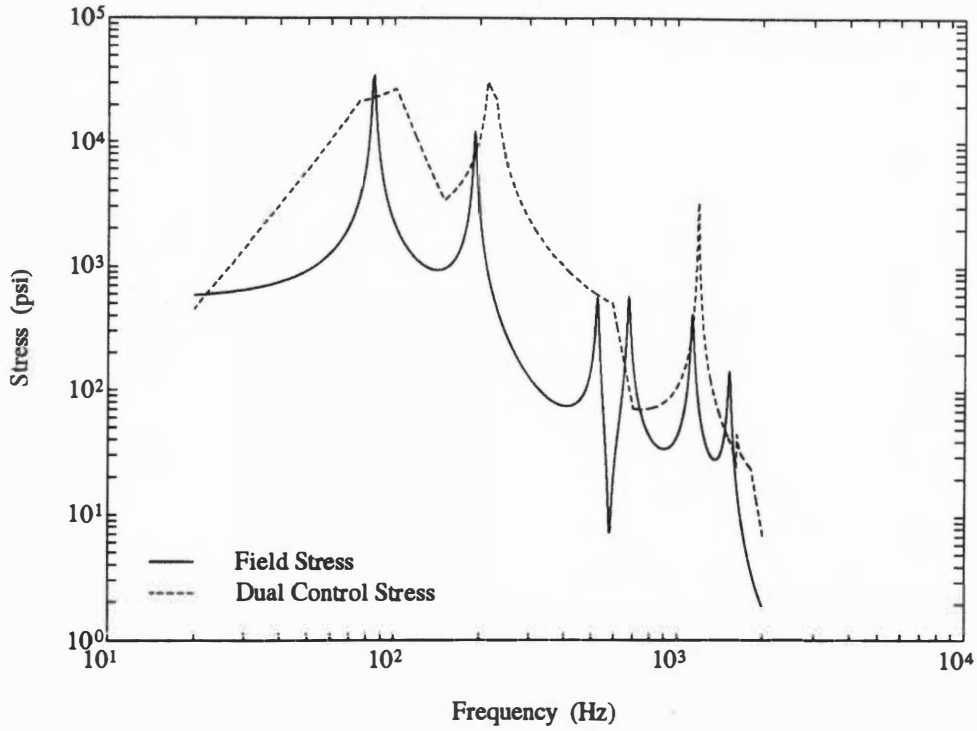

Figure 6.27 **Maximum subsystem structure bending stress FRF resulting from dual extremal control test method.**

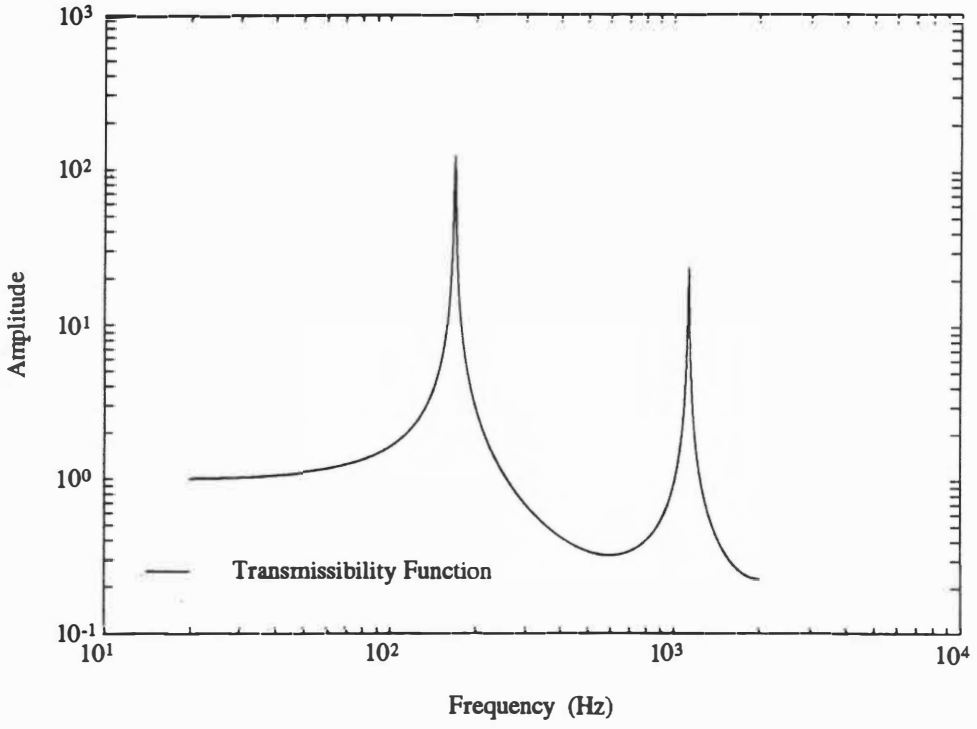

Figure 6.28 **Transmissibility FRF for top block of subsystem structure for use in transmissibility correction test method.**

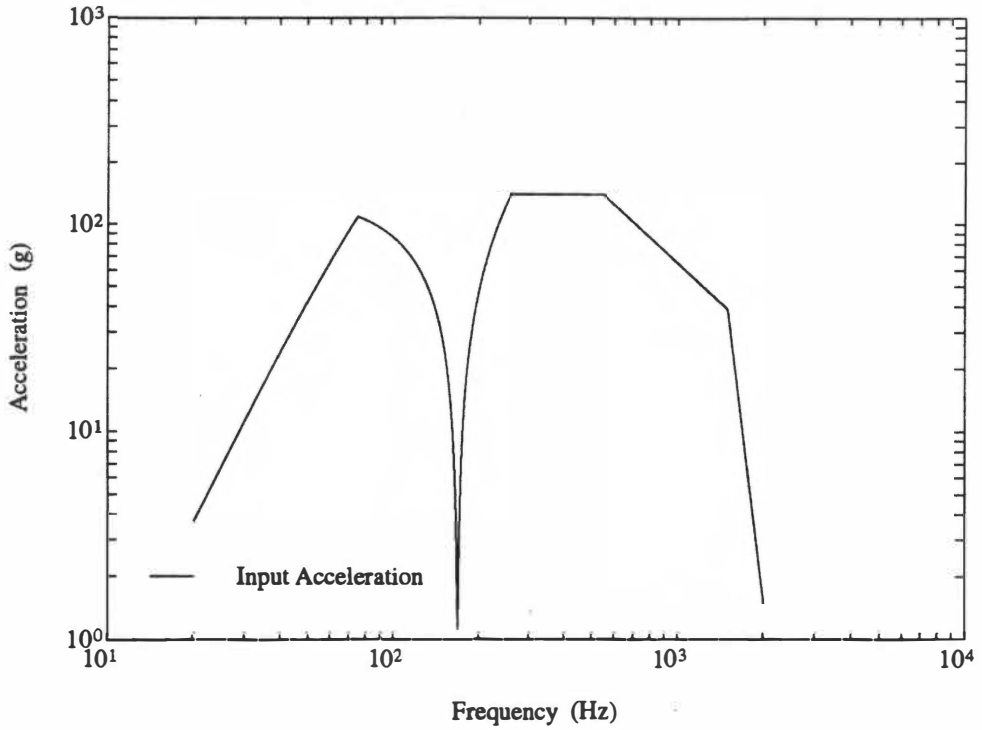

Figure 6.29 Final input acceleration FRF for subsystem test using the transmissibility correction test method.

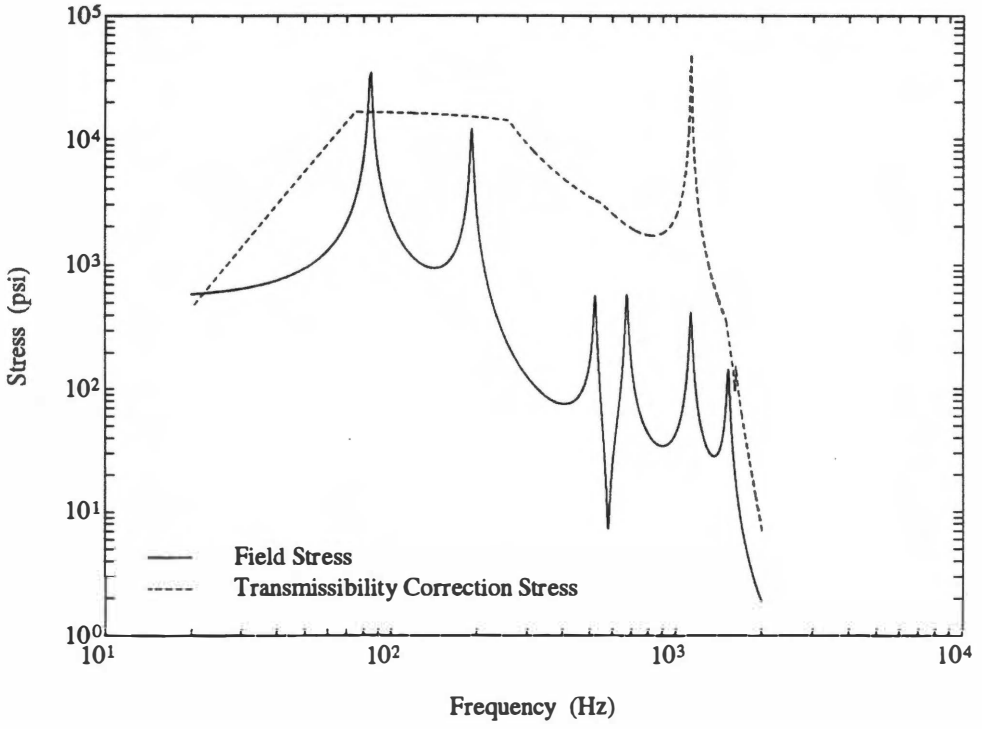

Figure 6.30 Maximum subsystem structure bending stress FRF resulting from transmissibility correction test method.

infinite impedance simulation, superimposed against the field measurements, is depicted in Fig. 6.31. Again, visual determination of the impedance method which most closely simulates the field environment is not obvious from this frequency response plot. However, by application of Miner's cumulative damage criterion (Eq. 6.1) total damage resulting from each method can be easily calculated. The subsystem structure is fabricated from ANSI 1018 carbon steel. The *S-N* curve for this material [31] is used to calculate damage totals. The damage fraction at each frequency point is calculated and then summed across the entire frequency range. The resulting damage totals plus the damage ratio to the field condition are outlined in Table 6.3.

Table 6.3 Cumulative damage totals

Vibration Type	Damage Total	Damage Ratio
Field environment	5.222×10^{-4}	1.00
Force-acceleration product test	5.593×10^{-4}	1.07
Dual extremal control test	8.572×10^{-4}	1.64
Transmissibility correction test	6.959×10^{-2}	133.3
Infinite impedance test	5.911×10^{15}	1.13×10^{19}

The force-acceleration product method most closely simulates the original field vibration environment. The dual extremal control method also closely simulates the original vibration experience. The transmissibility correction method has a damage ratio greater than 100, but the damage total remains less than one. The infinite impedance test method would obviously cause structural failure with a prodigious damage total, magnitudes greater than one.

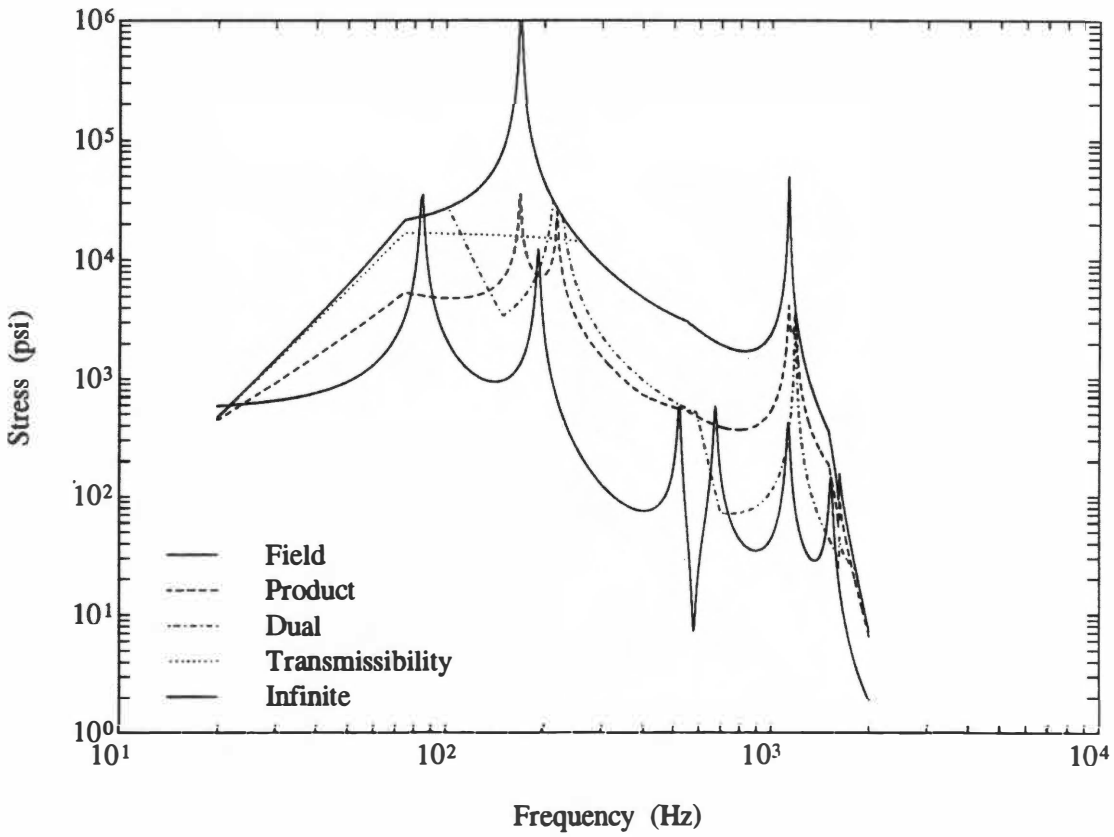

Figure 6.31 Subsystem structure bending stress FRF comparing the three impedance methods vs. field levels and an infinite impedance test.

Advantages and Disadvantages

The force-acceleration product (FAP) method has some advantages over the other two methods. The FAP method can be implemented into existing product line test procedures. Existing field acceleration spectrums are used and the only additional information required is subsystem accelerance functions, which can be experimentally measured for production hardware or calculated for new designs. Interface force measurement and control are not required during the test operation. This implies that existing test equipment can be used with the only supplementary equipment required, being that necessary to measure driving point accelerance.

The major deficiency in the FAP method lies in a theoretical assumption for its use. That is, the FAP method does not fully account for the support foundation impedance function, and therefore this method is not theoretically precise. In Chapter 4 it was shown that the interface acceleration is a function of impedance variables from both equipment and support. However, the results obtained in this investigation indicate that the inaccuracy associated with this assumption is small. The necessity for obtaining driving point accelerance measurements for each unit tested (since production units of the same subsystem will generally not have matching resonances and antiresonances) can also be viewed as a disadvantage.

The dual extremal control (DEC) method appears to be the most flexible and comprehensive of the three impedance methods. The primary advantage of the DEC method is that the unit under test will automatically reduce (notch) the input acceleration level during the test operation. This implies that each production unit will effect its own input spectrum, regardless if the natural frequencies are not the same from unit to unit.

The main disadvantage of the DEC method is the added complexity of the vibration test. Namely, the addition of force transducers into the vibration control loop. This requires extra test equipment and additional fixturing. The need to determine an accurate force control spectrum can also be viewed as a disadvantage.

The transmissibility correction (TC) method is the simplest of the three methods to implement. Force measurement, of any kind, is not required. Acceleration transmissibility functions are obtained using standard test procedures. However, the TC method is the least accurate of the three impedance methods evaluated. Provided that extra equipment and/or extra time is not available, the TC method is still considerably better than an infinite impedance test.

Mechanical impedance methods can be effectively used to account for the dynamic loading interaction between equipment and support during an equipment only vibration test. Their utilization however, is not strictly limited to vibration testing applications alone. These same concepts apply equally well to engineering design problems. Application of mechanical impedance methods to a missile design problem is illustrated in the following chapter.

CHAPTER 7

MISSILE DESIGN PROBLEM

The Standard Missile 2 Block IIIA Medium Range (SM-2 Blk IIIA MR) is the medium range member of the Standard Missile family. SM-2 Blk IIIA is a tactical, guided, surface-to-air missile system. Fig. 7.1 is a diagram of the missile external structure. The five missile sections are secured together to form the missile all-up-round (AUR) assembly. Each section is vibration tested along with major subassemblies contained within each section.

The Standard Missile 2 Block IIIB Medium Range (SM-2 Blk IIIB MR) missile is a new design upgrade, which proposes to add multi-mode target tracking capability. An infrared (IR) seeker head is to be added to the missile system along with the existing radio frequency (RF) seeker head, thus providing the missile with multi-mode detection capability (RF or IR). The proposed IR seeker upgrade is to be physically attached to the missile airframe at missile station (MS) 31.02. The addition of the IR seeker constitutes a major missile modification, and therefore, requires qualification testing. The development of appropriate vibration design loads and test specifications is illustrated for this missile design problem.

What Went Wrong?

An example of how infinite impedance overdesign can lead to serious schedule delays and cost overruns is illustrated with the Standard Missile IR seeker upgrade discussed above. The prime contractor of Standard Missile 2 proceeded into the design

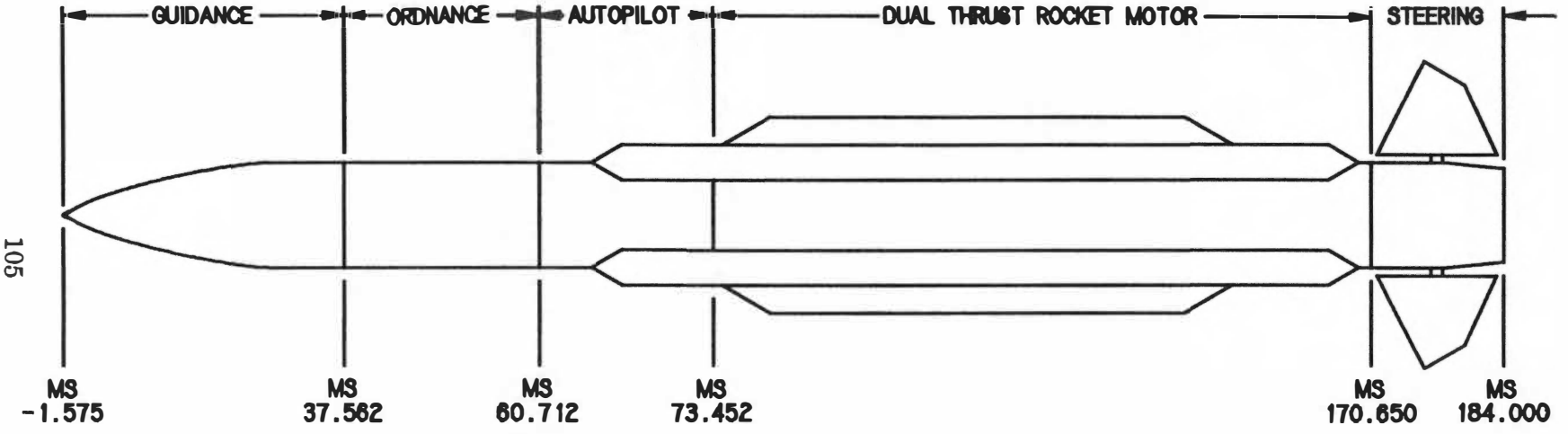

Figure 7.1 Standard Missile 2 Block IIIA all-up-round assembly external configuration.

and development phase using an infinite impedance approach. The field acceleration of the guidance section base (MS 37.562) was enveloped and then used in subsequent dynamic analyses of the new IR seeker configuration to determine seeker head design loads. Not surprisingly, the infinite impedance analysis results indicated very high response levels at the IR seeker location. These design loads were greater than the proposed seeker head could withstand. Based on the infinite impedance design loads, it was decided that the new IR seeker would have to be mounted to the guidance section using a vibration isolator assembly. The vibration isolator added considerable complexity to the mounting scheme and greatly increased the total assembly cost. One, seemingly innocuous, design assumption results in schedule delays, cost increases, and a final product that may not be as good as a hard-mounted IR seeker (no vibration isolator). A review of "what went wrong" is accomplished by performing finite element analysis evaluation of both the vibration isolated and non-isolated design proposals.

Missile Computer Model

A simple approach to modeling the structural dynamic characteristics of tactical missiles consists of developing a non-uniform beam model using a lumped parameter representation for the distributed stiffness and weight. The development of the lumped parameter representation for the airframe weight and stiffness distribution is a straightforward process involving the geometric and material properties of the structure. Accurate representation of mechanical missile joints, however, is a more difficult and less straightforward modeling task. A missile joint constitutes a disturbance in load path which can result in substantial losses in effective stiffness in the vicinity of the joint. Missile joint compliance can be accounted for by representing the joint with equivalent rotational, and longitudinal springs selected to match measured modal response

characteristics.

A missile can be described analytically as a non-uniform elastic beam (the main airframe beam) to which various appendages are attached. The appendages represent the internal equipment packages. Joint local deformation characteristics can be simulated by placing local springs at stations where joints occur. The main beam is represented as a series of lumped masses and inertias connected by weightless beam elements. The beam elements represent the average stiffness properties between the mass stations. The appendages are represented in the same manner as the main beam and attachment of an appendage to the main beam is accomplished with local springs representing attachment compliances.

The amount of local joint compliance present in a particular missile joint is primarily a function of joint design and geometry. The initial establishment of joint compliance values for modeling the SM-2 Blk IIIB MR design problem are taken from an industry design guideline for missile joint properties [32]. The final joint compliance values are "tuned" to match AUR modal survey data for SM-2 BlK II MR (modal survey data was not available for the Block IIIA AUR configuration).

Finite Element Analysis

The ANSYS finite element computer program is used to generate the AUR beam model and perform the dynamic analyses. Average stiffness, mass, and inertia values are calculated from the SM-2 Blk IIIA MR design drawing technical data package for both missile airframe and appendage sections. Table C.1 (located in Appendix C) lists the SM-2 Blk IIIA MR structural dynamic properties for use in the finite element computer program.

Modal analysis is performed repeatedly, iterating on the joint compliance values, so as to match AUR model survey test data [33]. A comparison of experimental versus calculated natural frequencies for SM-2 AUR structure is as follows:

Table 7.1 Experimental vs. calculated natural frequencies, SM-2 AUR

Experimental (Hz)	Calculated (Hz)	Difference (%)
f_1 = 44	f_1 = 43	2.27
f_2 = 95	f_2 = 94	1.05
f_3 = 116	f_3 = 115	0.86
f_4 = 185	f_4 = 206	11.35
f_5 = 275	f_5 = 273	0.73
f_6 = 318	f_6 = 344	8.18
f_7 = N/A	f_7 = 479	N/A
f_8 = N/A	f_8 = 483	N/A
f_9 = N/A	f_9 = 757	N/A
f_{10} = N/A	f_{10} = 812	N/A

The higher order modes are not determined in a standard ground modal survey and therefore, correlation to the experimental values is not confirmed for natural frequencies greater than 350 Hz.

Random vibration is the primary excitation driving the in-flight missile structure. For this design evaluation, it is assumed that the dual thrust rocket motor is the random vibration source. A flat 0.01 g^2/Hz from 20 to 600 Hz, rolling off to 0.001 g^2/Hz at 1,000 Hz is applied to the missile airframe structure, in the longitudinal axis. Acceleration response at the base of the guidance section joint and at the IR seeker gimbal location is recorded and used in the design evaluations. The dynamic characteristics for the vibration

isolated and hard-mounted IR seeker proposals are summarized in Table 7.2.

Table 7.2 Dynamic characteristics of hard-mounted and isolated IR seeker proposals

Seeker Mounting Proposal	IR Seeker Mounting Assembly					IR Seeker Gimbal Assembly				
	Frequency (Hz)		Quality Factor		Mass (lb)	Frequency (Hz)		Quality Factor		Mass (lb)
	Long	Radial	Long	Radial		Long	Radial	Long	Radial	
Isolated	245	245	4	4	0.58	700	550	17	17	0.166
Non-Isolated	1,100	1,100	25	25	0.50	700	550	17	17	0.166

Modification to the AUR computer model is made to add the IR seeker head assembly at missile station 31.02. The hard-mounted case study is evaluated first.

Fig. 7.2 displays the rocket motor input spectrum (applied at MS 165.0), the guidance section base response power spectral density (PSD), and the IR seeker head response PSD. These represent hypothetical field measurements. Fig. 7.3 shows the guidance section base PSD with the spectral peaks enveloped to form the acceleration control spectrum. Fig. 7.4 displays the interface force levels acting between the guidance and ordnance sections, with the peak amplitudes enveloped to form the force control spectrum. The guidance section is then detached from the missile AUR (at MS 37.562) and secured to a vibration shaker with fixtures. The vibration test is carried out using both the infinite impedance and dual extremal control test methods.

Fig. 7.5 compares the two input acceleration functions. Notice that the dual control input spectrum displays acceleration notches at frequencies where the vibration test is force controlled (fixed base natural frequencies of guidance section). Fig. 7.6 compares the guidance section test results for both the infinite impedance and dual control

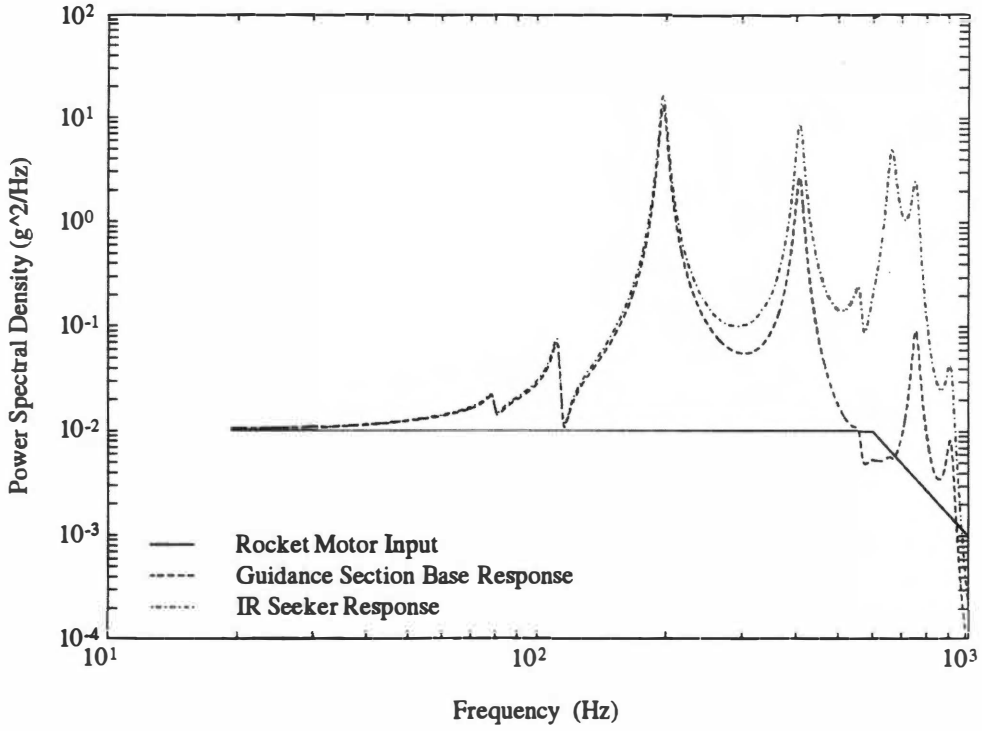

Figure 7.2 **AUR field measurements resulting from rocket motor random vibration input in the longitudinal axis, hard-mounted IR seeker.**

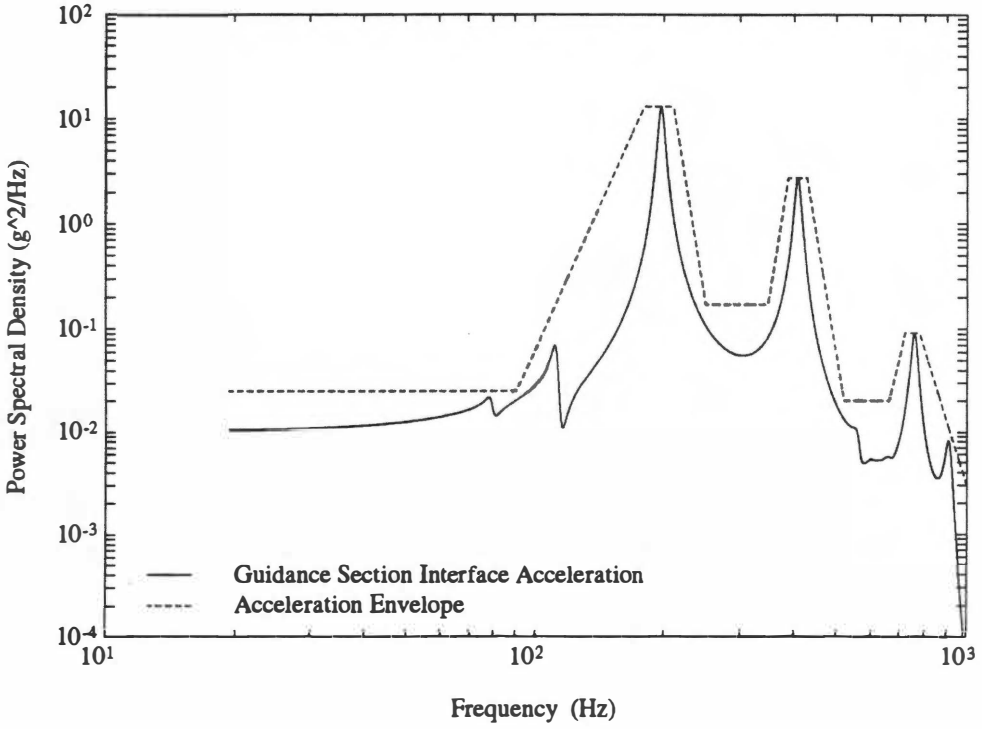

Figure 7.3 **Acceleration control spectrum shown as an envelope of peak guidance section base interface levels, hard-mounted IR seeker.**

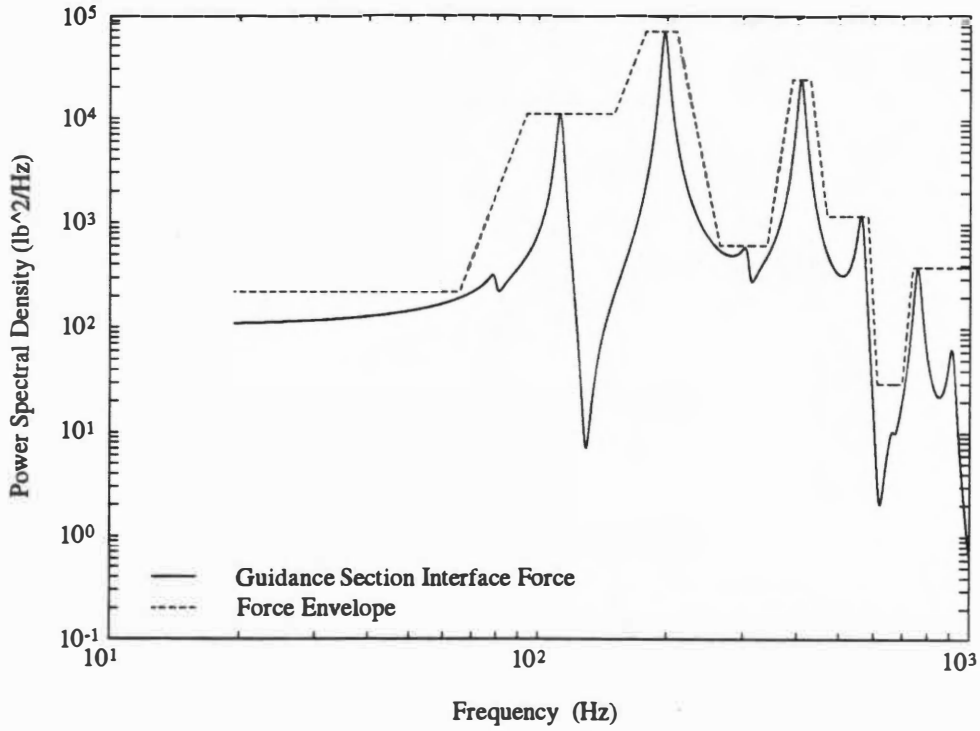

Figure 7.4 Force control spectrum shown as an envelope of peak guidance section base interface levels, hard-mounted IR seeker.

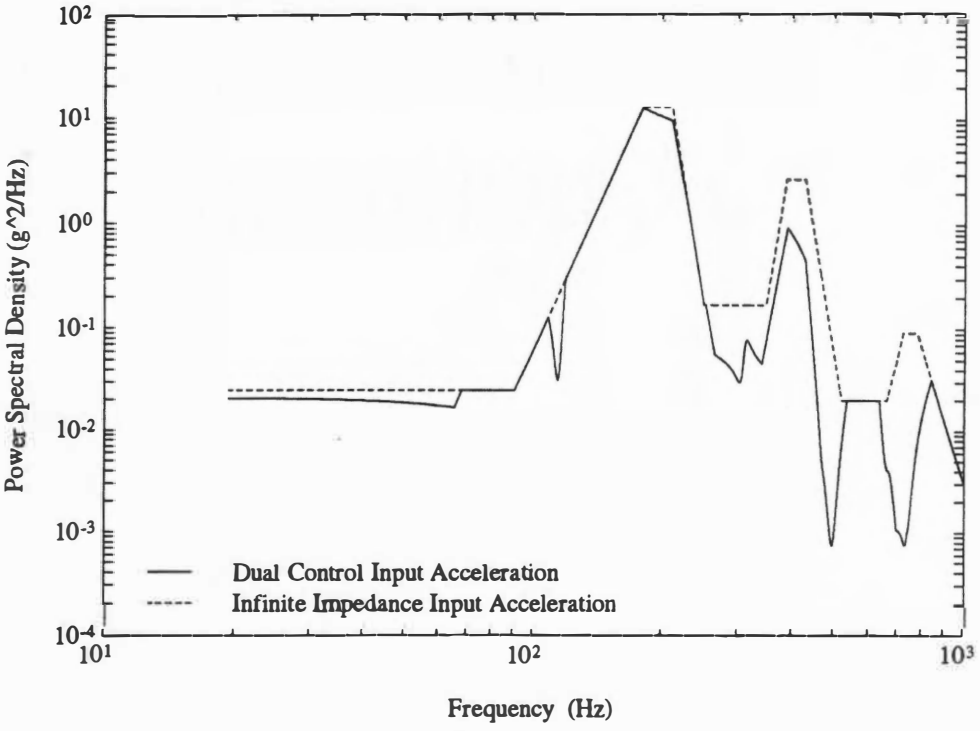

Figure 7.5 Input acceleration spectrum comparing dual control against infinite impedance method for longitudinal axis, hard-mounted IR seeker.

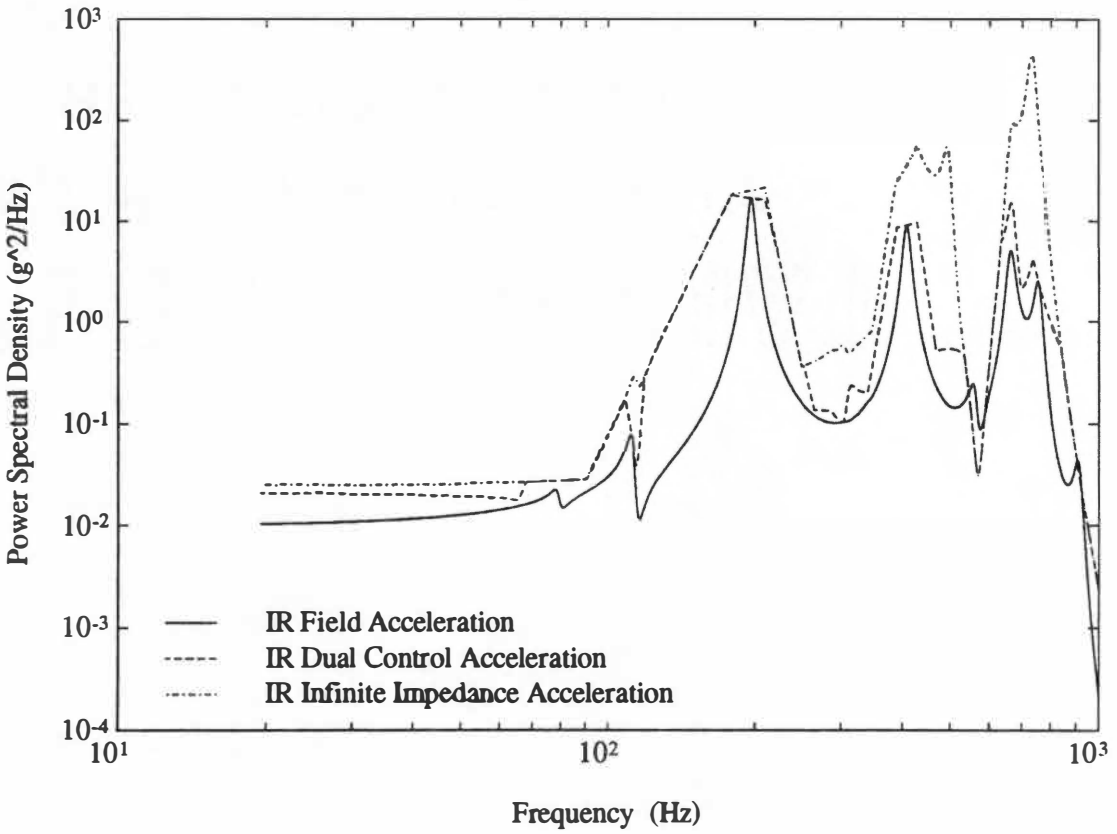

Figure 7.6 Guidance section test results for dual control and infinite impedance test methods, superimposed against field measurements, hard-mounted IR seeker.

methods, superimposed against the AUR field measurements. As can be observed, the infinite impedance method does indicate high response levels at the IR seeker location, just as was reported by the prime contractor. However, these high levels are a test artifact and do not occur in the field.

The analyses are re-run to evaluate the prime contractor's vibration isolated seeker mounting configuration. The finite element model is revised to reflect the dynamic characteristics of the vibration isolated IR seeker head assembly. Figs. 7.7 through 7.11 display the vibration isolated configuration frequency response results.

Results Comparison

The power spectral density response plots can be integrated to give the mean square response, from which the 1σ standard deviation (root-mean-square, RMS) response is obtained. The statistical average frequency is defined as:

$$f_{SA} = \sqrt{\frac{\int f^2 S(df)}{\int S(df)}} \tag{7.1}$$

which is an indicator of where the dominant resonant frequencies reside. Together, these two response quantities provide insight into the severity of the random vibration environment [14]. Comparing these two quantities for both seeker mounting proposals uncovers exactly "what went wrong" and why. Table 7.3 lists the RMS and statistical average frequency values for both IR seeker mounting proposals.

The IR seeker RMS acceleration value for the hard-mounted, infinite impedance guidance section test indicates high response levels (162 *g*'s RMS), at an average

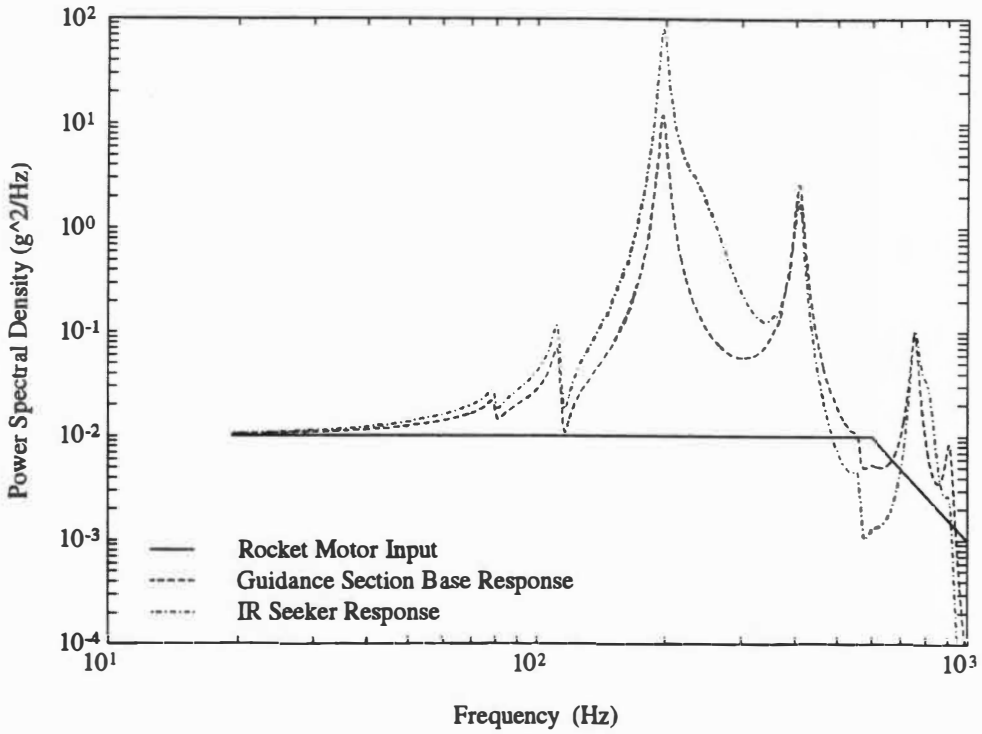

Figure 7.7 AUR field measurements resulting from rocket motor random vibration input in the longitudinal axis, isolated IR seeker.

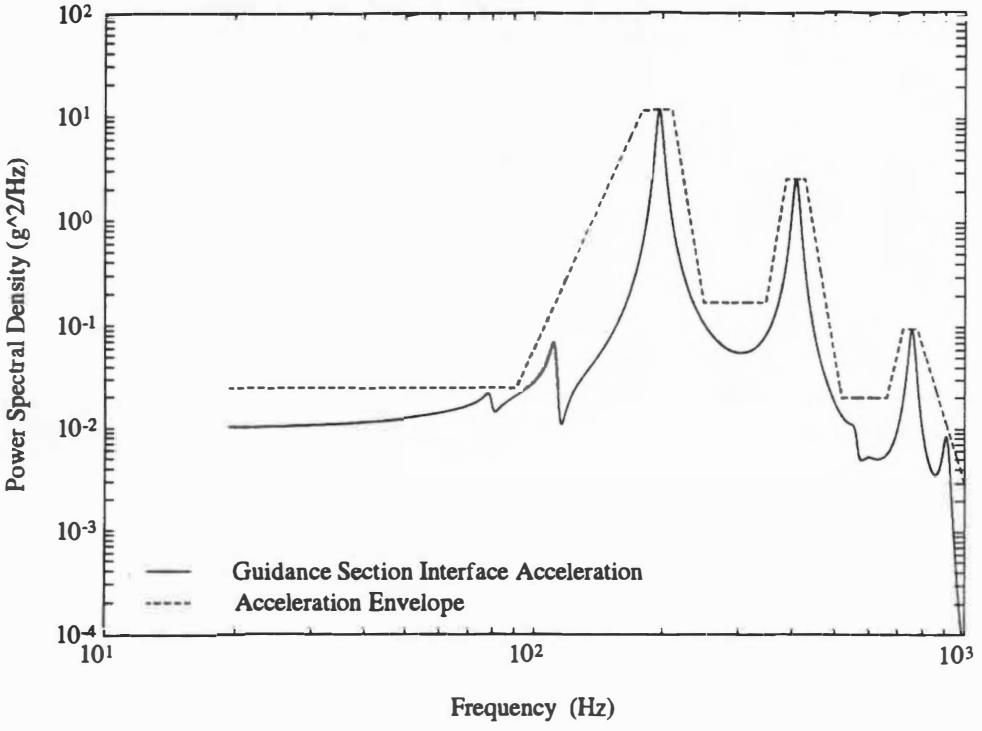

Figure 7.8 Acceleration control spectrum shown as an envelope of peak guidance section base interface levels, isolated IR seeker.

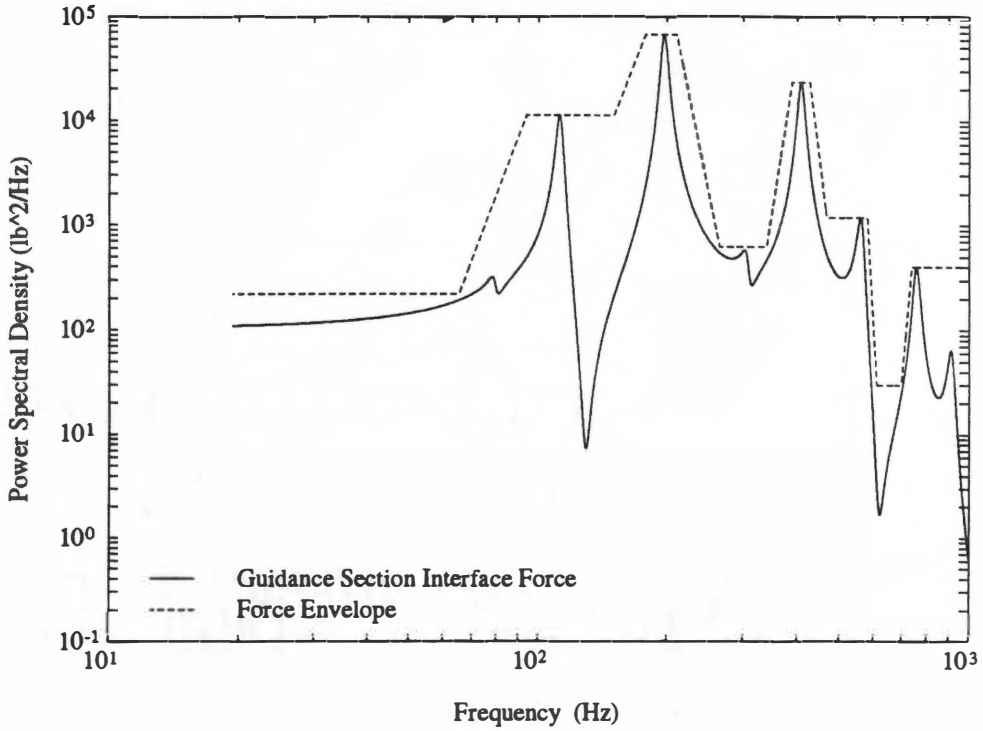

Figure 7.9 Force control spectrum shown as an envelope of peak guidance section base interface levels, isolated IR seeker.

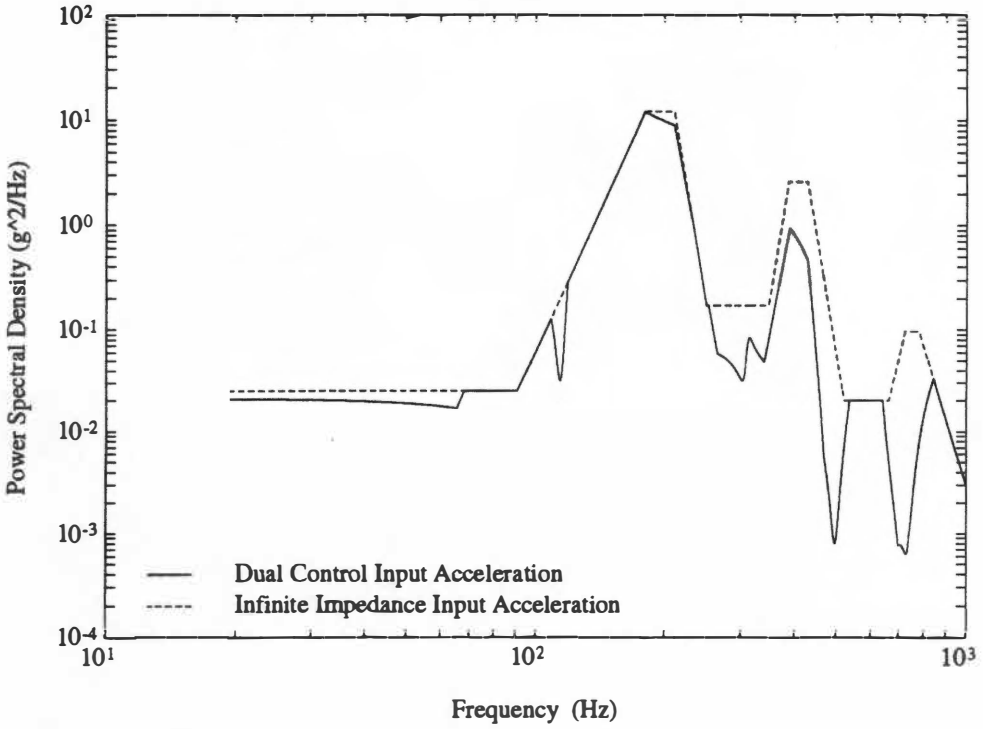

Figure 7.10 Input acceleration spectrum comparing dual control against infinite impedance method for longitudinal axis, isolated IR seeker.

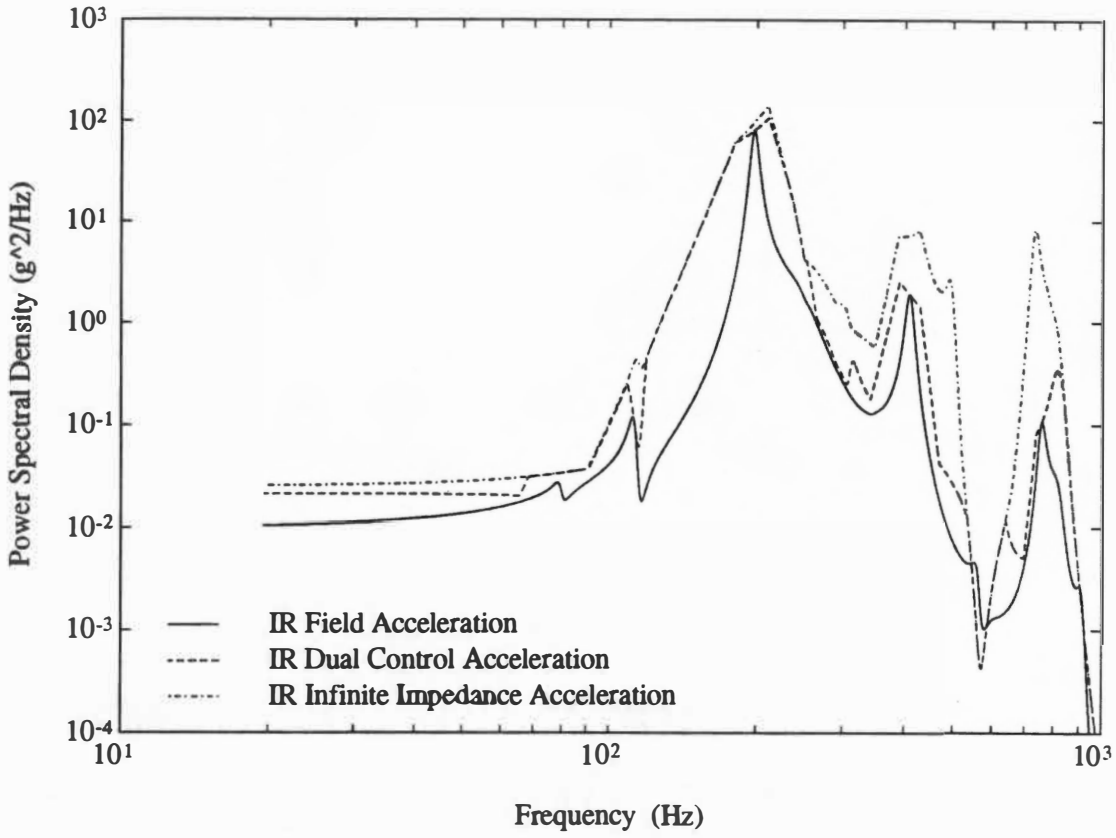

Figure 7.11 Guidance section test results for dual control and infinite impedance test methods, superimposed against field measurements, isolated IR seeker.

Table 7.3 Results comparison of hard-mounted and vibration isolated seeker proposals

Parameter	Hard-Mounted IR Seeker		Vibration Isolated IR Seeker	
	1σ RMS (g)	Avg f_{SA} (Hz)	1σ RMS (g)	Avg f_{SA} (Hz)
AUR Level Field Measurements				
Rocket motor input PSD	2.69	454	2.69	454
Guidance section base response	15.35	297	15.11	299
IR seeker head gimbal response	27.68	519	33.94	224
Guidance Section Infinite Impedance Test				
Input acceleration envelope	31.10	269	30.19	273
IR seeker head gimbal response	161.83	664	80.44	293
Guidance Section Dual Control Test				
Input acceleration function	26.89	219	26.01	222
IR seeker head gimbal response	50.12	478	69.62	217

frequency around 664 Hz. The IR gimbal resonance is at 700 Hz and thus the majority of the power, during the infinite impedance test, directly excites the IR gimbal's fixed base natural frequency. This high level of IR seeker response does not occur during flight (28 vs 162 *g*'s RMS). The decision to vibration isolate at 240 Hz seems to be a bad choice. Even though the infinite impedance seeker response levels are reduced (with the isolated seeker) to a tolerable test level (from 162 to 80 *g*'s RMS), the AUR field measurements for the IR seeker indicate a higher response with the vibration isolator than without it (34 vs 28 *g*'s RMS). This results from the close proximity of the missile's fundamental frequency to the isolation frequency. The statistical average frequency for the AUR guidance section base is at 297 Hz. The isolation frequency is at 245 Hz, close enough to participate in the fundamental missile response.

The dual control results indicate no problem with the hard-mounted IR seeker assembly. The seeker head resonances are considerably greater than the missile's fundamental frequency and therefore modal coupling is not present. Guidance section testing using dual control yields comparable RMS and average frequency values to the field measurements (50 vs 28 *g*'s RMS and 478 vs 519 Hz). The dual control test for the vibration isolated seeker has an increased RMS value over the dual control of the hard-mounted proposal (70 vs 50 *g*'s RMS). Again, this arises because of the coupling of isolation and missile frequencies.

This design evaluation conclusively demonstrates the problems that can result with an infinite impedance vibration approach. The addition of a costly, complicated, mounting device is neither necessary nor beneficial for reducing flight level vibration. In actuality, the IR seeker flight level vibration will increase with the presence of a vibration isolator.

Impedance methods applied to a design problem are of no advantage if an infinite impedance qualification test is a requirement. When an infinite impedance test is required, the design is governed by having to pass an unrealistic vibration test, and not based on the actual field environment. The advantages of mechanical impedance methods can only be realized when they are implemented into the vibration test facility. Implementation of mechanical impedance test methods into the test laboratory is the subject of the next chapter.

CHAPTER 8

IMPLEMENTATION, PROCEDURE, AND CONCLUSION

Up to this point, much effort has been placed on the development, justification, and demonstration of mechanical impedance simulation methods. The implementation of these methods, in a vibration test facility, is perhaps the most important aspect of the total problem. The inadequate testing technology that existed some 25 years ago was the predominant reason why impedance test methods were abandoned at that time. The advancements in control technology and instrumentation have now rendered mechanical impedance testing fully achievable.

As previously stated, implementation of the force-acceleration product and transmissibility correction methods do not require additional control techniques and therefore description of their implementation is not necessary. The dual extremal control method requires modification to the standard control scheme and discussion of its implementation is provided below.

Dual Extremal Control Vibration Controller

In the dual extremal control approach, the shaker control system compares several measurement channels with appropriate reference spectra and adjusts the shaker drive until one channel is equal to the reference and the other channels are equal to or less than their references. When one channel is force and the other is acceleration, the dual extremal control method is automatically implemented. Unfortunately, most conventional shaker controllers currently provide for only one reference spectrum.

Fig. 8.1 shows the flow diagram which can be used to implement dual extremal control with conventional test equipment [23]. The payload test unit is mounted to a rigid fixture. Four piezoelectric force transducers are sandwiched between the fixture plate and the shaker table platform. The outputs of the four force transducers in the test axis direction are summed to provide total force. The summed transducer output is attenuated by a charge amplifier to accommodate the high sensitivity force transducers. The output of the charge amplifier is sent to a real-time spectrum analyzer, and then to the shake controller for force limiting.

Channels 1 and 2 are redundant control accelerometers in the shake direction, and channel 3 is the force transducer signal. S1 and S2 are the control accelerometer charge amplifier sensitivities in volts/*g*, Sf is the force transducer charge amplifier sensitivity in volts/lb, and S3 is the pseudo-accelerometer sensitivity in volts/*g* input to channel 3 of the controller. The one-third octave spectrum shaping filter gain settings are calculated from S3, Sf, and the acceleration A_S and force F_S specifications as shown in Fig. 8.1. The one-third octave shaping filter network acts as the second reference spectrum. The newer, faster vibration test controllers incorporate the capability of specifying separate references for each control channel. With this feature, the one-third octave filter is not necessary, as both acceleration and force control reference spectrums are directly input into the vibration controller.

Dual Control Force Spectrum

Perhaps the major difficulty in the implementation of dual control vibration testing is the definition of an appropriate force limit. The force control spectrum has been defined as an envelope of maximum interface force levels, acting between an equipment item and

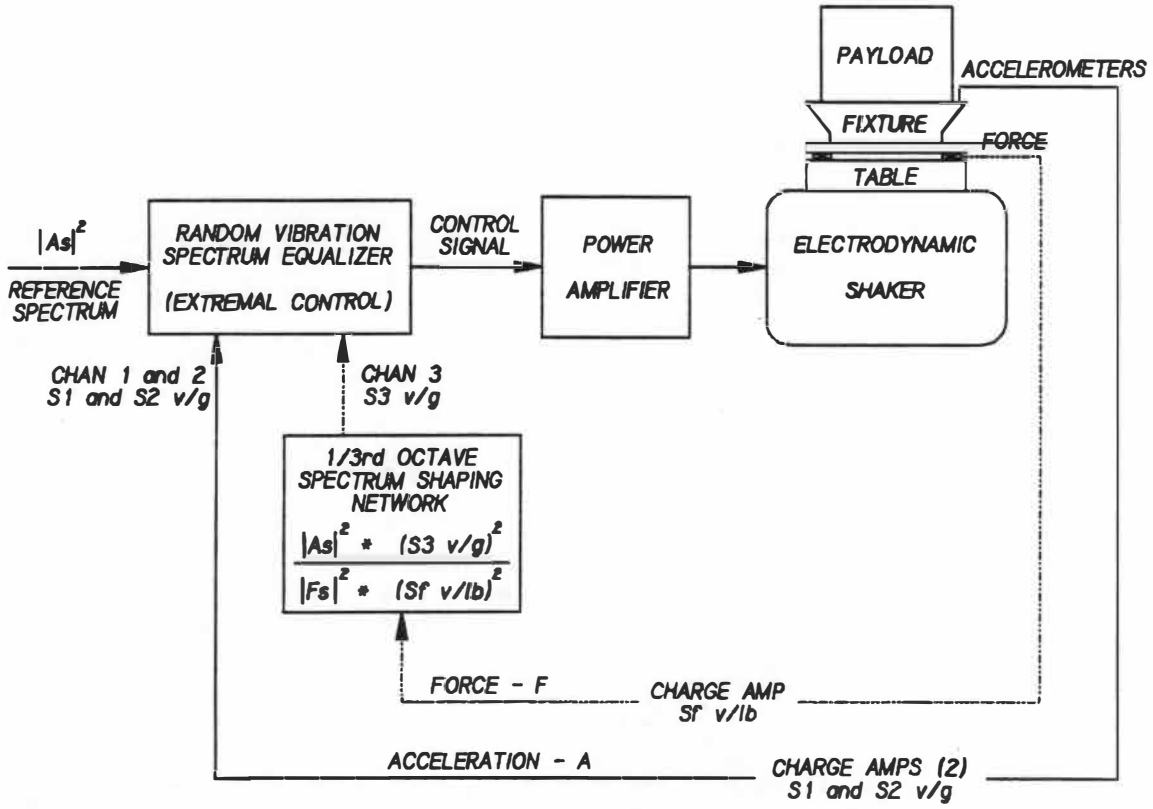

Figure 8.1 Diagram for dual extremal control of acceleration and force using conventional test equipment.

its support, in the field vibration environment. The force control spectrums developed throughout this thesis resulted from the assumption that the field vibration source, for the combined system, has a known magnitude and known application point. This allowed for the interface force to be directly extracted from the simulation results. During a supersonic guided missile flight this assumption is not usually valid. The random vibration source is a complex combination of rocket motor noise, aerodynamic turbulence, asymmetric vortex shedding, and aeroelastic coupling effects. In this case the vibration source has an unknown magnitude and application point.

Ideally, the interface force levels should be determined by inserting force transducers, between equipment and support points, and record the force magnitude that occurs during flight. Unfortunately, the typical missile assembly has no room to facilitate the added height and width associated with the force instruments. How is an accurate force control spectrum developed when the vibration source is unknown? Several methods have been successfully used to accomplish this task [25, 27, 34-35].

All of these methods calculate the force limit spectrum from the interface acceleration specification derived in the conventional manner. One option is to multiply the acceleration specification by the magnitude squared (for random vibration) of the vibration source (equipment support) effective mass. This option (called the source impedance method) is claimed to yield the correct result in the high frequency regime where both the equipment and support have many resonance frequencies [24]. Another option is to multiply the acceleration specification by the vibration load (equipment) effective mass. Both of these methods do not fully account for the combined contributions of the equipment and support impedance functions, as was derived in Chapter 4.

A method which accounts for both contributions has been successfully applied in flight configuration qualification testing at the Jet Propulsion Laboratory [34-35]. This method has been named the two-degree-of-freedom-system (2-DOFS) method, since it uses results obtained from a 2-DOF parametric study (as was performed in Chapter 3). This method requires the effective mass (or accelerance) frequency response functions for both the vibration source and load. These impedance functions are determined by laboratory measurements or by using the finite element method. An effective mass ratio is calculated as the mean load to mean source effective mass. From the effective mass ratio, the ratio of mean-square absolute acceleration of load mass to mean-square free acceleration of source mass is computed from 2-DOF parametric results. The force limit spectrum is then taken as the product of the input acceleration spectrum times the square of the mean effective mass of the load times the calculated 2-DOF mean-square response ratio. This technique can be quickly illustrated by using the following table:

Table 8.1 Typical data used to calculate force control specification

Frequency (Hz)	50	100	200	400	800
Acceleration specification (g^2/Hz)	.023	.07	.09	.09	.04
Mean source effective mass (lbs)	800	350	150	70	30
Mean load effective mass (lbs)	200	126	63	32	16
Ratio of load to source effective mass	0.25	0.36	0.42	0.46	0.53
2-DOF mean-square response ratio	5	4	3.7	3.5	3
Force specification (lbs^2/Hz)	4600	4445	1322	323	31

Line one lists the octave band center frequencies at which the force spectrum values are calculated. Line two lists acceleration spectral values from the interface acceleration specification. Line three gives the vibration source mean effective weight at the center band frequencies. The mean effective weight is defined as a smooth curve

(arithmatic average) passing through the mean of the spectral peaks and valleys, ignoring the details of the effective mass frequency response function. Line four gives the mean effective mass of the vibration load. Line five is the ratio of the mean load to mean source effective mass. Line six gives the ratio of the mean-square response to that of the input for a 2-DOF system (see Fig 8.2). Finally, the octave band values of the force limit specification are given in line 7, where line 7 = (line 2) × (line 4)^2 × (line 6).

The calculation of the force control specification is not very sensitive to the assumed mass ratios or the assumed damping values. A conservatively assumed mass ratio (smallest credible value) will assure a conservative test. The mean-square response ratio increases monotonically with a decreasing mass ratio (see Fig. 8.2). Increasing the damping also monotonically increases the mean-square response ratio. A conservative test will result from overestimating the damping factor.

The Procedure

A systematic step-by-step procedure is suggested to help implement mechanical impedance vibration simulation methods for a typical guided missile system:

1.) Establish a well developed missile finite element computer model. The missile model generated in Chapter 7 is a relatively crude beam representation (180 degrees-of-freedom). A missile model can be generated to represent much greater detail. The newer high-speed computers are capable of solving finite element problems that contain over a hundred thousand degrees-of-freedom. With this capability, detailed 3-dimensional missile section models can be integrated with beam representations to

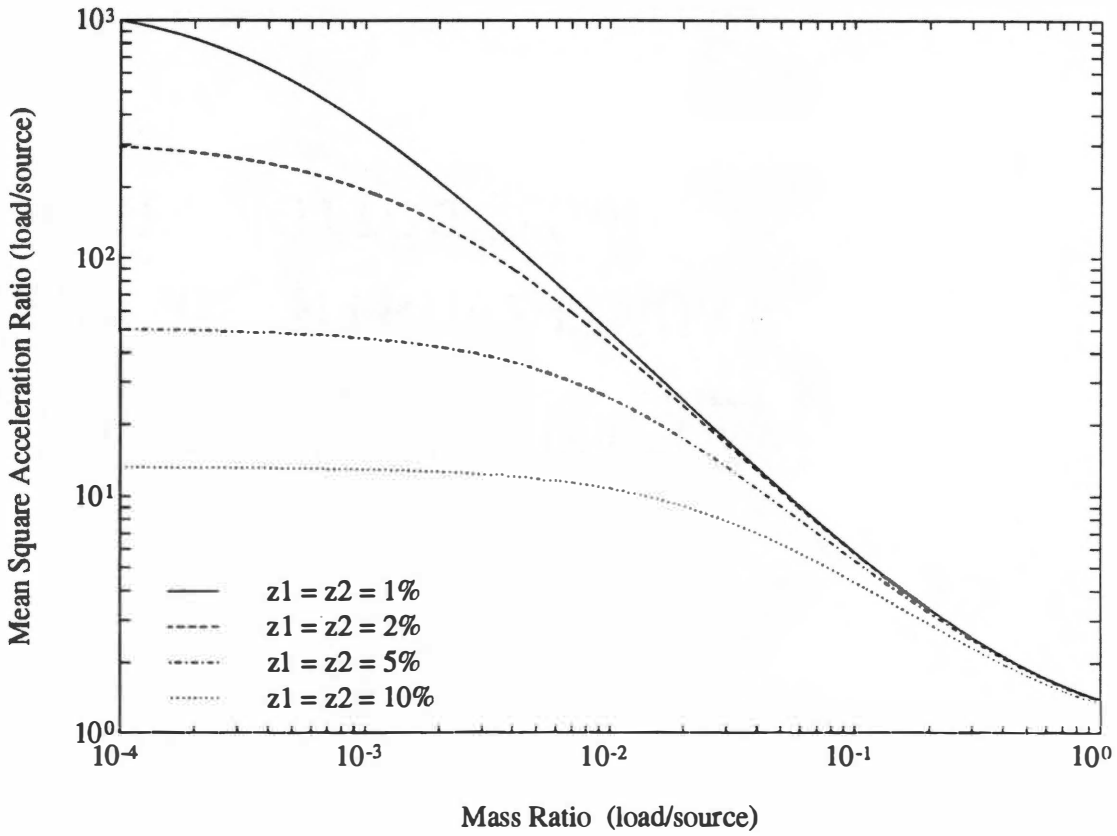

Figure 8.2 Sensitivity of mean-square acceleration of load mass to mean-square free acceleration of source mass when $\omega_2 = \omega_1$.

provide an assortment of model combinations, that can be selected based on which missile section is being evaluated. A designated model custodian can maintain the computer models and ensure that missile interface connections match up. In this regard, different engineering disciplines (strength or dynamic groups) can generate different missile sections that can be run independent of the combined system or solved as an AUR solution routine. This technique is generally referred to as finite element substructuring. Each missile section can be solved independently and then combined with the AUR assembly to solve for the combined system (similar to the impedance method developed in Chapter 4). The engineering time and effort spent in this step can payoff large dividends, as the missile system continues to evolve over the years (the typical missile system has been evolving since the 1970's and 1980's).

2.) Since most missile systems have been deployed for a number of years, it is assumed that production or prototype hardware is available for vibration testing. Mechanical impedance measurements (driving point and transfer functions) are collected for each missile section, critical section subassemblies, and combined section configurations. These measurements could either be accelerance or effective mass. This step is the most difficult to perform correctly, since experimental testing requires an experienced test engineer.

3.) Comparison of the impedance test data to the computer finite element results is performed. Validation of the finite element computer models is achieved by modifying missile model parameters such that the two results are in agreement. Agreement is typically defined as being within 5% to 10% of the measured impedance test data (for both spectral peaks and valleys). It should be emphasized that the success of this step

will depend largely on the accuracy of the measured data, and in order to ensure this, considerable care and attention to detail must be exercised in every aspect of the measurement step.

4.) The gathering of all past missile flight acceleration data is recommended. This data should be stored in a central data bank, along with flight data for different missile systems. Acceleration response data should be recorded at all support point locations where separate vibration test are required. That is, for every level of missile structure to be vibration tested, a flight acceleration record should be available for reference. Missile development programs can use acceleration records for a similar missile system as a baseline, until flight test data is available.

5.) Generate the force control test specifications for each missile section or subassembly to be vibration tested. The dual extremal control method is the most comprehensive impedance method, therefore it is assumed that this is the impedance method to be implemented in the vibration test facility. The acceleration control specifications of step 4 are used along with the impedance measurements/analysis of step 3 to determine the necessary force control specifications. Evaluate the possibility of modifying a missile equipment/support interface to facilitate insertion of force transducers, so that in-flight force measurements can be made. This data would act as a check to verify that the generated force spectrums are in general agreement with the recorded flight interface force levels.

6.) Design or modify vibration test fixtures to accommodate the addition of force transducers. Upgrade the vibration controller to a newer system that allows for

multiple reference spectrums, otherwise use the control scheme shown in Fig. 8.1. Perform dual extremal control vibration testing as previously described.

Conclusion

Realistic vibration tests are a function of (1) the field test data available for reference, (2) the techniques used in deriving the test specifications, and (3) the test techniques used in the laboratory. Mechanical impedance methods offer a rational means of eliminating the costs and schedule delays associated both with overdesign and overtesting to meet conventional infinite impedance vibration specifications.

Mechanical impedance methods have been sparingly utilized over the past 30 years. The equivocation associated with these methods lies in the tacit assumption that infinite impedance testing is a conservative, reasonable approach to laboratory vibration simulation. It is hoped that this argument will loose support and allow engineers to concentrate on producing equipment designs to withstand the field vibration environment, in lieu of overdesigning to survive an unrealistic test artifact.

It has been known for a long time that notching the input acceleration, at the antiresonant frequencies, could limit the overtest of a motion controlled, infinite impedance vibration test. The problem was to decide where, how wide, and how deep the notches should be. The above procedure provides a specific, justifiable way to accomplish the notching based on a force limit. Further work is required in order to specify force control specifications with the same level of confidence possible for acceleration specifications.

REFERENCES

LIST OF REFERENCES

[1] Plunkett, R., Colloquium on Mechanical Impedance Methods for Mechanical Vibrations," ASME Annual Meeting, New York, December 1958.

[2] Morrow, C.T., "Application of the Mechanical Impedance Concept to Shock and Vibration Testing," TRW Space Technology Laboratories, Los Angeles, CA, March 1960.

[3] Otts, J.V., "Force Controlled Vibration Tests: A Step Toward Practical Application of Mechanical Impedance," Shock and Vibration Bulletin, No. 34, Part 5, pp. 45-52, February 1965.

[4] Otts, J.V., "Methods Used to Realistically Simulate Vibration Environments," Shock and Vibration Bulletin, No. 41, Part 4, pp. 29-35, December 1970.

[5] On, F.J., "A theoretical Basis for Mechanical Impedance Simulation in Shock and Vibration Testing," Shock and Vibration Bulletin, No. 33, Part 4, pp. 47-53, March 1964.

[6] Nuckolls, C.E., and Otts, J.V., "A Progress Report on Force Controlled Vibration Testing," Shock and Vibration Bulletin, No. 35, Part 2, pp. 117-130, January, 1966.

[7] Ratz, A.G., "An Impedance-Compensated Random Equalizer," Proceedings-Institute of Environmental Sciences, 1966 Annual Technical Meeting, pp. 353-357, San Diego, April 1966.

[8] Painter, G.W., "Use of Force and Acceleration Measurements in Specifying and Monitoring Laboratory Vibration Tests," Shock and Vibration Bulletin, No. 36, Part 3, pp. 1-13, January 1967.

[9] Hunter, N.F., and Otts, J.V., "The Measurement of Mechanical Impedance and Its Use in Vibration Testing," Shock and Vibration Bulletin, No. 42, Part 1, pp. 55-69, January, 1972.

[10] Clements E.W., "Shipboard Shock and NAVY Devices for its Simulation," Naval Research Laboratory, NRL Report 7396, Washington, D.C., July, 1972.

[11] Scharton, T.D., "Dual Control Vibration Tests of Flight Hardware," Proceedings-Institute of Environmental Sciences, 37th Annual Technical Meeting, San Diego, May 1991.

[12] Morrow, C.T., Shock and Vibration Engineering - Volume 1, John Wiley & Sons, Inc., New York and London, pp. 89-104, 1963.

[13] Curtis, A. and Boykin, T., "Response of Two-Degree-of-Freedom-Systems to White Noise Base Excitation," Journal of the Acoustical Society of America, Vol. 35, No. 5, pp. 655-663, 1961.

[14] Crandall, S.H. and Mark, W.D., Random Vibration in Mechanical Systems, Academic Press, New York and London, pp. 71-97, 1963.

[15] Ewins, D.J., "Measurement and Application of Mechanical Impedance Data - 1. Introduction and Ground Rules," Journal of the Society of Environmental Engineers, Vol. 14, No. 2, pp. 3-12, December 1975.

[16] Ewins, D.J., "Measurement and Application of Mechanical Impedance Data - 2. Measurement Techniques," Journal of the Society of Environmental Engineers, Vol. 15, No. 1, pp. 23-33, March 1976.

[17] Ewins, D.J., "Measurement and Application of Mechanical Impedance Data - 3. Interpretation and Application of Measured Data," Journal of the Society of Environmental Engineers, Vol. 15, No. 2, pp. 7-17, June 1976.

[18] Neubert, V.H., Mechanical Impedance: Modeling/Analysis of Structures, Jostens Printing and Publishing Company, State College, PA, pp. 199-210, 1987.

[19] Murfin, W.B., "Dual Specifications in Vibration Testing," Shock and Vibration Bulletin, No. 38, Part 1, pp. 109-113, August 1968.

[20] Witte, A.F., "Specification of Sine Vibration Test Levels Using a Force-Acceleration Product Technique," Shock and Vibration Bulletin, No. 41, Part 4, pp. 69-78, December 1970.

[21] Witte, A.F., "A Force-Acceleration Control Technique for Vibration Testing," Instrument Society of America, Paper No. 69-650, October 1969.

[22] Witte, A.F. and Rodeman, R., "Dual Specifications in Random Vibration Testing, an Application of Mechanical Impedance," Shock and Vibration Bulletin, No. 41, Part 4, pp. 109-118, December 1970.

[23] Scharton, T.D., "Force Limited Vibration Testing," Proceedings-Technology 2001 Conference, San Jose, CA, pp. 105-115, December 1991.

[24] Scharton, T.D., "Analysis of Dual Control Vibration Testing," Proceedings-Institute of Environmental Sciences, 36th Annual Technical Meeting, April 1990.

[25] Scharton, T.D., "Force Specifications for Extremal Dual Controlled Vibration Tests," Shock and Vibration Bulletin, No. 61, October 1990.

[26] Smallwood, D.O., "An Analytical Study of a Vibration Test Method Using Extremal Control of Acceleration and Force," Proceedings-Institute of Environmental Sciences, 35th Annual Technical Meeting, pp. 263-271, May 1989.

[27] Smallwood, D.O., "Development of the Force Envelope for an Acceleration/Force Extremal Controlled Vibration Test," Shock and Vibration Bulletin, No. 61, pp. 95-104, October 1990.

[28] Sweitzer, K.A., "Mechanical Impedance Correction Technique for Vibration Tests," Proceedings-Institute of Environmental Sciences, 33rd Annual Technical Meeting, pp. 73-76, San Jose, CA, May 1987.

[29] Fackler, W.C., Equivalence Techniques for Vibration Testing, The Shock and Vibration Information Center, Naval Research Laboratory, Washington, D.C., 1972.

[30] Miner, M.A., "Cumulative Damage in Fatigue," Journal of Applied Physics, Vol. 16, A-159, September 1945.

[31] Shigley, J.E., and Mitchell, L.D., Mechanical Engineering Design, 4th Edition, McGraw-Hill Book Company, pp. 285, Figure 7-8, 1983.

[32] Maloney, J.G., Shelton, M.T., and Underhill, D.A., "Structural Dynamic Properties of Tactical Missile Joints - Phase I, II, and III," Electro-Dynamic Division, General Dynamics Corporation, CR-6-348-945-001,2,3, September 1971.

[33] DeJong, A., "Standard Missile-2, Block II, All-Up-Round (AUR) Vibration Modal Survey Testing Program," Missile Systems Division, Raytheon Company, SWS #2902, September, 1989.

[34] Scharton, T.D., "Force Limited Vibration Testing at JPL," Proceedings - 14th Annual Aerospace Testing Seminar, Manhattan Beach, CA, March 1993.

[35] Kern, D.L., Boatman, D.J., Scharton, T.D., and Rentz, P.E., "Random Vibration Testing of SIR-C Electronics Using Force Limiting Techniques," Shock and Vibration Bulletin, No. 63, pp. 651-663, October 1992.

APPENDIXES

APPENDIX A

Chapter 5 *Subsystem II* 5-DOF Simulation Results

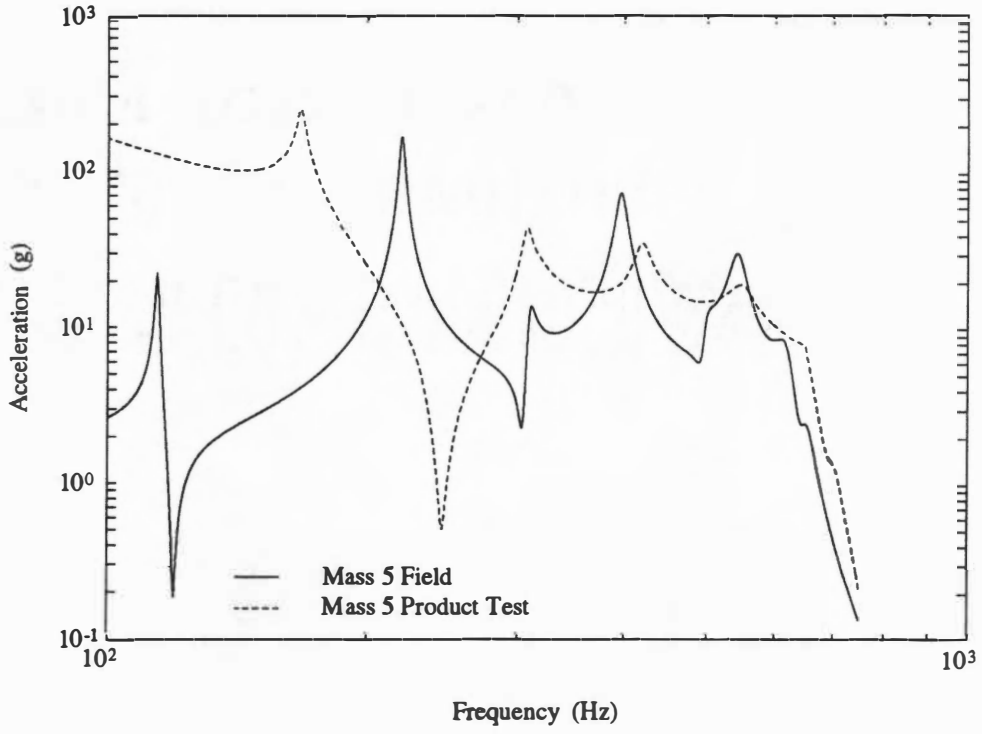

Figure A.1 Acceleration of m_5 comparing 10-DOF field results to those obtained from subsystem *II* test using force-acceleration.

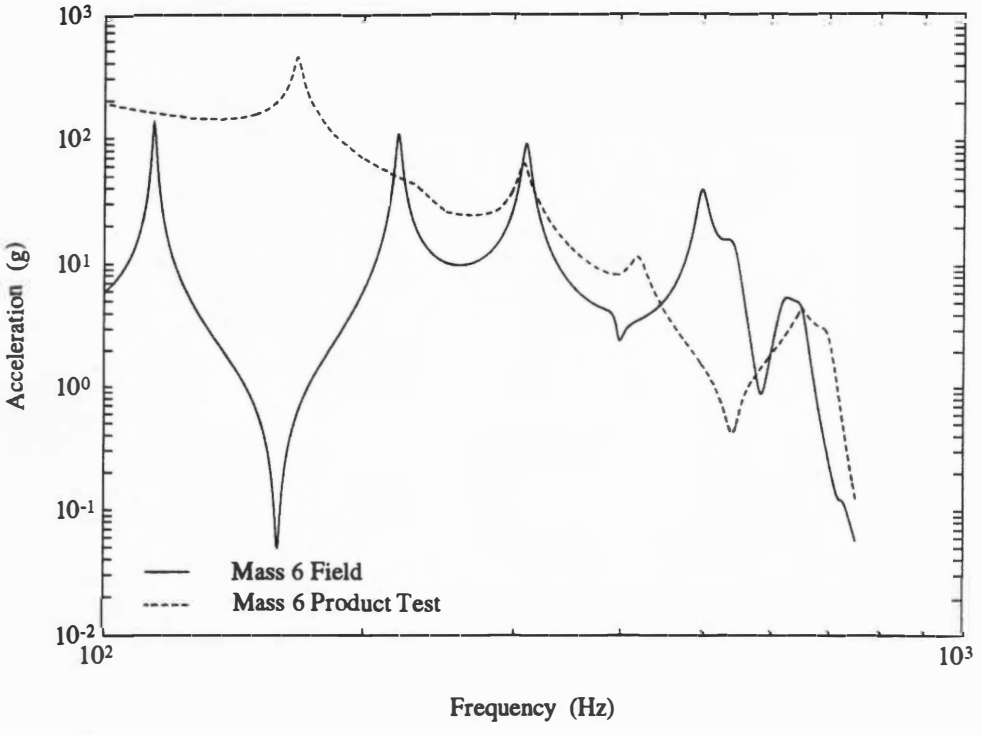

Figure A.2 Acceleration of m_6 comparing 10-DOF field results to those obtained from subsystem *II* test using force-acceleration

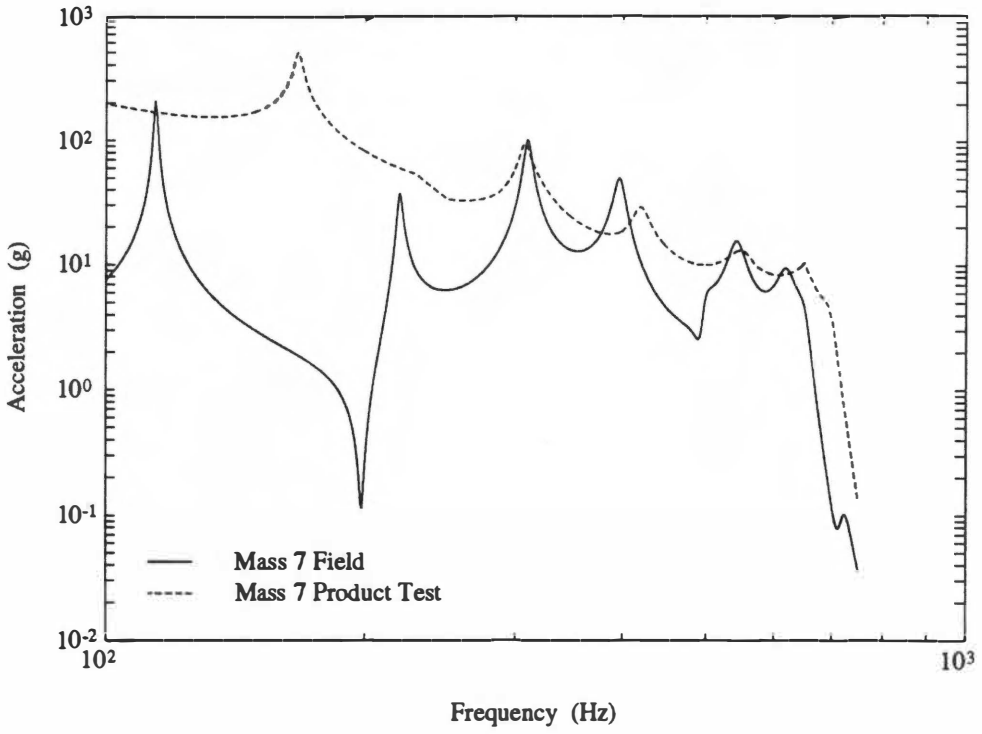

Figure A.3 Acceleration of m_7 comparing 10-DOF field results to those obtained from subsystem *II* test using force-acceleration.

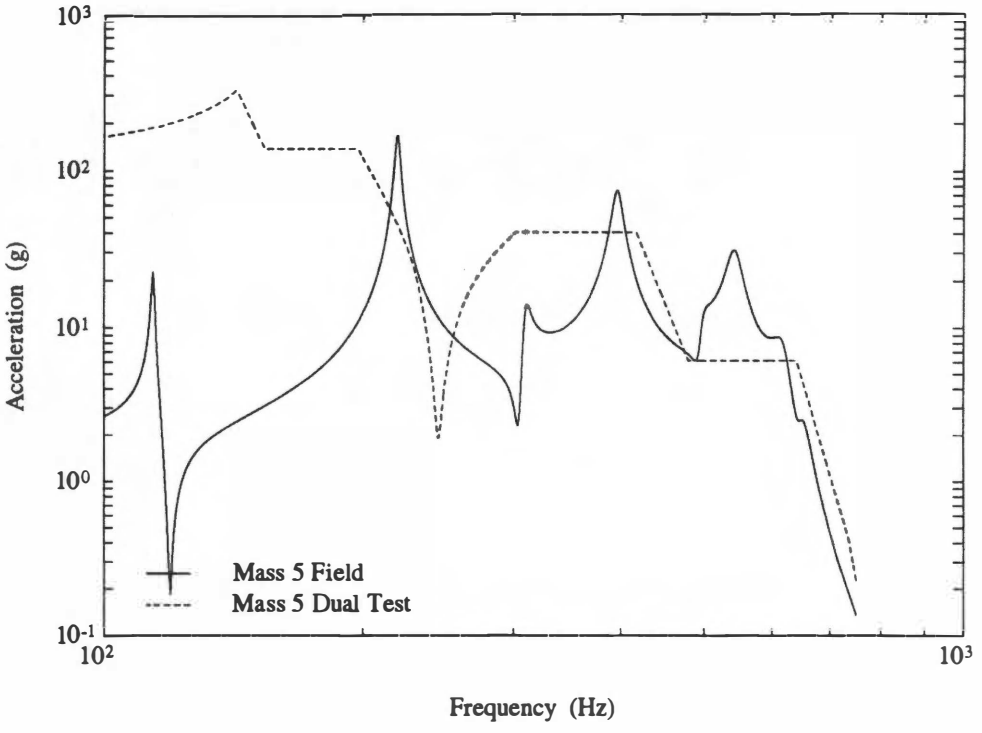

Figure A.4 Acceleration of m_5 comparing 10-DOF field results to those obtained from subsystem *II* test using dual control.

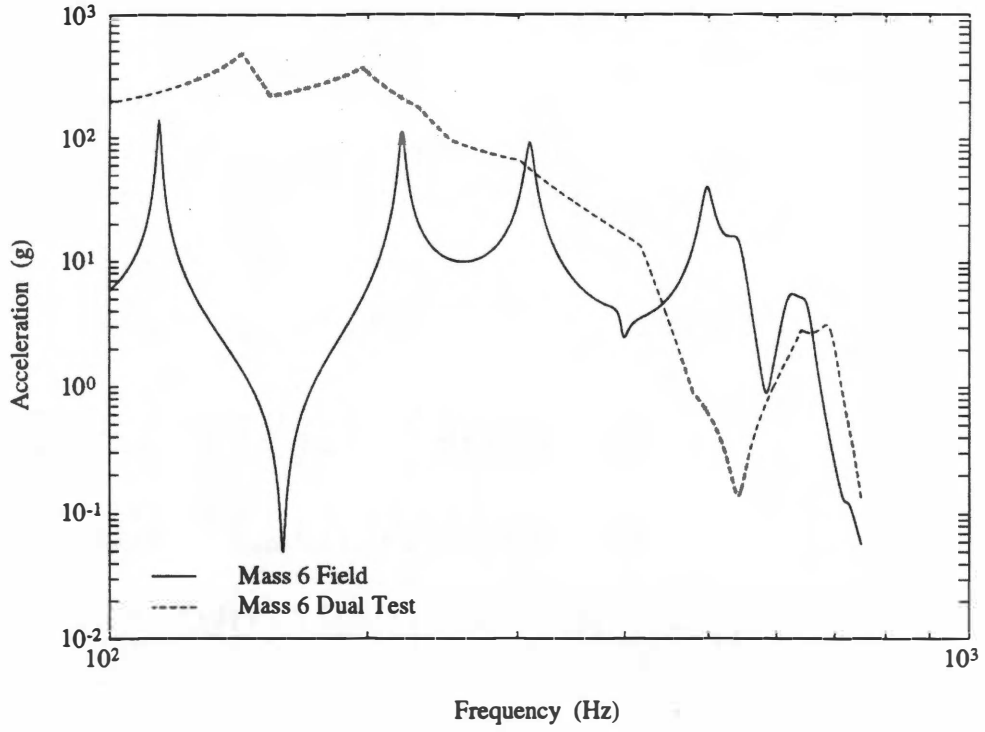

Figure A.5 Acceleration of m_6 comparing 10-DOF field results to those obtained from subsystem *II* test using dual control.

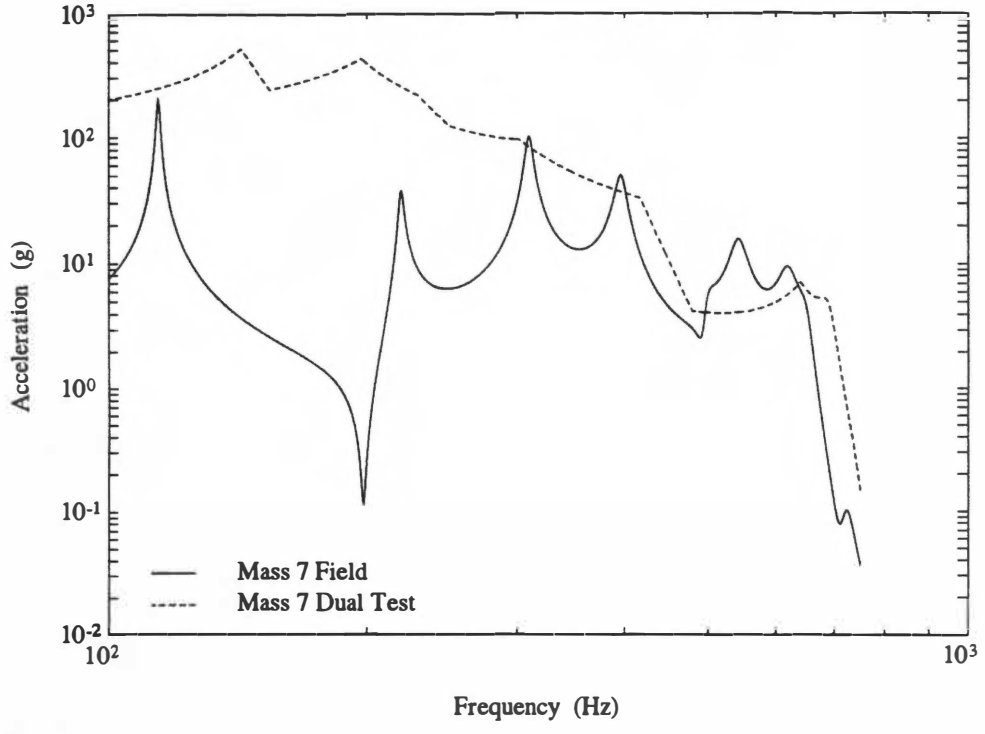

Figure A.6 Acceleration of m_7 comparing 10-DOF field results to those obtained from subsystem *II* test using dual control.

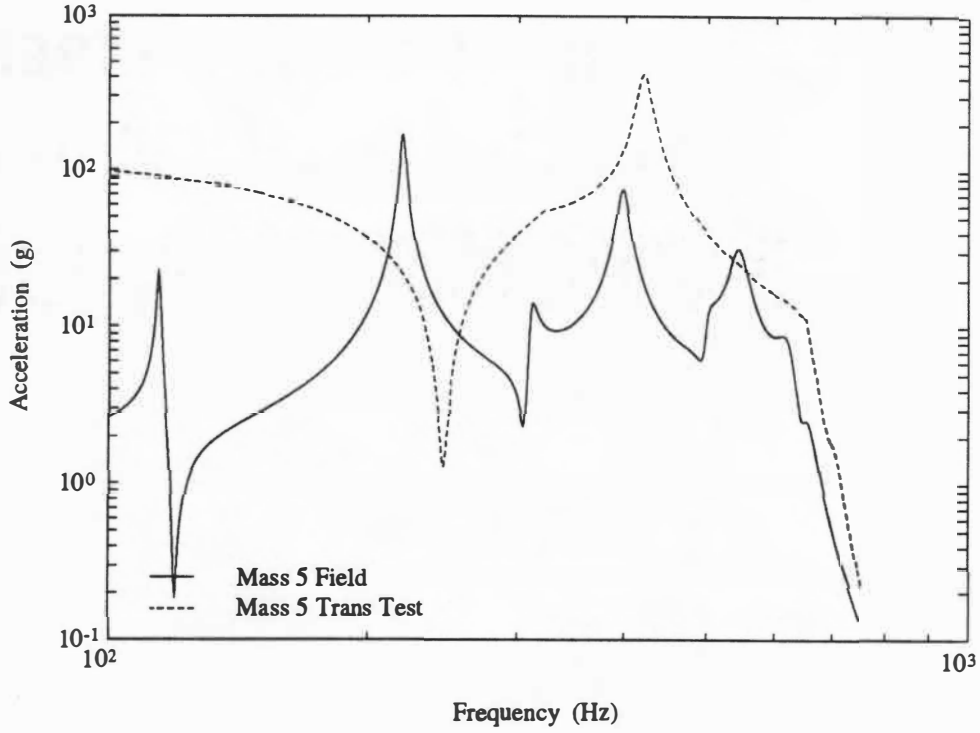

Figure A.7 Acceleration of m_5 comparing 10-DOF field results to those from subsystem *II* test using transmiss. correction.

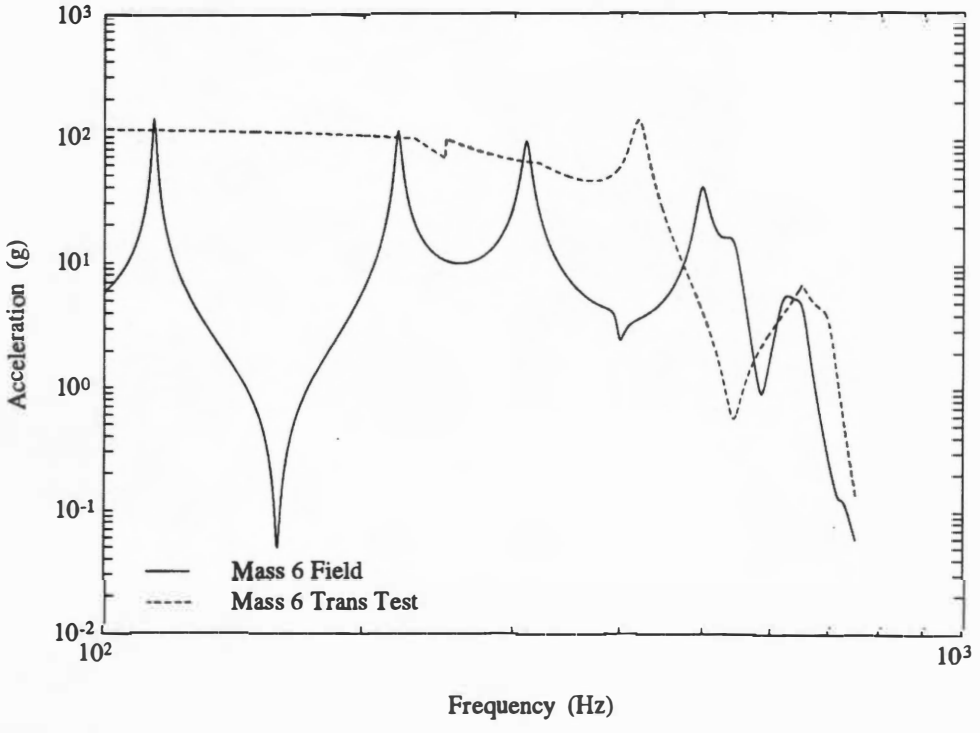

Figure A.8 Acceleration of m_6 comparing 10-DOF field results to those from subsystem *II* test using transmiss. correction.

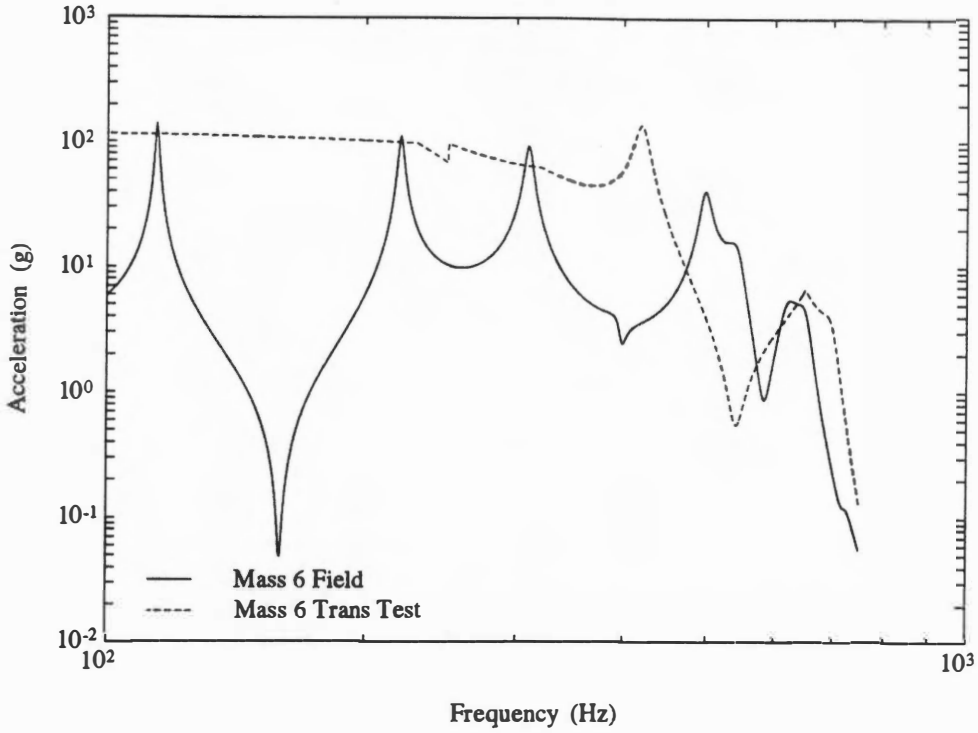

Figure A.9 Acceleration of m_7 comparing 10-DOF field results to those from subsystem *II* test using transmiss. correction.

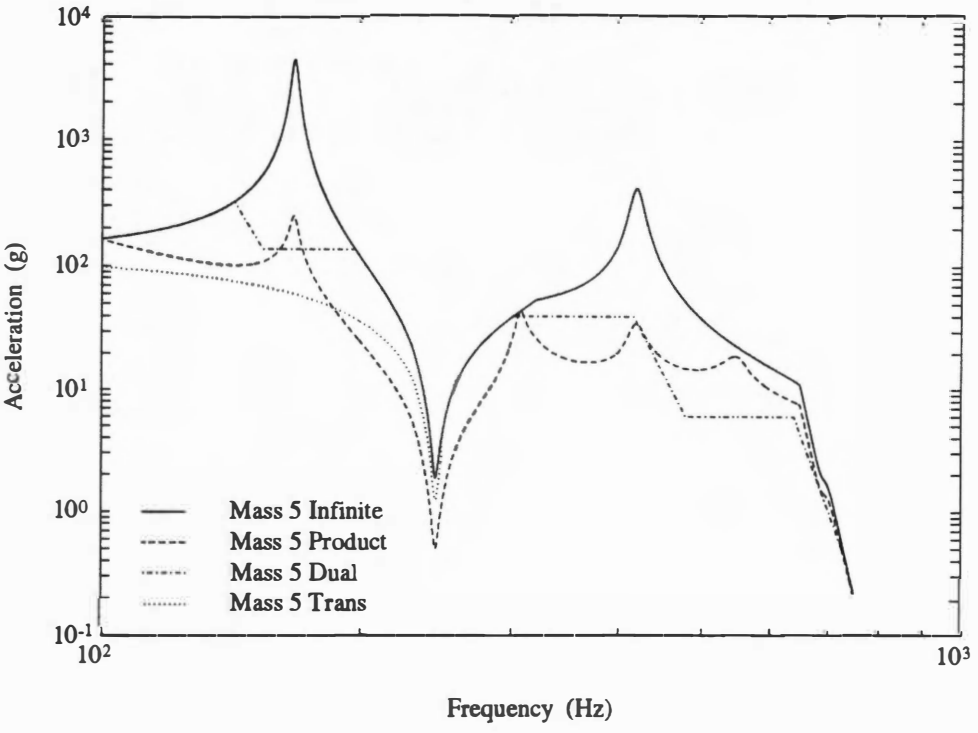

Figure A.10 Acceleration FRF of m_5 comparing the three impedance test methods vs. an infinite impedance test for subsystem *II*.

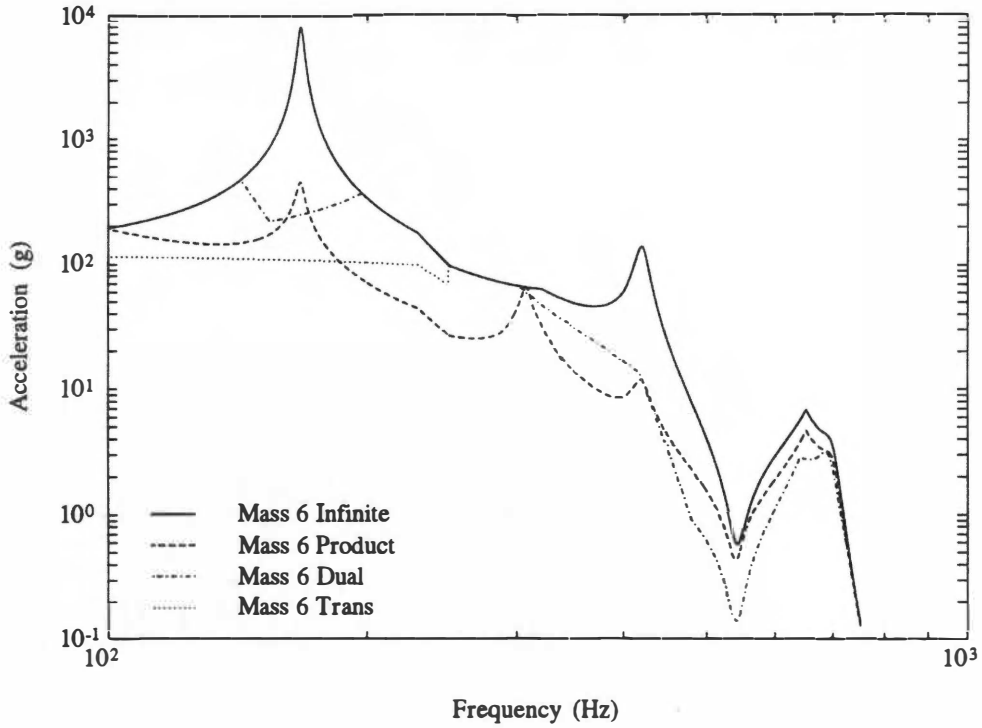

Figure A.11 Acceleration FRF of m_6 comparing the three impedance test methods vs. an infinite impedance test for subsystem *II*.

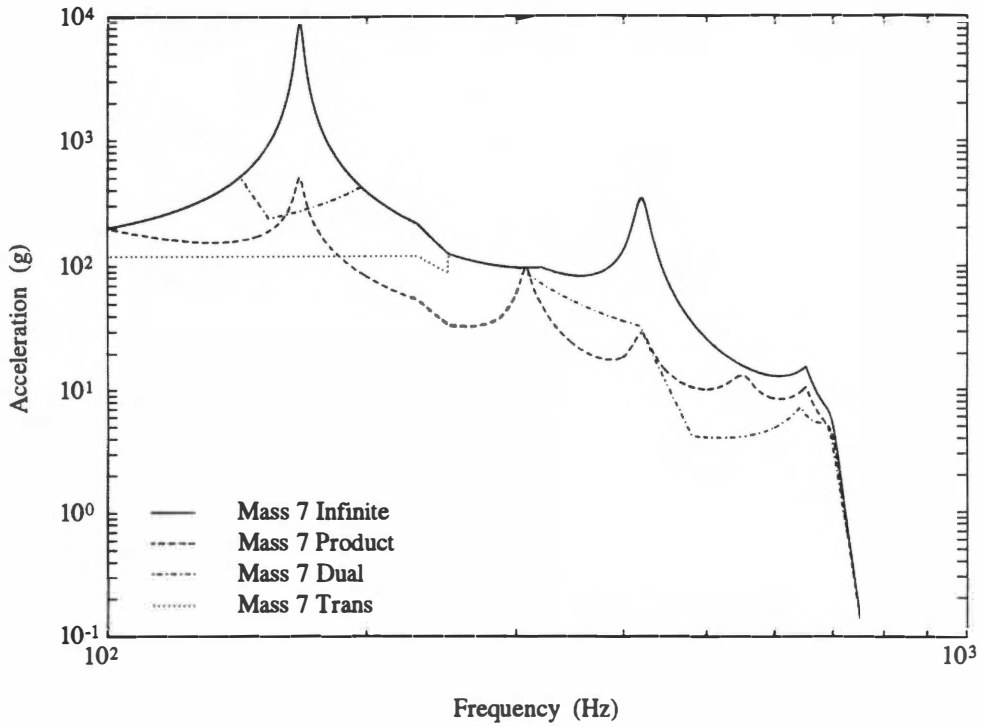

Figure A.12 Acceleration FRF of m_7 comparing the three impedance test methods vs. an infinite impedance test for subsystem *II*.

APPENDIX B

Chapter 6 Fabrication Drawings of Beam/Block Structure

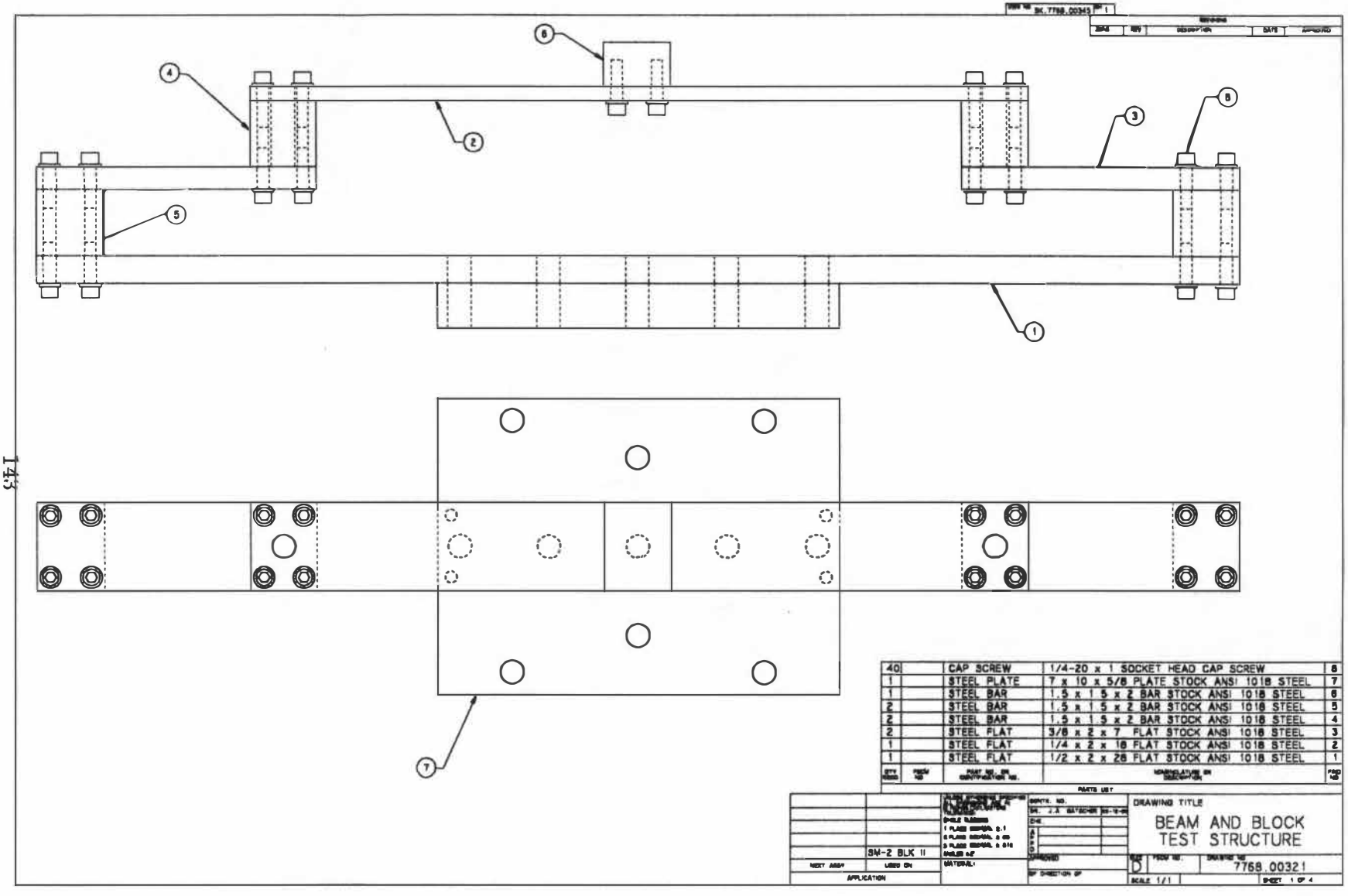

Figure B.1 Fabrication drawing of beam and block test structure - sheet 1.

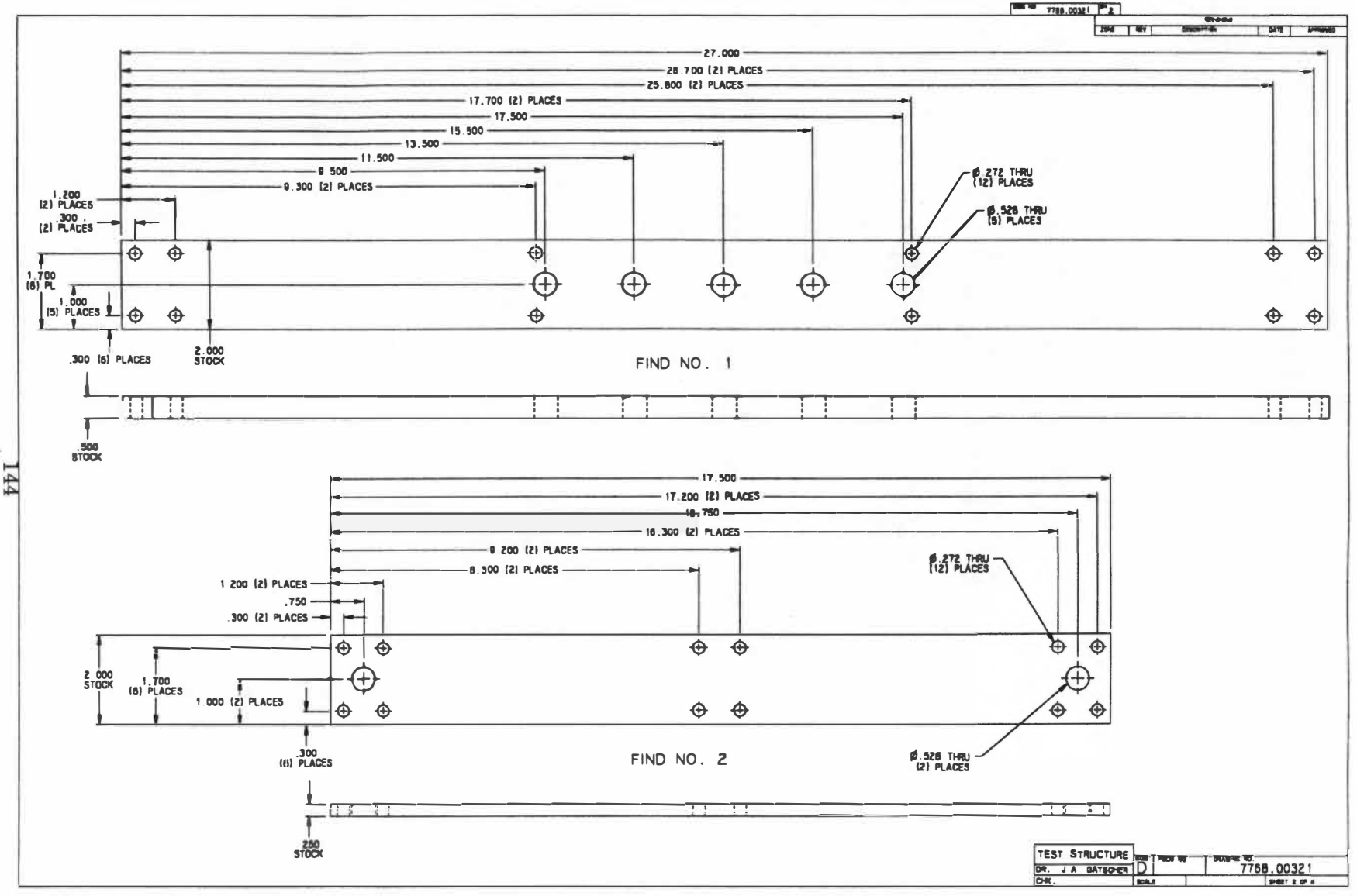

Figure B.2 Fabrication drawing of beam and block test structure - sheet 2.

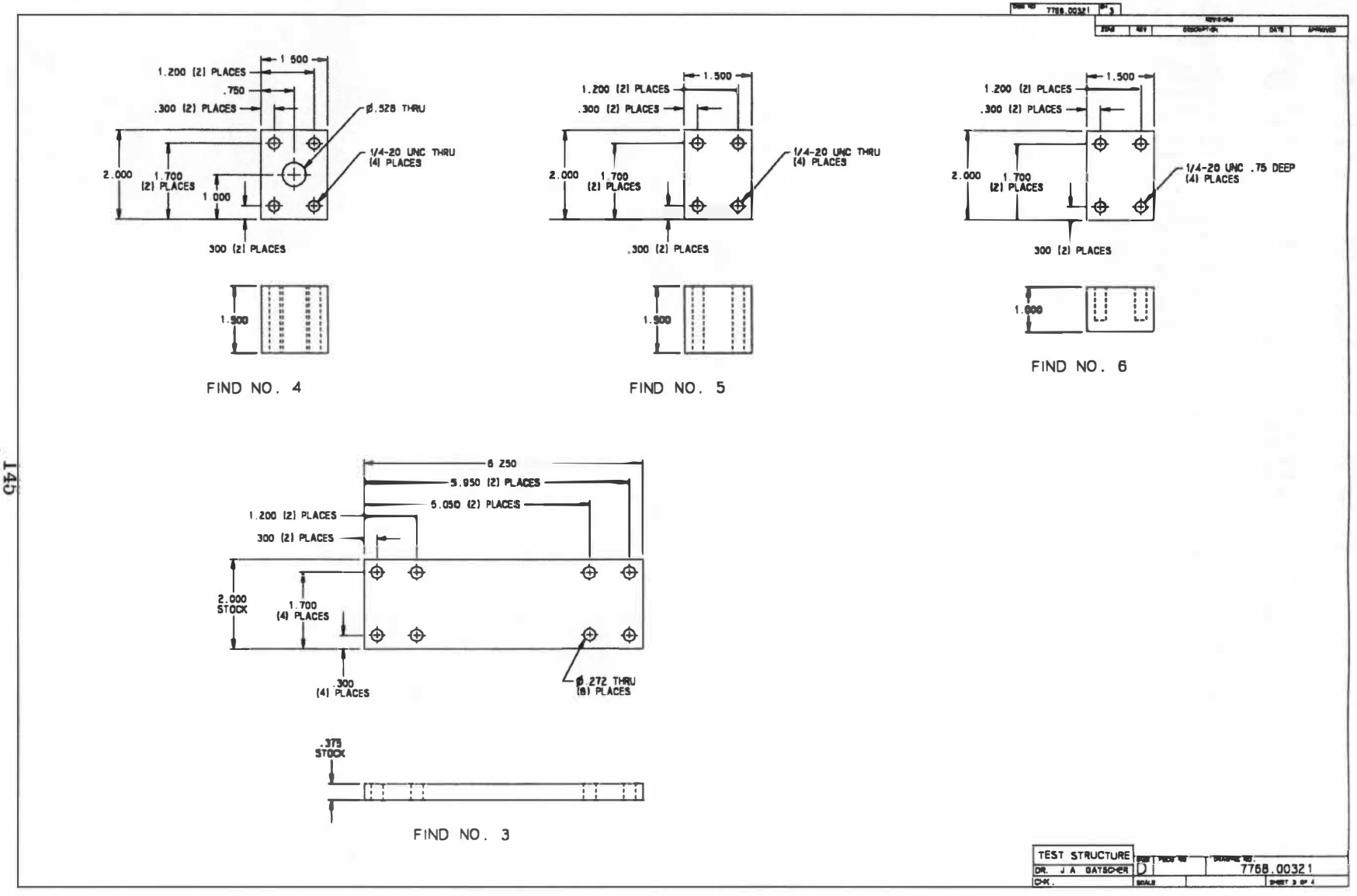

Figure B.3 Fabrication drawing of beam and block test structure - sheet 3.

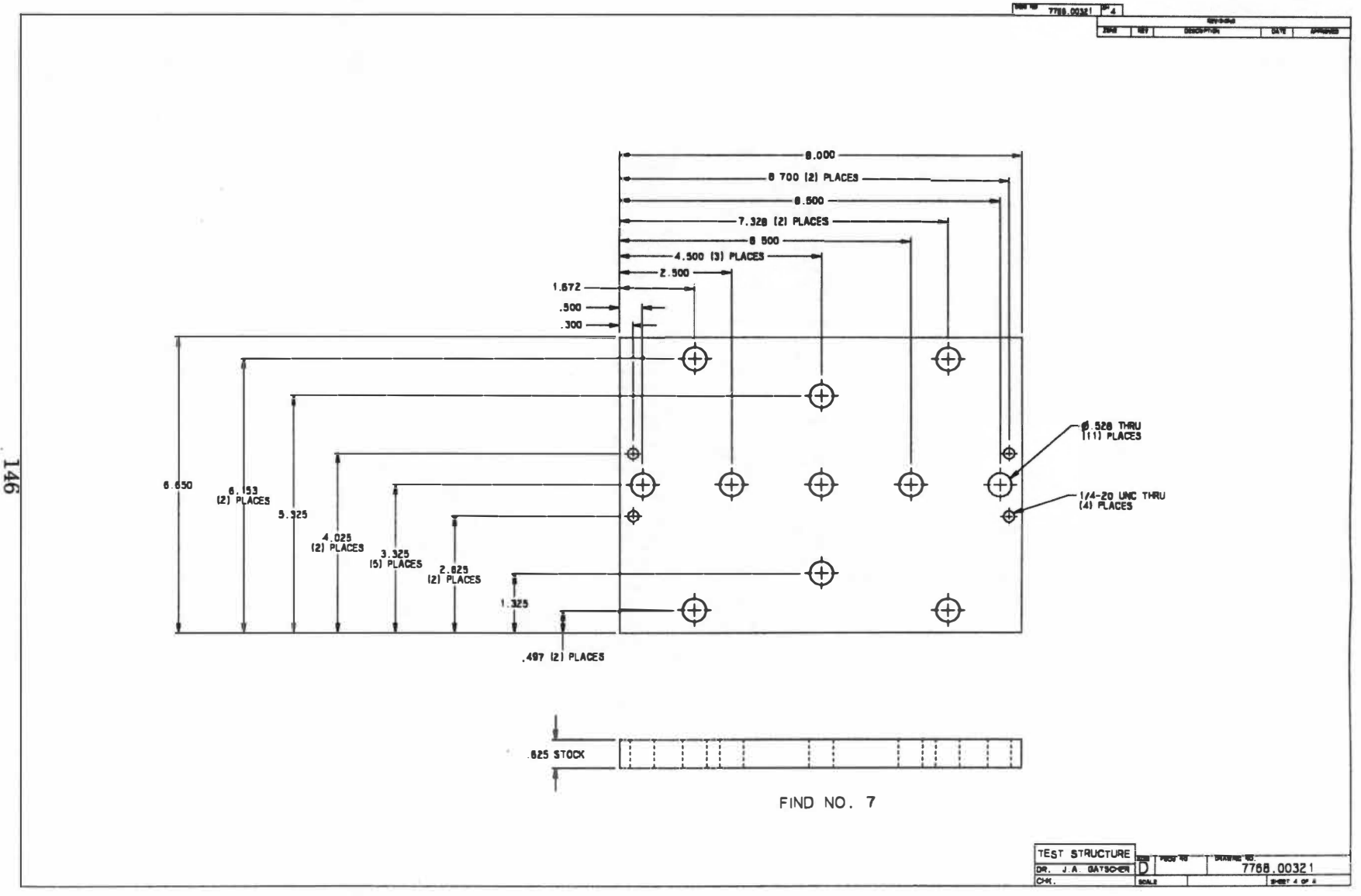

Figure B.4 Fabrication drawing of beam and block test structure - sheet 4.

APPENDIX C

Chapter 7 Standard Missile 2 Structural Dynamic Properties

Table C.1 SM-2 Block IIIA MR dynamic properties listing

Missile Station (in)	Weight (lb)	Stiffness ($lb\text{-}in^2$)	Weight Inertia ($lb\text{-}in^2$)	Rotational Compliance (rad/in-lb)	Shear Compliance (in/lb)
Radome - Airframe					
-1.575	0.010	1.00e+07			
1.260	0.500	1.80e+08	1.10		
1.760	1.500	7.20e+08	12.90		
10.260	2.500	1.70e+09	42.09		
15.260	2.800	2.92e+09	70.47		
20.260	4.000	3.94e+09	128.05		
25.760	4.800	2.41e+09	101.01		
27.560		2.41e+09		2.2e-09	
27.560		1.66e+09			
Guidance Section - Airframe					
29.760	15.510	1.66e+09	194.00		
36.260	6.580	2.60e+09	246.00		
36.560		7.64e+09			
37.562		7.64e+09		1.0e-08	
Warhead Section - Airframe					
37.650	2.243	3.52e+09	43.00		
38.400	0.873	4.03e+09	10.10		
38.800	4.605	7.13e+09	28.30		
38.810		7.13e+09			
39.390	8.540	1.80e+09	170.50		
43.590	15.807	1.80e+09	332.40		
47.790	14.842	1.80e+09	251.20		
48.730	7.536	1.80e+09			
51.990	9.255	7.13e+09	185.10		
52.530		7.13e+09			
52.540	8.339	1.51e+09	58.90		
55.900	5.520	1.51e+09	112.80		

Table C.1 (Continued)

Missile Station (in)	Weight (lb)	Stiffness (lb-in^2)	Weight Inertia (lb-in^2)	Rotational Compliance (rad/in-lb)	Shear Compliance (in/lb)
56.460	18.900	1.51e+09	299.10		
59.280	2.044	6.48e+09	47.40		
59.940	3.576	5.48e+09	63.50		
60.712		5.48e+09		4.4e-09	
Autopilot Battery Section - Airframe					
61.540	2.259	9.10e+08			
61.670	5.280	9.10e+08	173.00		
67.780	5.800	9.10e+08	183.80		
68.800		3.00e+09			
69.260	2.630	3.00e+09	89.70		
69.480		3.00e+09			
71.410		4.00e+09			
73.000		4.00e+09		1.1e-09	
Rocket Motor Full Weight - Airframe					
73.000	23.050	4.05e+09	546.60		
75.000	31.125	3.47e+09	487.90		
80.000	38.095	3.47e+09	524.66		
85.000	39.870	2.92e+09	619.66		
90.000	53.465	2.92e+09	798.63		
95.000	49.849	2.92e+09	798.63		
100.000	53.465	2.92e+09	798.63		
105.000	49.849	2.92e+09	798.63		
110.000	53.465	2.92e+09	798.63		
115.000	49.849	2.92e+09	798.63		
120.000	53.537	2.92e+09	809.00		
125.000	50.571	2.92e+09	849.75		
130.000	54.187	2.92e+09	849.75		
135.000	50.571	2.92e+09	849.75		

Table C.1 (Continued)

Missile Station (in)	Weight (lb)	Stiffness ($lb\text{-}in^2$)	Weight Inertia ($lb\text{-}in^2$)	Rotational Compliance (rad/in-lb)	Shear Compliance (in/lb)
140.000	52.506	2.92e+09	849.75		
145.000	50.571	2.92e+09	849.75		
150.000	52.506	2.92e+09	849.75		
155.000	50.571	4.22e+09	849.75		
157.500		6.91e+09			
160.000	50.010	5.40e+09	846.13		
164.000	46.807	4.85e+09	1344.60		
168.000	44.483	7.48e+09	599.58		
170.400	36.690	7.48e+09	589.89		
170.400		7.48e+09			
170.700		1.42e+09		4.5e-09	
Steering Control Section - Airframe					
172.200	6.791	1.53e+09	160.00		
174.000		2.40e+09			
175.000	7.099	2.40e+09	46.00		
176.000	32.450	2.40e+09	440.00		
177.380	48.600	3.70e+09	598.00		
181.370	6.500	3.70e+09	161.30		
184.000	0.010				
Seeker Head - Appendage					
19.560	10.440	2.60e+05			
20.570		2.60e+05		8.7e-08	
22.560	0.500	1.00e+06			
24.660	14.140	1.20e+06	44.00		
24.660		1.00e+07		2.7e-09	2.7e-09
26.280	2.220	2.00e+07	71.00		
27.560		2.00e+07		2.7e-09	1.3e-09
27.560		2.00e+07			

Table C.1 (Continued)

Missile Station (in)	Weight (lb)	Stiffness ($lb\text{-}in^2$)	Weight Inertia ($lb\text{-}in^2$)	Rotational Compliance (rad/in-lb)	Shear Compliance (in/lb)
Guidance - Appendage					
27.560		1.80e+08			
27.560		1.80e+08		1.0e-06	2.0e-07
27.560		1.80e+08			
29.080	13.600	1.80e+08			
30.370		1.80e+08		8.0e-07	
31.710	10.900	1.80e+08			
33.020		1.80e+08		8.0e-07	
34.370	12.000	1.80e+08			
35.150		1.80e+08		8.0e-07	
35.570	4.000	1.80e+08			
36.210		1.80e+08		8.0e-07	
36.210		1.80e+08			
Removable Explosive Assembly - Appendage					
38.810		1.20e+09		3.0e-06	
38.810	7.610	1.20e+09			
41.090	15.240	1.20e+09	245.97		
43.380	15.240	1.20e+09			
45.670	15.240	1.20e+09	328.00		
47.960	15.240	1.20e+09			
50.250	15.240	1.20e+09	245.97		
52.530	7.610	1.20e+09			
52.530		1.20e+09			
Autopilot - Appendage					
60.510	1.431	6.00e+08			
62.140	3.839	6.00e+08			
63.140	5.415	6.00e+08			
64.140	5.431	6.00e+08			

Table C.1 (Continued)

Missile Station (in)	Weight (lb)	Stiffness ($lb\text{-}in^2$)	Weight Inertia ($lb\text{-}in^2$)	Rotational Compliance (rad/in-lb)	Shear Compliance (in/lb)
65.140	5.431	6.00e+08			
66.010		4.90e+09			2.5e-08
67.010		4.90e+09		3.0e-06	
67.260	12.346	4.90e+09			
67.260		4.90e+09		1.5e-06	
68.760	17.038	4.90e+09			
69.510		4.90e+09			5.2e-08
Rocket Motor Nozzle - Appendage					
170.400		7.61e+09			
175.160		7.61e+09			
176.170	2.400	9.30e+08			
179.700	2.400	1.03e+09			
183.230	2.400	2.05e+09			
184.000		4.15e+09			
Total Weight = 1,510 lb					

VITA

Jeffrey A. Gatscher received his Bachelor of Science degree in mechanical engineering from Michigan Technological University in 1983. In 1989 he entered the University of Tennessee, Knoxville as a part-time graduate student and in 1994 received a Master of Science degree in mechanical engineering. He has specialized in dynamic and static analysis of aerospace launch vehicle systems. Currently, he is a senior development engineer with Raytheon Company's Missile Systems Division, where he works on analysis and simulation of guided missile systems to shock and vibration environments.